

# Crystal Phase Engineering in III-V Semiconductor Films: from Epitaxy to Devices

Présentée le 21 août 2020

à la Faculté des sciences et techniques de l'ingénieur  
Laboratoire des matériaux semiconducteurs  
Programme doctoral en science et génie des matériaux

pour l'obtention du grade de Docteur ès Sciences

par

**Philipp STAUDINGER**

Acceptée sur proposition du jury

Dr Y. Leterrier, président du jury  
Prof. A. Fontcuberta i Morral, Dr K. E. Moselund, directrices de thèse  
Prof. E. P. A. M. Bakkers, rapporteur  
Prof. P. Krogstrup Jeppesen, rapporteur  
Prof. N. Grandjean, rapporteur



*“If we walk far enough,” says Dorothy,  
“we shall sometime come to some place, I am sure.”*

– L. Frank Baum (The Wonderful Wizard of Oz)

To my family.



# Acknowledgements

The past years have been an incredible journey which would not have been possible without the help from my supervisors, coworkers, friends and family. I would like to express my gratitude to everyone that followed me along the way and made this an experience that I will always treasure.

**Heinz**, thank you for your unconditional support. For always being available and sharing all the ups and downs of this project. For giving me the freedom I wanted and, at the same time, offer guidance when I needed it. For your commitment to research and endless optimism. I am immensely indebted to you for all the knowledge you passed on to me, for teaching me how to approach problems from different angles and reach ambitious goals. I could not have wished for a better supervisor.

My deepest gratitude goes to **Kirsten** for providing an inspiring and motivating environment in which I could grow both as a researcher and as a person. Thank you for being a manager that sincerely cares about us, our concerns and well-being. Your positive attitude and scientific support greatly enriched my time at IBM.

I would like to thank **Prof. Anna Fontcuberta i Morral** for her academic supervision, valuable advice and constant availability. It was always a pleasure to visit you and your group in Lausanne.

The members of the committee not only took the time to evaluate this work and give helpful feedback, but also found space in their busy calendars to participate to my thesis examination. I am very thankful to **Prof. Erik Bakkers** from TU Eindhoven, **Prof. Peter Krogstrup** from Microsoft Research, **Prof. Nicolas Grandjean** and **Dr. Yves Leterrier** from EPFL.

I am grateful to the S&T department managers **Dr. Heike Riel** and **Dr. Walter Riess** for closely following my research and providing valuable advice.

It is only due to a team of incredibly skilled engineers and scientists that all the tools and processes needed for this research project run as smoothly as they do. I would especially like to thank **Marilyne** for introducing me to the fascinating world of TEM imaging, for teaching me her tricks and supporting me whenever needed. **Antonis** for maintaining the high standards of our e-beam lithography tool and exposing countless of chips with unusual material stacks and other peculiarities. I really enjoyed my FIB-sessions with **Steffen**, not only because I knew that they will result in a perfect TEM lamella, but also because of the great conversations we shared. When it comes to fabrication and processing questions there are two doors you can

## Acknowledgements

---

knock on (metaphorically speaking, they are usually found in the cleanroom). Thank you **Ute** and **Daniele** for all your advice and support.

A large part of this work is dedicated to optical characterization. I am very thankful to **Emanuel** for allowing me to misuse his Raman microscope for my PL studies. **Svenja** and **Noelia** have always been extremely helpful with in-depth discussions about photonics. Thank you also for carrying out some of the essential measurements for this thesis and for all the non-work-related activities we did such as traveling Japan or biking the Uetliberg. The CL studies I carried out together with **Nicolas Tappy** greatly enhanced my understanding of this new kind of semiconductor. Thank you for that and your hospitality at EPFL.

I was lucky enough to be involved in multiple EU research projects and international collaborations. I would especially like to acknowledge **Prof. Erik Bakkers**, **Prof. Jos Haverkort**, **Prof. Jonathan Finley**, **Prof. Silvana Botti**, **Prof. Friedhelm Bechstedt**, **Prof. Michael Johnston**, **Prof. Yamina Andre**, **Prof. Evelyne Gil** and **Prof. Alois Lugstein** for countless fruitful discussions, for exchanging samples and for sharing their deep insights on so many different topics. I would further like to thank **Elham**, **Alain**, **Yizhen**, **Dorian**, **Sabrina**, **Kun** and **David**. I always enjoyed spending time with you during our regular meetings and discuss not only about science. A big thank you also goes to **Mohammed** and **Gabin** for dedicating a lot of their time to perform HVPE growth experiments on our template structures.

I am grateful for all the incredibly smart colleagues and friends I found at IBM. **Lukas**, your endless knowledge and unique way of solving challenging problems have always been inspiring to me. Thank you for deeply understanding my project and providing valuable input from the very beginning. I would like to thank **Bernd** for all the discussions we had about physics and life, and **Sigi** for his feedback especially on my presentations. **Clarissa**, how could I ever forget my first two weeks at IBM, which I spent with you at the MOCVD? Thank you for introducing me to all the different tools, for your warm personality and also for resolving my first loading attempt and never talk about it again. Together with **Yannick** I really developed a good feeling for MOCVD growth and especially nucleation on Si. I am also grateful for the first patent we wrote together. From **Nicolas** I learned a lot about crystallography and TEM imaging. **Preksha** is not only an expert in photonics, but also a good friend with whom I shared great adventures such as ski weekends and music festivals. Our group would have been definitely less fun without **Fabian**. Thank you also for our numerous skiing trips and for climbing the Daubenhorn together. With **Markus R.** and **Simon** I found friends that would not only cross the Alps with me on our bikes, but also share hobbies such as photography and table soccer. A big thank you also goes to all the other colleagues and office mates **Cezar**, **Markus S.**, **Andrea**, **Alan**, **Nico**, **Daniel**, **Pengyan** and **Kasia**. Thank you all for making IBM an amazing place to work at.

Last but not least I would like to acknowledge my **family** for their unconditional love and support. In particular I thank my parents **Margit** and **Peter**, my brother **Christoph** with **Birgit**, my sister **Petra** with **Johannes** and my granny **Emma**. A big thanks also goes to **Elisabetta** and my dear **friends** in Austria. None of this would have been possible without you.

*Zurich, July 23, 2020*

P. S.

# Abstract

*Crystal phase engineering* is an exciting pathway to enhance the properties of conventional semiconductors. Metastable SiGe presents a direct band gap well suited for optical devices whereas wurtzite (WZ) phosphide alloys enable efficient light emission in the green spectral range. Availability of these materials could profoundly impact electronics as well as solid-state lighting industries. However, their synthesis in high quality and beyond nanowire size constraints remained elusive, hampering both scientific and commercial exploitation.

In this thesis, we develop new approaches for metastable film growth to enable a platform for robust material characterization and device fabrication. Metal-organic vapor phase epitaxy is used to grow pure WZ nanowires and fins. To obtain planar layers, we explore two extensions of this well-known technique. The first one is based on conformal epitaxy and enables the use of standard (001)-oriented substrates. In this way, we achieve the controlled concurrent epitaxy of stable and metastable InP. We further propose a variation of this approach by using a nanowire as seed. This establishes a clear route for the synthesis of a large range of materials as is exemplarily demonstrated for WZ GaAs films.

For the second technique we explore a method to enforce epitaxial lateral overgrowth on (111)A-oriented substrates. This allows to deposit pure WZ InP layers on insulator exceeding areas of  $100\text{ }\mu\text{m}^2$ , the largest ever demonstrated. We conceive a nucleation-based model and argue on a fundamental size limitation of metastable film epitaxy.

Further advancement of this process allows to directly grow metastable micro- and nanostructures, which are optically isolated from the substrate. The high quality and shape-control of these crystals enables room-temperature lasing in WZ InP microdisks.

This thesis demonstrates the successful development of new concepts to synthesize metastable semiconductors with pure crystalline phase and dimensions tailored towards planar device fabrication. We expect our findings to significantly contribute to the realization of crystal phase engineered electronic and optoelectronic devices.

**Keywords:** crystal structure • III-V semiconductors • indium phosphide (InP) • wurtzite • polytypism • metal-organic vapor phase epitaxy (MOVPE) • metastable film • photoluminescence • transmission electron microscopy (TEM) • room-temperature lasing



# Zusammenfassung

Die Manipulation der Kristallphase ist ein spannender Ansatz um die Eigenschaften konventioneller Halbleiter zu verbessern. Metastabiles SiGe weist eine direkte Bandlücke auf, ideal für optische Bauelemente. Phosphid-Verbindungen in der Wurtzit (WZ) Kristallstruktur ermöglichen effiziente Lichtemission im grünen Spektralbereich. Die Verfügbarkeit dieser Materialien könnte bedeutenden Einfluss auf die Elektronik- sowie Beleuchtungsindustrie haben. Deren Synthese in guter Qualität und jenseits Grössenlimitierungen von Nanodrähten ist jedoch ausserordentlich schwierig.

In dieser Arbeit entwickeln wir neue Methoden, um metastabile Filme zu synthetisieren. Wir verwenden metallorganische Gasphasenepitaxie um Nanodrähte und Lamellen in reiner WZ Phase zu wachsen und entwerfen zwei Erweiterungen um planare Schichten zu erhalten. Die erste basiert auf konformer Epitaxie und ermöglicht die Verwendung von (001)-orientierten Substraten. Auf diese Weise bewerkstelligen wir die kontrollierte und gleichzeitige Epitaxie von stabilem und metastabilem InP. Weiters schlagen wir eine Variation dieses Ansatzes vor, indem wir einen Nanodraht als Kristallkeim verwenden. Dies ebnet den Weg für viele weitere Materialien, was exemplarisch für WZ GaAs Filme gezeigt wird.

Für die zweite Methode untersuchen wir laterales epitaktisches Überwachsen auf (111)A-orientierten InP Substraten. Auf diese Weise können wir die grössten je gezeigten reinen WZ Schichten mit mehr als  $100\text{ }\mu\text{m}^2$  über einem Isolator abscheiden. Wir entwickeln ein Nukleations-basiertes Modell, das eine fundamentale Grössenlimitierung für das Wachstum von metastabilen Filmen erklärt.

Eine Weiterentwicklung dieses Prozesses erlaubt die direkte Synthese von metastabilen Mikro- und Nanostrukturen, die optisch vom Substrat isoliert sind. Die hohe Qualität dieser Kristalle ermöglicht Lasing in WZ InP Mikrodisk bei Raumtemperatur.

Diese Arbeit zeigt neue Konzepte auf um metastabile Halbleiter in hoher Qualität und in geeigneten Grössen für planare Fabrikationsprozesse herzustellen. Wir erwarten, dass unsere Erkenntnisse bedeutsam zur Realisierung von Kristallphasen-manipulierten elektronischen und optoelektronischen Bauelementen beitragen werden.

**Stichwörter:** Kristallstruktur • III-V Halbleiter • Indiumphosphid • Wurtzit • Polytypismus • metallorganische Gasphasenepitaxie • metastabiler Film • Mikrodisk • Transmissionselektronenmikroskopie • Raumtemperatur Lasing



# Contents

<b>Acknowledgements</b>	<b>v</b>
<b>Abstract</b>	<b>vii</b>
<b>Zusammenfassung</b>	<b>ix</b>
<b>List of Publications</b>	<b>xiii</b>
<b>List of Figures and Tables</b>	<b>xv</b>
<b>List of Acronyms</b>	<b>xix</b>
<b>1 Introduction</b>	<b>1</b>
1.1 Crystal Phase Engineering – on the Search for New Materials . . . . .	2
1.2 State of the Art – Synthesis of Metastable Crystal Phases . . . . .	4
1.3 Epitaxy Strategies for Metastable Films – beyond Nanowire Size Constraints .	6
1.4 Scope and Structure of this Thesis . . . . .	7
<b>2 Semiconductor Crystals in Stable and Metastable Phases</b>	<b>9</b>
2.1 Crystal Structure . . . . .	9
2.2 Defects . . . . .	12
2.3 Electronic Band Structure . . . . .	13
2.4 Epitaxial Growth . . . . .	18
2.5 Selective Growth of Nanostructures . . . . .	22
2.6 Polytypism in III-V Semiconductors . . . . .	27
2.7 Synthesis of Metastable Semiconductors . . . . .	30
<b>3 Experimental Methods</b>	<b>35</b>
3.1 Conformal Epitaxy . . . . .	35
3.2 Zipper-Induced Epitaxial Lateral Overgrowth . . . . .	39
3.3 Structural Characterization using STEM . . . . .	40
3.4 Optical Characterization using $\mu$ -PL . . . . .	42

## Contents

---

<b>4</b>	<b>Metastable Film Formation by Conformal Epitaxy</b>	<b>45</b>
4.1	Publication 1 . . . . .	46
4.2	Additional Results . . . . .	57
4.3	Main Achievements . . . . .	61
<b>5</b>	<b>Metastable Film Formation by Zipper-Induced Epitaxial Lateral Overgrowth</b>	<b>63</b>
5.1	Publication 2 . . . . .	64
5.2	Additional Results . . . . .	75
5.3	Main Achievements . . . . .	79
<b>6</b>	<b>Room Temperature Lasing from Wurtzite InP Microdisks</b>	<b>81</b>
6.1	Publication 3 . . . . .	81
6.2	Main Achievements . . . . .	89
<b>7</b>	<b>Conclusion and Outlook</b>	<b>91</b>
7.1	Future Directions . . . . .	93
	<b>References</b>	<b>97</b>
	<b>Curriculum Vitae</b>	<b>125</b>

# List of Publications

Most of the results presented in this thesis have been published in peer-reviewed scientific journals. The three main publications are reproduced in their entirety with the permission of the corresponding journals. For the papers presented here, I planned the experiments, performed the majority of the experimental work and data analysis, and wrote the largest part of the manuscripts:

- P. Staudinger, S. Mauthe, K. E. Moselund, and H. Schmid, “Concurrent Zinc-Blende and Wurtzite Film Formation by Selection of Confined Growth Planes”, *Nano Letters*, **18**(12), 7856–7862 (2018)
- P. Staudinger, K. E. Moselund, and H. Schmid, “Exploring the Size Limitations of Wurtzite III–V Film Growth”, *Nano Letters*, **20**(1), 686–693 (2020)
- P. Staudinger, S. Mauthe, N. Vico Triviño, S. Reidt, K. E. Moselund, and H. Schmid, “Wurtzite InP Microdisks: from Epitaxy to Room-Temperature Lasing”, *under review in Nanotechnology*

In the scope of this thesis I wrote an invited article for a popular science magazine and filed 3 patent applications:

- P. Staudinger, K. E. Moselund, and H. Schmid, “Crystal phase tuning creates new functionality”, *Compound Semiconductor Magazine*, **1/2**, (2020)
- P. Staudinger, H. Schmid, "Method for planar layers of metastable material phases", *United States Patent Office*, 16/926850 (2020)
- N. Vico Triviño, P. Staudinger, S. Mauthe, K. E. Moselund, "Method to fabricate a III-V spherical resonator", *United States Patent Office*, 16/573309 (2019)
- Y. Baumgartner, L. Czornomaz, P. Staudinger, H. Schmid, "Fabrication of semiconductor substrates", *United States Patent Office*, 16/127669 (2018)

## List of Publications

---

At the same time I contributed to several other projects, which are not included in this thesis. A continued collaboration with the group of A. Lugstein at TU Wien resulted in the following journal publications:

- P. Staudinger, M. Sistani, J. Greil, E. Bertagnolli, and A. Lugstein, "Ultrascaled Germanium Nanowires for Highly Sensitive Photodetection at the Quantum Ballistic Limit", *Nano Letters*, **18**(8), 5030–5035 (2018)
- M. Sistani, P. Staudinger, J. Greil, M. Holzbauer, H. Detz, E. Bertagnolli, and A. Lugstein, "Room-temperature Quantum Ballistic Transport in Monolithic Ultrascaled Al-Ge-Al Nanowire Heterostructures", *Nano Letters*, **17**(8), 4556–4561 (2017)
- R. Böckle, M. Sistani, P. Staudinger, M. S. Seifner, S. Barth, and A. Lugstein, "Ge Quantum Wire Memristor", *Nanotechnology*, accepted manuscript (2020)
- M. Sistani, P. Staudinger, and A. Lugstein, "Polarity Control in Ge Nanowires by Electronic Surface Doping", *under review*
- N. Gächter, F. Könemann, M. Sistani, M. G. Bartmann, M. Sousa, P. Staudinger, A. Lugstein, and B. Gotsmann, "Spatially Resolved Thermoelectric Effects in operando Semiconductor-Metal Nanowire Heterostructures", *under review*

For further collaborations, I contributed by performing clean room processing, MOVPE growth and STEM characterization (selection):

- C. Convertino, C. B. Zota, Y. Baumgartner, P. Staudinger, M. Sousa, S. Mauthe, D. Caimi, L. Czornomaz, A. M. Ionescu, and K. E. Moselund "Sub-Thermionic Scalable III-V Tunnel Field-Effect Transistors Integrated on Si (100)", *IEEE International Electron Devices Meeting (IEDM)* (2019)
- B. F. Mayer, S. Wirths, S. Mauthe, P. Staudinger, M. Sousa, J. Winiger, H. Schmid, and K. E. Moselund, "Microcavity Lasers on Silicon by Template-Assisted Selective Epitaxy of Microsubstrates", *IEEE Photonics Technology Letters*, **31**(13), 1021-1024 (2019)
- N. V. Triviño, P. Staudinger, N. Bologna, H. Riel, K. Moselund, and H. Schmid, "III-V Vertical Nanowires Grown on Si by Template-assisted Selective Epitaxy for Tandem Solar Cells", *OSA Publishing* (2019)
- S. Mauthe, P. Staudinger, N. V. Trivino, M. Sousa, T. Stöferle, H. Schmid, and K. E. Moselund, "Monolithically Integrated InP-on-Si Microdisk Lasers with Room-Temperature Operation", *OSA Publishing* (2019)
- D. Busse, E. Fadaly, V. T. van Lange, J. R. Suckert, A. Dijkstra, M. van Tilburg, C. Rödl, P. Staudinger, M. A. Verheijen, S. Kölling, D. Ziss, J. Furthmüller, F. Bechstedt, J. Stangl, H. Schmid, S. Botti, E. P. A. M. Bakkers, J. E. M. Haverkort, and J. J. Finley, "Towards a photonic band edge laser using hexagonal-SiGe nanowire arrays", *SPIE* (2020)

# List of Figures and Tables

1.1	Band gap energy of commonly used elemental and compound semiconductors for the cubic and hexagonal phase . . . . .	3
1.2	State of the art of metastable crystal growth in semiconductors . . . . .	5
1.3	From nanowire to film growth – new epitaxy strategies developed during the course of this thesis . . . . .	6
2.1	Unit cells of zinc-blende and wurtzite crystals . . . . .	10
2.2	Overview of crystal structures in cubic (3C) and hexagonal (2H) symmetries .	11
2.3	Twinning in III-V semiconductors . . . . .	13
2.4	First Brillouin zones for FCC and HCP crystal symmetries . . . . .	14
2.5	Electronic band structure of ZB and WZ InP . . . . .	15
2.6	Band gap energy of III-V semiconductors in ZB and WZ phase as well as Si and Ge in D and LD phase . . . . .	17
2.7	Electronic band structures of LD Si and Ge along with the minima at various high symmetry points for LD $\text{Si}_{1-x}\text{Ge}_x$ as a function of Ge content . . . . .	18
2.8	Schematic representation of MOVPE for III-V growth . . . . .	19
2.9	Antiphase boundary formation for crystal structure mismatched epitaxy . . .	21
2.10	VLS growth mechanism . . . . .	22
2.11	Selective area epitaxy of NWs . . . . .	23
2.12	Epitaxy of fins (SAE) and planar layers (ELO) . . . . .	24
2.13	Top-view schematic of zipper growth modes . . . . .	25
2.14	Conformal epitaxy of layers . . . . .	26
2.15	Local bonding configuration in ZB and WZ structures . . . . .	27
2.16	Bulk energy difference between the ZB and WZ crystal structure in dependence of ionicity . . . . .	28

## List of Figures and Tables

---

2.17	ZB and WZ crystals viewed along the typical growth direction (c-axis) . . . . .	29
2.18	Side-view of a catalyst droplet on top of a NW, showing two different ways of new nuclei to be formed . . . . .	31
2.19	Principle of crystal orientations, phase change and stacking transfer . . . . .	32
2.20	Concepts for epitaxy of WZ fins and planar layers . . . . .	33
3.1	Fabrication steps for conformal epitaxy . . . . .	36
3.2	CE templates before and after growth . . . . .	37
3.3	Atomistic model of possible low-index facet formation during CE . . . . .	38
3.4	Fabrication steps for zipper-induced epitaxial lateral overgrowth . . . . .	39
3.5	Mechanism of zipper-induced epitaxial lateral overgrowth . . . . .	40
3.6	Simplified schematic of a typical STEM setup . . . . .	41
3.7	Schematic representation of the $\mu$ -PL setup used for this work . . . . .	43
4.1	Table of contents figure . . . . .	47
4.2	Experimental implementation of confined growth planes . . . . .	49
4.3	STEM investigation of an InP crystal grown along $\langle 100 \rangle$ . . . . .	50
4.4	STEM investigation of InP films grown along $\langle 110 \rangle$ . . . . .	51
4.5	Simultaneous growth of ZB and WZ InP layers . . . . .	52
4.6	PL measurements of ZB and WZ InP films . . . . .	53
4.7	End facets and atomistic model for structural transition . . . . .	54
4.8	HR-STEM image of the phase transition in an InP crystal grown along $\langle 110 \rangle$ -direction . . . . .	57
4.9	Room temperature CL characterization of a crystal grown along $\langle 110 \rangle$ -direction . . . . .	58
4.10	STEM investigation of InP and GaAs films . . . . .	59
4.11	Two step epitaxy technique for synthesizing WZ GaAs films . . . . .	60
4.12	STEM characterization of a WZ GaAs film . . . . .	60
5.1	STEM characterization of InP-InAlP core-shell fins . . . . .	63
5.2	Table of contents figure . . . . .	65
5.3	From nanowire to film growth for large area WZ structures . . . . .	68
5.4	HAADF-STEM and PL characterization of a zipper-ELO hexagon . . . . .	69
5.5	Scaling behavior of InP structures . . . . .	71
5.6	Atomistic model for size-dependent structural transitions in III-V SAE . . . . .	72

5.7	SEM images of zipper-ELO structures . . . . .	75
5.8	30° tilted SEM images of InP crystals grown in hexagonal holes with increasing diameter . . . . .	76
5.9	3D schematic of zipper-ELO . . . . .	76
5.10	SEM images of InP fins with increasing length . . . . .	77
5.11	STEM characterization of an InP fin with 300 $\mu\text{m}$ length . . . . .	78
6.1	Table of contents figure . . . . .	82
6.2	Concept for WZ InP microdisk epitaxy . . . . .	84
6.3	Growth of structures with different feature sizes and geometries applicable to photonic devices . . . . .	85
6.4	HAADF-STEM characterization of a representative microdisk . . . . .	86
6.5	Optical characterization and lasing in a WZ InP microdisk . . . . .	87
7.1	Qualitative map showing the techniques and results presented in this thesis compared to the state of the art for growth of metastable materials . . . . .	93
7.2	Ideas for synthesizing a larger range of metastable materials . . . . .	94



# List of Acronyms

<b>ADF</b>	annular dark field	<b>FFT</b>	fast Fourier transform
<b>AFM</b>	atomic force microscopy	<b>FIB</b>	focused ion beam
<b>ALD</b>	atomic layer deposition	<b>FWHM</b>	full width at half maximum
<b>APB</b>	antiphase boundaries	<b>HAADF</b>	high angle annular dark field
<b>BF</b>	bright field	<b>HCP</b>	hexagonal close-packed
<b>BG</b>	band gap	<b>HF</b>	hydrofluoric acid
<b>BHF</b>	buffered hydrofluoric acid	<b>HR</b>	high-resolution
<b>CB</b>	conduction band	<b>HSQ</b>	hydrogen silsesquioxane
<b>CCD</b>	charge-coupled device	<b>ICP</b>	inductively coupled plasma
<b>CE</b>	conformal epitaxy	<b>LD</b>	lonsdaleite
<b>CELO</b>	confined epitaxial lateral overgrowth	<b>LED</b>	light-emitting diode
<b>CL</b>	cathodoluminescence	<b>LL</b>	light in light out (curve)
<b>CMOS</b>	complementary metal-oxide-semiconductor	<b>LPE</b>	liquid phase epitaxy
<b>D</b>	diamond (crystal structure)	<b>MBE</b>	molecular beam epitaxy
<b>DHF</b>	diluted hydrofluoric acid	<b>MCE</b>	microchannel epitaxy
<b>EBL</b>	e-beam lithography	<b>MFC</b>	mass flow controller
<b>EDX</b>	energy-dispersive x-ray	<b>MOCVD</b>	metal-organic chemical vapor deposition
<b>ELO</b>	epitaxial lateral overgrowth	<b>MOVPE</b>	metal-organic vapor phase epitaxy
<b>FCC</b>	face-centered cubic	<b>NW</b>	nanowire
		<b>PD</b>	planar defect

## List of Acronyms

---

<b>PECVD</b>	plasma-enhanced chemical vapor deposition	<b>TBAs</b>	tertiarybutylarsenine
<b>PL</b>	photoluminescence	<b>TBP</b>	tertiarybutylphosphine
<b>RF</b>	radio frequency	<b>TCSPC</b>	time-correlated single photon counting
<b>RIE</b>	reactive ion etching	<b>TEM</b>	transmission electron microscopy
<b>RT</b>	room temperature	<b>TEOS</b>	tetraethyl orthosilicate
<b>RTW</b>	rotational twin	<b>TMGa</b>	trimethylgallium
<b>SAE</b>	selective area epitaxy	<b>TMIn</b>	trimethylindium
<b>SAG</b>	selective area growth	<b>TPL</b>	triple phase line
<b>SEM</b>	scanning electron microscopy	<b>TRPL</b>	time resolved photoluminescence
<b>SF</b>	stacking fault	<b>UHV</b>	ultrahigh vacuum
<b>SOI</b>	silicon-on-insulator	<b>VB</b>	valance band
<b>STEM</b>	scanning transmission electron microscopy	<b>VLS</b>	vapor liquid solid (growth)
<b>TASE</b>	template-assisted selective epitaxy	<b>VS</b>	vapor solid (growth)
		<b>WZ</b>	wurtzite
		<b>ZB</b>	zinc-blende

# 1 Introduction

*“Scientists discover the world that exists;  
engineers create the world that never was.”*

– Theodore von Kármán

Throughout human history novel materials have been at the heart of technological progress and cultural evolution. Be it through discovery or by advancement in understanding and manufacturing, numerous examples exist in which the availability of new matter significantly impacted the way humans lived and developed. It is thus not a coincidence that the prehistoric periods of civilization have been classified into stone, bronze and iron age – with each new era being brought about by a new material [1]. Many disruptive innovations that followed in modern times were enabled by development of new substances. From steel to concrete, from ceramics to glass, from polymers to synthetic fibers: the story of human progress is a story of materials [2].

There is one class of matter that like no other has shaped technological advancement during the last century – semiconductors. The availability of pure and crystalline silicon and germanium, together with theoretical progress in quantum physics, has led to the development of transistors in 1947 [3] and integrated circuits in the late 1950s [4]. The digital revolution that followed impacted our lives in ways so deep that it has become difficult to imagine a world without it. Computers, smartphones, telecommunication and the internet have driven not only the globalization with all its implications [5]. From modern cars over solar cells to medical equipment or GPS – digital electronics underpins practically everything we take for granted nowadays in our interconnected digital world. No wonder this era has been named *silicon age* [6].

More recently, III-V semiconductors have increasingly gained importance due to their superior electronic and optoelectronic properties [7]. High electron mobilities enabled the development of RF transistors that are used for example in transceivers for wireless communication [8] or radar technologies [9]. Direct band gap transitions in many III-Vs such as GaAs or InP further enabled the development of light emitting diodes (LEDs) [10] and semiconductor lasers [11]. These devices are now the basis for optical fiber communication [12], which constitutes a substantial part of all global data transfer [13]. The continuous development of

III-nitrides has revolutionized the lighting market by introducing energy-efficient blue and ultraviolet LEDs [14, 15] thereby trimming the global energy consumption [16]. Besides the plentiful examples of existing technologies, III-Vs and nanostructures made thereof are still evaluated for novel applications so diverse that they include both high efficiency solar cells [17, 18, 19, 20, 21] and next generation qubits for quantum computing [22, 23, 24].

Today we see an increasing number of materials being studied and finding applications in new technologies. The accelerated advancement in materials science is to a large part owed to the fast progress in computational methods and simulations that help us to understand and predict certain properties [25]. On the search of new matter, different avenues can be followed. Screening possible combinations of elements is certainly one of them. A more subtle approach is to rearrange the atoms in an existing material and thereby change its crystal structure. In this way the physical properties of abundant and well-studied semiconductors can be fine-tuned, while making only minimal changes to their chemistry, which provides the advantage that established fabrication technology can still be used in existing fabs. We call this approach *crystal phase engineering* and shall follow it during this thesis.

### 1.1 Crystal Phase Engineering – on the Search for New Materials

There are two basic parameters that define a material. The atoms from which it is constituted and how these atoms are arranged in space. Many materials are formed from the same elements but have dissimilar crystalline structures, so-called crystal phases. This circumstance is referred to as polymorphism [26, 27]. Polymorphs or allotropes, as they are called in elemental crystals, can have substantially different physical properties as becomes clear by comparing for example diamond with graphite [28]. For compound semiconductors, two predominant forms exist: the cubic zinc-blende (ZB) and the hexagonal wurtzite (WZ) phase [29]. For each material one form is thermodynamically preferred and is thus referred to as stable configuration or phase. However the activation energy for atomic rearrangement is so high, that once the non-stable polymorph is synthesized it effectively remains stable under standard conditions [30]. Hence, we will refer to the thermodynamically less preferred configuration as metastable phase [31]. The formation of a metastable phase can for example take place under extreme conditions. It took a meteorite impact to discover the WZ-like allotrope of diamond in 1967 [32]. Lonsdaleite, as this material was named, has later been synthesized in a controlled way [33, 34] and is now believed to be the hardest known substance [35, 36]. In correspondence to the cubic diamond crystal structure (D) of elemental semiconductors we will refer to their hexagonal phase as lonsdaleite (LD) [37].

Many metastable phases of conventional semiconductors have been theoretically predicted to exhibit beneficial properties compared to their stable counterparts. III-Vs for example, are known to be efficient light emitters in the infrared [38] and red [39], however their performance drops drastically upon approaching the orange-yellow wavelength regime [40]. The underlying reason is the indirect nature of AlP and GaP and the related band crossing of InAlGaP at Al-

or Ga-rich conditions [41]. In contrast, theory predicts that the entire composition spectrum of the metastable WZ InAlGaP compound exhibits a direct band gap transition [42]. This class of materials could thus provide a solution to the so-called *green gap* problem – the lack of efficient light emitters in the center of the visible wavelength regime [43, 44, 45]. This circumstance is best described in Fig. 1.1, which depicts band gap energies along with the tunable direct range for conventional semiconductors in stable and metastable phases.

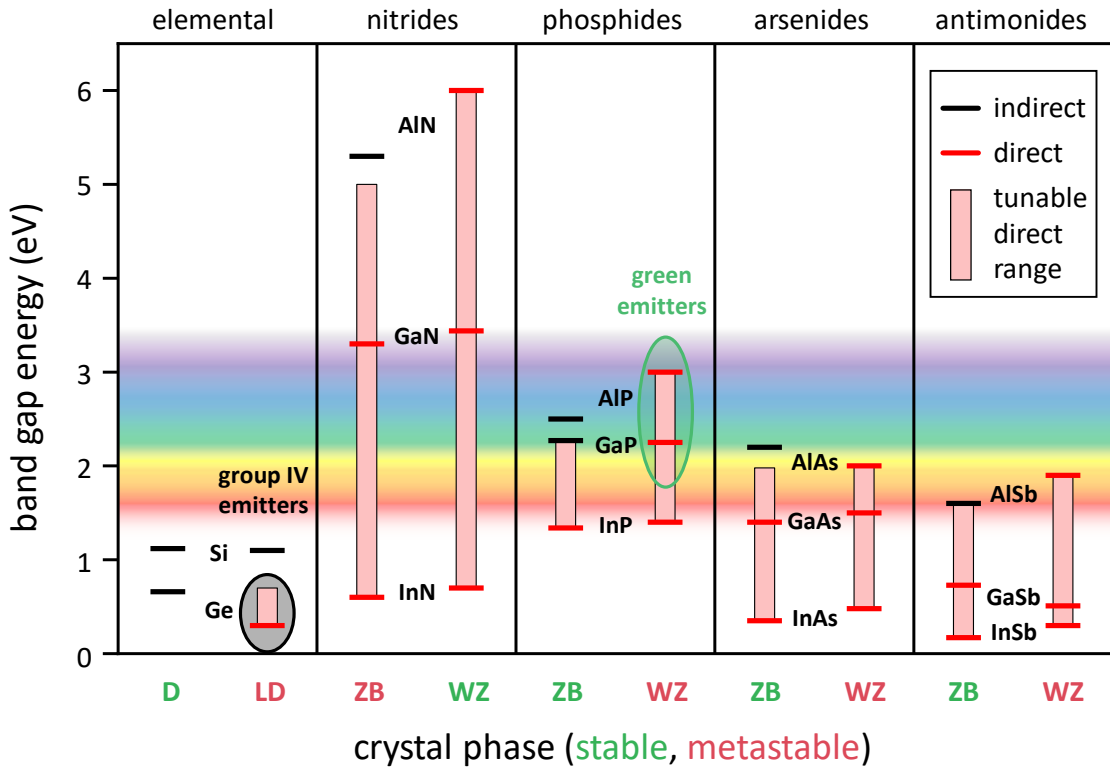


**Figure 1.1** | Band gap energy of commonly used elemental and compound semiconductors for the cubic and hexagonal phase. Hexagonal materials generally offer a wider range of direct band gap. Data taken from [42, 46, 47, 48, 49].

III-nitrides on the other hand, in their stable WZ phase, are known to be plagued by strong internal electrical fields [50]. GaN/InGaN heterostructures, such as they are commonly used in blue LEDs, are consequently susceptible to the so-called quantum confined Stark effect, the spatial separation of electron and hole wavefunctions within a quantum well [51, 52, 53]. As a result their efficiency decreases, especially upon increasing the indium content, which is necessary to obtain a band gap that allows for green emission [54]. ZB III-nitrides could pose another solution to the *green gap* problem, due to the predicted absence of internal electrical fields in this crystal phase [55, 56].

The integration of a material that exhibits efficient interaction with light into the mature CMOS technology is of enormous technological interest. Optical interconnects could provide a possible solution to the interconnect bottleneck that is limiting the performance of state of the art integrated circuits [57]. Tremendous efforts are being made to demonstrate integration of

active III-V devices on Si, either through direct growth [58] or wafer bonding [59]. Undoubtedly, a much more elegant approach would be to use Si itself to build these device, however Si and the technologically compatible SiGe alloys are all indirect band gap semiconductors that cannot emit light efficiently. At least this is true for their stable cubic crystal phase. Theory predicts that Ge, and with it Ge-rich SiGe alloys, become direct upon phase-change to the LD structure [60, 61, 62], as illustrated in Fig. 1.1. Hence, they are an ideal system to unite electronic and optoelectronic functionalities on a single chip.

Promising theoretical predictions have triggered intense research interest in synthesizing these metastable materials. Large progress was made especially by using the physics of nanocrystals which are elongated along one dimension – so-called nanowires (NWs). The challenge resides on the growth in a phase-controlled way, which allows for effective *crystal phase engineering* of optoelectronic properties.

### 1.2 State of the Art – Synthesis of Metastable Crystal Phases

Soon after the vapor-liquid-solid growth (VLS) mechanism was described by Wagner and Ellis in 1964 [63], it has been observed that many of the III-V materials grown by this principle exhibit an unusual crystal structure. InAs NWs or whiskers, as they have been called back then, crystallized in the metastable WZ phase that switched back to ZB upon annealing to 800°C [64]. Since then, tremendous advances were made both experimentally as well as theoretically. A large range of metastable materials can now readily be synthesized with high quality by VLS, including most commonly used binary materials as indicated in Tab. 1.2. III-antimonides and elemental semiconductors show less phase-control due to their lower ionicity as will be explained in **Section 2.6**. Instead these materials have often been synthesized by transferring the crystal structure from a core NW to its shell. This has proven especially successful in the case of SiGe alloys, which can now be grown in very high quality [65, 66]. Increasing understanding of the growth dynamics helped to develop accurate models that describe the role of the catalyst for the formation of WZ III-Vs [67, 68, 69, 70, 71, 72, 73]. This knowledge is now used for controlled switching between stable and metastable crystal phases to create heterostructures with interesting properties [74, 75, 76, 77, 78, 79]. The deliberate synthesis of twinning super lattices with long-range order in InP [80], InAs [81, 82] and GaAs [83, 84] further demonstrates the superior crystal phase control that can be achieved by this technique.

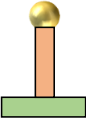
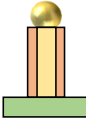
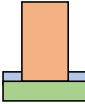

Even though ZB III-nitrides have been synthesized by VLS, other techniques have proven more useful to stabilize the cubic crystal structure. By using GaAs(001) substrates it has been shown that the crystal phase can be effectively transferred to a GaN film, despite the large lattice mismatch [85]. As indicated in Tab. 1.2, related materials soon followed. To bring cubic nitrides closer to application, efforts have shifted towards the direct growth on Si substrates [86, 55].

Using the same principle for stabilizing the hexagonal phase in III-V materials seems more difficult. To the best of our knowledge, only one study exists in which highly defective WZ InAlP has been grown on m-plane GaN substrates. However, significant advances were made in the

## 1.2. State of the Art – Synthesis of Metastable Crystal Phases

catalyst-free synthesis of InP [105] and related ternaries such as AlInP [106] and InGaP [107], which can be seen as an intermediate step concerning technological maturity. By growing InP fin structures [108], the first steps towards large-area substrates were made, however still lacking a planar geometry as desired for many device applications.

**Table 1.2** | State of the art of metastable crystal growth in semiconductors (ZB for III-N, LD for IV, WZ otherwise), divided by technique and material system. *VLS* includes self catalyzed growth. *Shell growth* refers to the crystal structure transfer from a metastable core NW. *Catalyst free* growth includes any technique without catalyst particle that does not result in *planar films*. Green background color stands for high crystal phase control for a large range of materials with good crystalline quality. Yellow indicates either a limited amount of materials or less phase control. Red colored entries show metastable material formation only locally or with large amounts of defects. Typically only one source is given for each material, even though in many cases multiple independent studies exist. For missing entries no appropriate source has been found.

	VLS 	shell growth 	catalyst free 	planar film 
III-N (ZB)	GaN [87], InN [88]	—	GaN [89], InN [90], AlGaIn [91], InGaIn [86]	AlN [92], GaN [93, 94, 95], AlGaIn [96], InGaIn [97]
III-P (WZ)	GaP [98], InP [99]	GaP [100], InP [101], AlGaP [102], AlInP [103], InGaP [104]	InP [105], AlInP [106], InGaP [107], InP fins [108]	AlInP on GaN substrate [109]
III-As (WZ)	AlAs [110], GaAs [111], InAs [112]	GaAs [113], InAs [114], AlGaAs [115], AlInAs [116], InGaAs [117]	GaAs [118], InAs [119], InGaAs [120]	—
III-Sb (WZ)	InSb [121, 122, 123, 124]	AlSb [125], GaSb [126]	—	—
other III-V (WZ)	GaAsP [127], InPSb [128], InAsP [129], InAsSb [130]	GaAsP [131], GaAsSb [132], InAsSb [133]	—	—
IV (LD)	Si [134, 135, 136, 137], Ge [138, 139, 140]	Si [141], Ge [66], SiGe [65]	—	—

### 1.3 Epitaxy Strategies for Metastable Films – beyond Nanowire Size Constraints

Nanowire growth is undoubtedly the technique which is most explored and versatile for the synthesis of metastable phases. For many applications such as solar cells [142], chemical sensors [143] or quantum devices [144], their unique properties have also distinctive advantages. To explore the rich potential of these new materials however, larger crystals are required, for example to form high quality optical cavities. A planar form factor is especially desirable, as it allows for conventional fabrication of lateral devices using state of the art processing and lithography techniques. During this thesis we will develop two distinctive approaches that

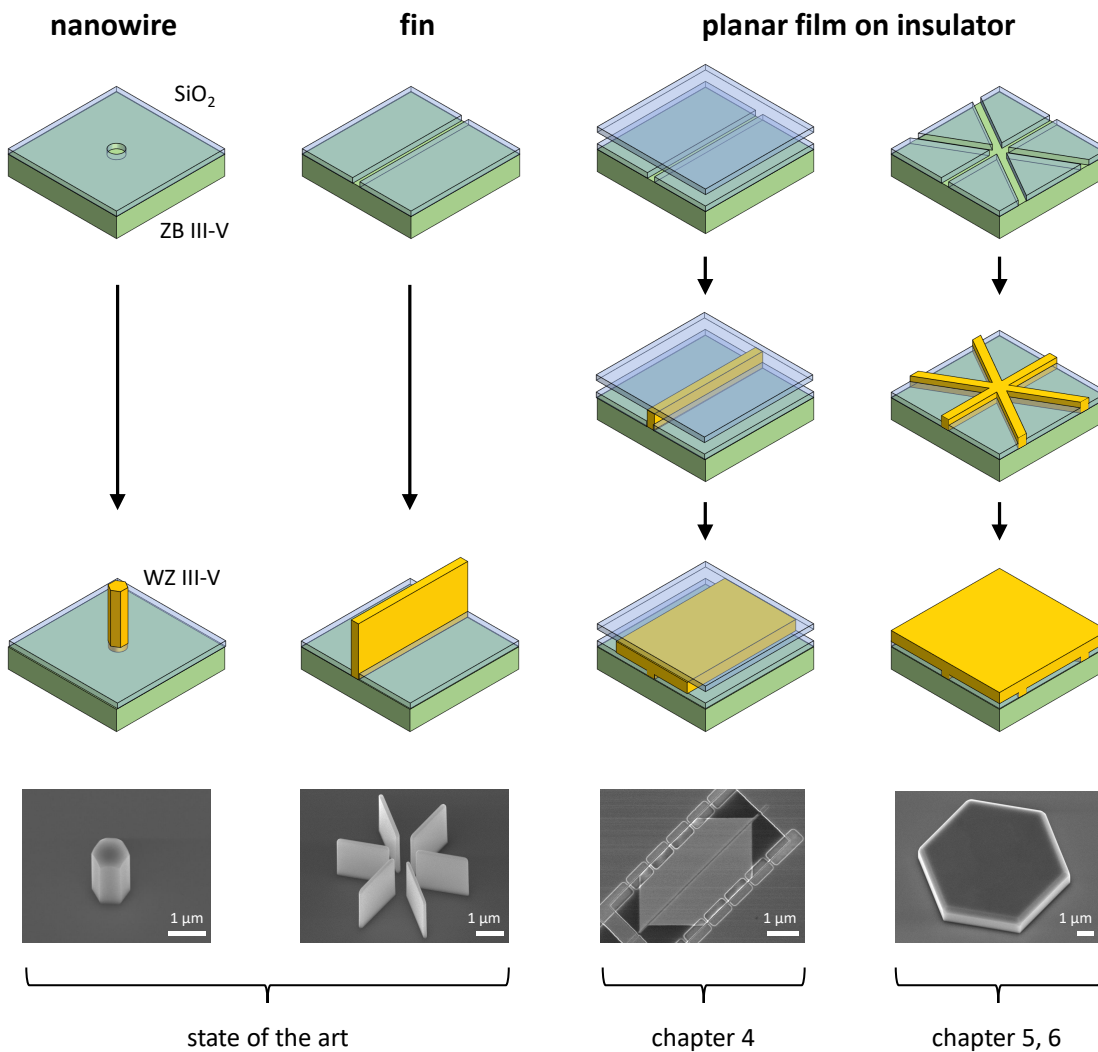


**Figure 1.3** | From nanowire to film growth – new epitaxy strategies developed during the course of this thesis. Selective area epitaxy of nanowires and fins is used as basis for more advanced techniques that result in metastable films. Bottom row depicts SEM images of WZ InP structures that have been synthesized throughout this research project.

allow for the formation of metastable planar films on insulator. Starting from state of the art selective area growth techniques that result in NWs and fins we explore the usage of a capping oxide and zipper-points to induce lateral overgrowth as indicated in Fig. 1.3. The challenge is to form and stabilize a metastable phase in such layers. Special care needs thus to be taken on crystalline directions, the formation of particular facets during growth and the reactor conditions.

## 1.4 Scope and Structure of this Thesis

In the framework of this thesis we will investigate phase transitions in nanostructures, what triggers their formation and how they can be stabilized. The objective is to develop new epitaxy strategies for the synthesis of metastable materials in layers that are compatible to conventional semiconductor processing techniques, thus bringing them closer to application. Even though the main goal is to grow high quality material that is useful for device applications, the availability of such phases in form factors in which bulk properties dominate is also very interesting from a fundamental point of view. For the first time certain properties of metastable semiconductors can be tested unambiguously. Special emphasis is given to optoelectronic properties, which are particularly promising. The demonstration of lasing in WZ InP is a large step towards device applications and will be a further proof of the high material quality that has been achieved. To explore properties of LD group IV materials, a collaboration with the E.P.A.M. Bakkers group at TU Eindhoven has been established. Large area WZ films should serve as a virtual substrate for crystal phase transfer to SiGe alloys in analogy to shell growth on NWs. During the following chapters we will introduce the theoretical background needed to carry out this research project, followed by detailed descriptions of the applied experimental methods and obtained results. In particular this thesis is structured as follows:

### Chapter 1: Introduction

In the first chapter the topic has been introduced and placed in a wider scientific context.

### Chapter 2: Semiconductor Crystals in Stable and Metastable Phases

The second chapter provides a theoretical overview of crystal structures and defects in semiconductors. We will address peculiarities of metastable crystal phases, their properties and how they can be synthesized, with special focus on wurtzite III-V materials. Various growth techniques are reviewed and first strategies towards film formation developed.

### Chapter 3: Experimental Methods

In this chapter the experimental methods which are relevant for this thesis are presented. Starting from substrate preparation, we will discuss crystal growth and in particular address

## Chapter 1. Introduction

---

considerations for synthesis of metastable phases. Further, the main characterization techniques applied in this research project will be reviewed.

## Chapter 4, 5 and 6: Results and Discussion

Chapter 4-6 provide the main results of this thesis. **Chapter 4** is dedicated to describe conformal epitaxy as a first strategy for metastable film formation. In particular the effects of selecting confined growth planes will be explored as a basis for understanding phase transitions during film epitaxy. The most important result is the concurrent and defined formation of zinc-blende and wurtzite layers with high quality, during the same growth run. **Chapter 5** introduces zipper-induced epitaxial lateral overgrowth as another avenue to grow metastable layers. In this work we will explore the size limitations and demonstrate the largest ever grown WZ III-V crystals. A theoretical model is developed to explain our experimental observations. **Chapter 6** is dedicated to explore possible device applications for metastable materials. A growth platform is developed which allows for precise positioning of microdisks and related geometries, combining advantages of top-down with bottom-up techniques. Optical isolation of these structures allows for demonstration of the first WZ InP microdisk laser operated at room temperature. For every chapter we first give a short introduction, followed by an article which has been published in a peer-reviewed scientific journal.

## Chapter 7: Conclusion and Outlook

The last chapter provides a conclusion of the thesis followed by an outlook for future developments.

## 2 Semiconductor Crystals in Stable and Metastable Phases

*“Nothing in life is to be feared, it is only to be understood.  
Now is the time to understand more, so that we may fear less.”*

– Marie Skłodowska Curie

This chapter provides the fundamentals of crystal structures, physical properties and epitaxial growth of semiconductors. We will address peculiarities of metastable crystal phases, their properties and how they can be synthesized, with special focus on wurtzite III-V materials. This chapter is not exhaustive, it rather focuses on certain topics that are relevant for this thesis and motivates the results which will be presented in chapters 4-6.

### 2.1 Crystal Structure

One of the main objectives of this thesis is to explore the synthesis and properties of metastable crystal phases in semiconductors. A basic understanding of the crystallography of this kind of matter is therefore crucial in order to obtain insights on what drives their formation and why their properties differ from their stable counterparts. There are two predominant crystal structures to consider: Zinc-blende and wurtzite. As depicted in Fig. 2.1 they are described using two different Bravais lattices and base sets per unit cell. The ZB structure can be defined by one lattice parameter  $a_{\text{ZB}}$ , which corresponds to the edge length of its cubical unit cell. The lattice consists of two interpenetrating face-centered cubic (FCC) sublattices shifted by  $\sqrt{3}a_{\text{ZB}}$  along the diagonal. A base set of two atoms defines the population of these sublattices, such as e.g. In and P for indium phosphide (InP). In the case of an elemental semiconductor like Si or Ge, both atoms are of the same type and the corresponding crystal structure is referred to as diamond.

WZ on the other hand, is created from a base set of four atoms associated with a hexagonal lattice. Two lattice parameters are required to define this structure:  $a_{\text{WZ}}$  being the edge length and  $c_{\text{WZ}}$  being the height of the parallelepiped depicted in Fig. 2.1(b). The internal parameter

$u_{WZ}$  defines the bond length along the  $c$ -axis. For an ideal unit cell, the ratio of  $c_{WZ}$  and  $a_{WZ}$  calculates to  $c_{WZ}/a_{WZ} = \sqrt{8/3}$  and the internal parameter  $u_{WZ}$  has a value of  $u_{WZ} = 3/8c$ . Each of the two individual atom types forms a sublattice of the type hexagonal close-packed (HCP). WZ crystal structure is favored by some III-nitrides, such as gallium nitride (GaN) and II-VI compounds, such as zinc oxide (ZnO) [145]. Elemental semiconductors adopting this configuration have been experimentally verified only recently in the form of NWs [146, 134, 141, 147]. In this case we call their crystal structure lonsdaleite, named after the corresponding allotrope of carbon [32, 46].

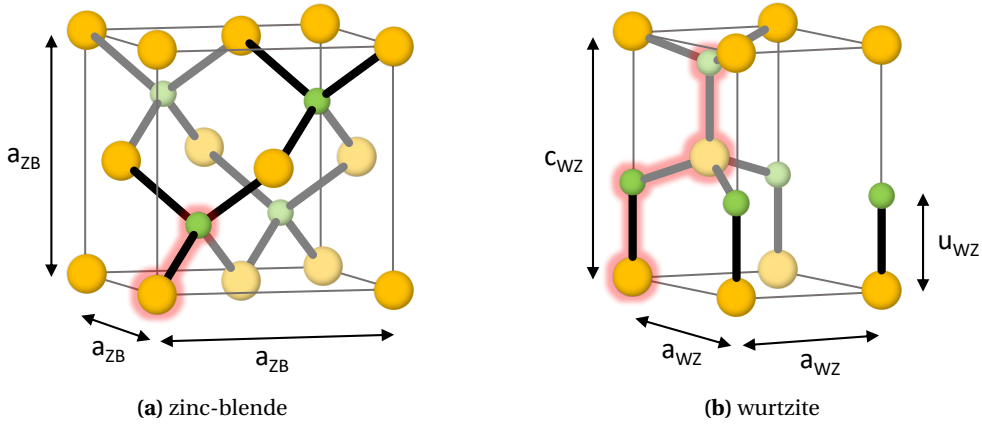


**Figure 2.1** | Unit cells of (a) zinc-blende and (b) wurtzite crystals along with their lattice parameters and internal parameter  $u_{WZ}$ . Yellow and green spheres represent atoms of group III and V, respectively. Bold lines indicate nearest-neighbor bonds. Atoms highlighted in red constitute the base set of the primitive unit cell.

Despite the fundamentally dissimilar crystal families – cubic and hexagonal – of the ZB and WZ structures, they have very much in common, which becomes more evident when we orient the cubic  $\langle 111 \rangle$ -direction along the  $z$ -axis as it is done in Fig 2.2. Looking at pairs of vertically aligned atoms, the remaining difference of these two structures resides on the bilayer stacking sequence along the so-called  $c$ -axis ( $\langle 111 \rangle$  for ZB and  $\langle 0001 \rangle$  for WZ, respectively). Whereas WZ follows an ABAB... stacking, ZB alternates between ABCABC... in a periodic way. Note that also more complicated stacking sequences exist e.g. in silicon carbide (SiC) [148]. In theory, all of these polytypes have equal bond lengths and bond angles between the nearest neighbors, which results in tetrahedrally coordinated atoms. Under this assumption the ideal lattice constants of WZ can be calculated for a given material [42]:

$$a_{WZ} = \frac{a_{ZB}}{\sqrt{2}}, \quad c_{WZ} = \frac{2a_{ZB}}{\sqrt{3}} \quad (2.1)$$

However, the slight changes in the stacking order result in very different symmetry properties. ZB has four threefold axes of rotation, which correspond to the  $\langle 111 \rangle$  room-diagonals of the cubical unit cell. The WZ lattice on the other hand only has one axis with threefold rotational symmetry –  $\langle 0001 \rangle$ . This has two important consequences: (1) The lower symmetry of the WZ

configuration together with the ionic bonding forces causes a shift of the individual atoms along the  $c$ -axis, which is described by using deviating  $c_{WZ}/a_{WZ}$ -ratios and  $u_{WZ}$ -values [149]. This has been experimentally verified [150] and is known to be the source of spontaneous polarization along the  $\langle 0001 \rangle$ -direction, which is not occurring in the ZB phase [151, 152]. (2) As a consequence the crystal field splitting results in a splitting of the valence bands for heavy and light holes at the  $\Gamma$ -point [153].

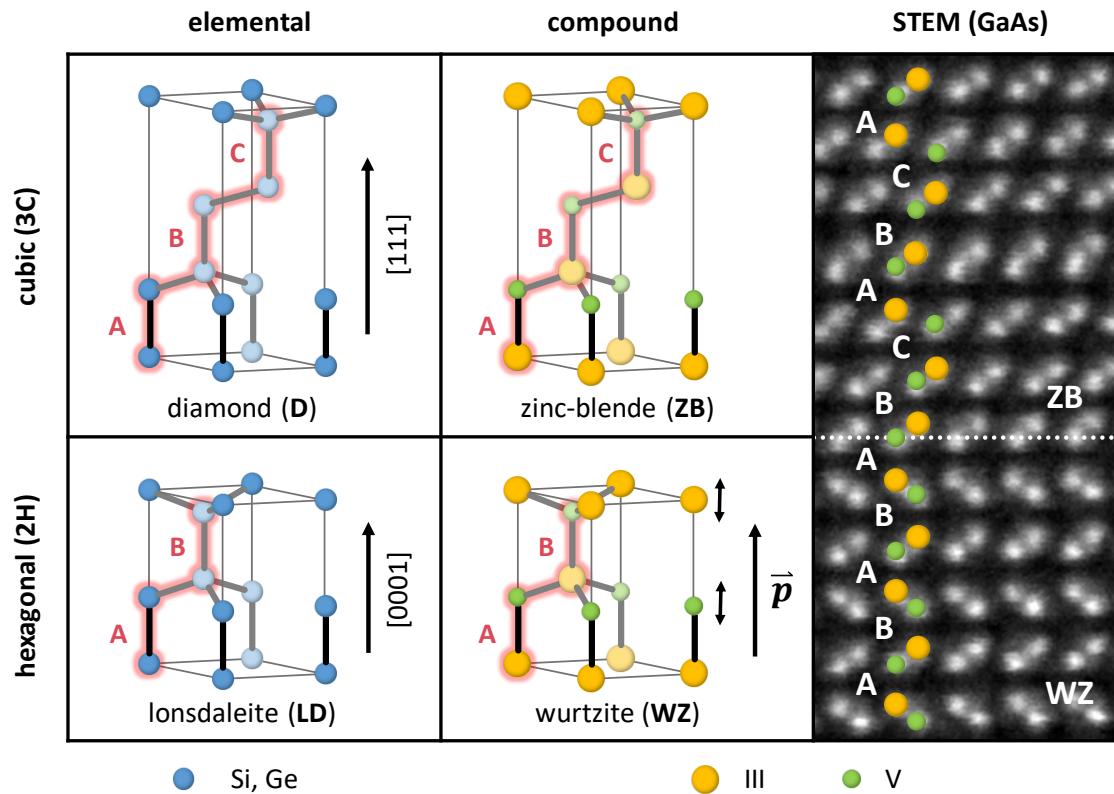


**Figure 2.2** | Overview of crystal structures in cubic (3C) and hexagonal (2H) symmetries for elemental and compound semiconductors. As opposed to Fig. 2.1(a), cubic symmetries are represented in an alternative way to highlight their similarities with the closely related 2H-family. The remaining difference is defined by the atomic bilayer stacking along the [111] or [0001] direction (ABC...vs. ABAB...). The crystal phase can be changed along this axis as exemplified in an HR-STEM image of polytypic GaAs.

A direct way to assess the crystal structure of semiconductor materials is by high-resolution scanning transmission electron microscopy (HR-STEM). If the zone-axis is aligned with a  $\langle 110 \rangle$ -direction for ZB or a  $\langle 11\bar{2}0 \rangle$ -direction for WZ, the stacking sequence perpendicular to this direction can be visualized directly. It should be noted that in a ZB structure, if the bilayer order is altered along another  $\langle 111 \rangle$ -direction that is not perpendicular to the selected  $\langle 110 \rangle$ -axis, the stacking sequence can not be observed unambiguously. The right hand side of Fig 2.2 depicts a micrograph of a polytypic GaAs crystal. The lower half shows the typical ABAB... stacking for WZ, whereas the upper part clearly depicts a ZB crystal with 3 alternating bilayers (ABC...). As this is a single image, it demonstrates the possibility of WZ and ZB phases

to coexist in a crystal with epitaxial relationship as long as this transition occurs along the *c*-axis. This property will be important when we will address growth and in particular phase transformations and phase transfer along specific growth orientations.

### 2.2 Defects

Until now, we have addressed the structural properties of ideal crystals. However in reality the arrangement of atoms in a lattice is not perfect and so called crystallographic defects exist. These imperfections are usually classified by their dimension into point (0 D), line (1 D), planar (2 D) and volume defects (3 D) [154]:

- (0 D) Point defects occur only around a single point in the lattice, without extending into space in any dimension. Typical examples include vacancy and interstitial defects, with a missing or an additional atom, respectively.
- (1 D) Line defects are lines through the crystal along which crystallographic registry is lost. It can be distinguished between edge and screw dislocations depending on whether the crystal planes are shifted perpendicular or parallel with respect to the defect line. In the case of heterojunctions, misfit edge dislocations are commonly found, originating from the lattice mismatch at the interface during epitaxial growth. They have a critical impact on the electrical performance of semiconductor devices and are thus highly undesirable.
- (2 D) Planar defects (PDs) include grain and antiphase boundaries (APBs), stacking faults (SF) and rotational twins (RTW). In ZB and WZ structures the latter two are especially important, because they can be easily formed along the stacking axis of the crystal. A SF is a local interruption in the stacking sequence. It can either be extrinsic when a layer is added (ABCBABC...) or intrinsic when one is missing (ABCBCABC...). In both cases the stacking order remains unaffected after the SF. A RTW in contrast induces an inversion of the ZB sequence around a so called twin plane (ABCACBA...), as schematically shown in Fig. 2.3. Note that even though the crystal structure is still ZB after the defect, a short WZ segment around the twin plane is formed. Hence, if such a RTW occurs at every stacking layer the crystal type changes completely from ZB to WZ [155]. From a geometrical point of view, a RTW can be seen as a rotation of the crystal by 60° around the  $\langle 111 \rangle$ -axis, thus maintaining the polarity in contrast to a mirror twin, which induces an antiphase boundary at the interface.
- (3 D) Volume defects are three-dimensional macroscopic or bulk defects. They are typically classified into precipitates (sub-micron particles), dispersants (intentionally introduced particles with a few micron in size), inclusions (undesired macroscopic particles) and voids (holes formed by trapped gases).

It is important to control all these imperfections, as they can significantly affect the physical

properties of the material and act as preferred sites for impurities or high diffusivity paths for dopants. The occurrence of SFs and RTWs can be seen as the transition from a cubic to a hexagonal phase. Manipulating them in a controlled way is therefore considered as one of the key elements for this thesis.

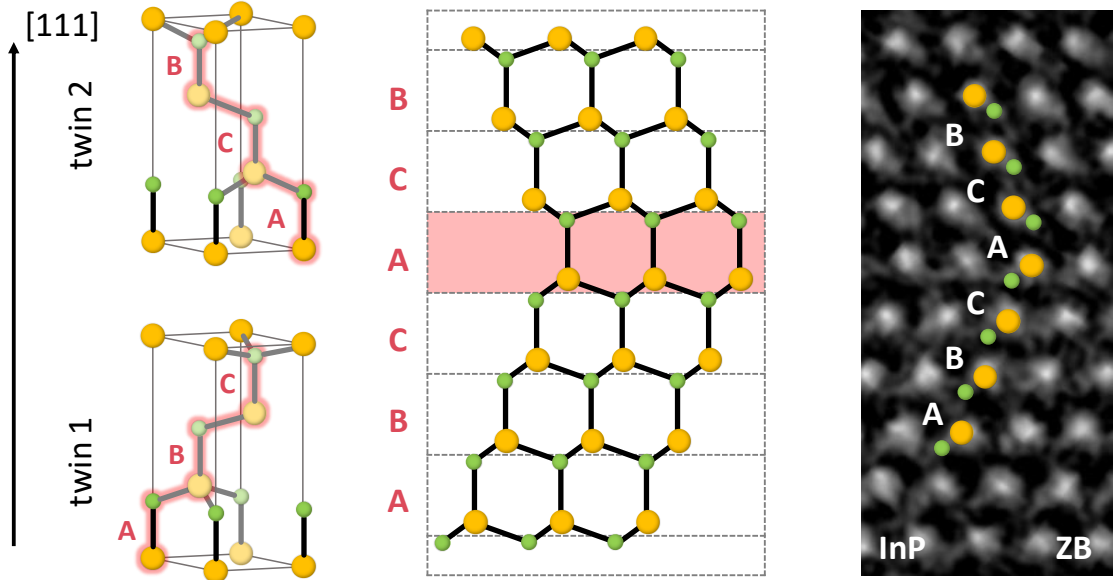


**Figure 2.3** | Twinning in III-V semiconductors. When two opposite twin orientations of ZB are combined, the common plane A is referred to as twin plane. An HR-STEM image depicts such a planar defect in an InP crystal. As opposed to GaAs depicted in Fig. 2.2, the size difference between In and P atoms is clearly noticeable.

## 2.3 Electronic Band Structure

The electronic band structure of a solid describes the energy range that is available for electrons moving within that material. This energy-momentum ( $E-k$ ) relationship is one of the most important concepts in solid state physics and indispensable especially to study semiconductor physics. Many electrical, optical, and even some magnetic properties of crystals can be understood in terms of the band structure. For example it is useful to explain interactions with photons and phonons, where energy and momentum have to be conserved [156]. Being able to tune the band structure of conventional materials is therefore a powerful tool for material scientists to enhance their properties and create new functionalities. Without modifying the composition of the respective material this can be achieved by inducing changes in the crystal symmetry, for example by applying strain, which essentially fine-tunes the atom-spacing within the lattice. Modifications under tensile or compressive strain are routinely exploited in order to improve the carrier mobility of Si(Ge) metal-oxide-semiconductor field-effect transistors [157, 158] or to modify the optical properties of III-V compounds [159, 160, 161]. In this work, we will address another way to alter the crystal symmetry of known materials. We synthesize them in a metastable phase. How this affects the electronic band structure will be

one of our main research questions.

To derive the band structure of a crystalline solid, the Schrödinger equation needs to be solved. This calculation constitutes a highly complex many-body problem for ZB and WZ crystal symmetries and solutions are obtained only by using a number of simplifications. For example, the valence electrons are considered individually and separately from the nuclei and the core electrons. Further, an average potential  $V(\mathbf{r})$  arising from the ionic lattice is treated as periodic in space with the crystal periodicity. The Bloch theorem states that under these assumptions the solutions for the wavefunction  $\psi(\mathbf{r}, \mathbf{k})$  of the Schrödinger equation

$$\left[ -\frac{\hbar^2}{2m^*} \nabla^2 + V(\mathbf{r}) \right] \psi(\mathbf{r}, \mathbf{k}) = E(\mathbf{k}) \psi(\mathbf{r}, \mathbf{k}) \quad (2.2)$$

are of the form of the Bloch function [156]

$$\psi(\mathbf{r}, \mathbf{k}) = \exp^{j\mathbf{k} \cdot \mathbf{r}} U_b(\mathbf{r}, \mathbf{k}) \quad (2.3)$$

where  $b$  is the band index. From the Bloch theorem, it can be shown that the solutions of the energy  $E(\mathbf{k})$  are periodic in the momentum space. In order to visualize the band structure of a crystal it is thus useful to look at the reciprocal lattice, that is, the Fourier transform of the crystal lattice in real space. As  $E(\mathbf{k})$  is periodic in the reciprocal lattice it is sufficient to consider the primitive cell, the smallest unit cell that represents the entire symmetry. The Wigner-Seitz construction is typically applied in order to obtain this so-called first Brillouin zone. Fig. 2.4 shows the Wigner-Seitz unit cells for FCC and HCP lattices, which correspond to the first Brillouin zones of ZB (and D) and WZ (and LD), respectively. High symmetry points at the surface are indicated by capital letters and the center is labeled with the Greek letter  $\Gamma$ .

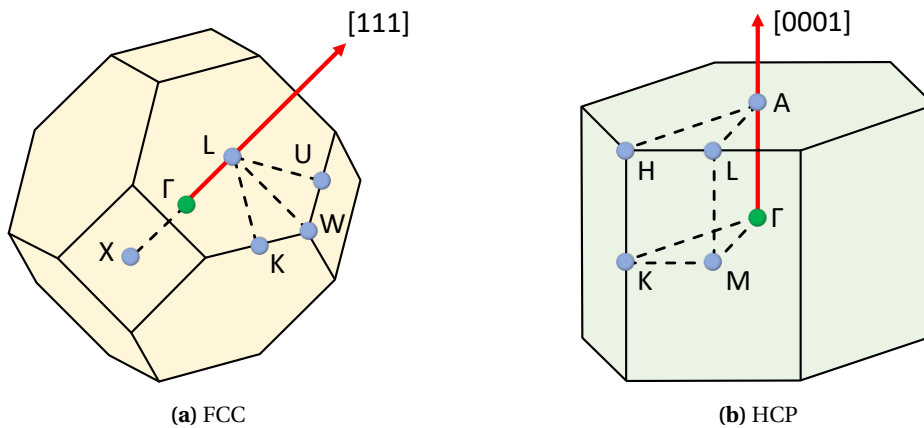


**Figure 2.4** | First Brillouin zones for (a) FCC and (b) HCP crystal symmetries. ZB and D have the FCC-type Brillouin zone, whereas WZ and LD can be described with the HCP-type. Letters indicate high symmetry points at the surface, and red arrows the direction of the crystal stacking axis.

Electronic band structures are typically plotted along lines that connect high symmetry points within the Brillouin zone [162].

The electronic band structure of III-V semiconductors has been studied theoretically using a variety of numerical methods yielding different levels of accuracy. The most frequently applied techniques include the orthogonalized plane-wave [163], the pseudopotential [164] and the  $\mathbf{k} \cdot \mathbf{p}$  method [165]. Fig. 2.5(a) shows results on the band structure of ZB InP. In this study a modified Becke-Johnson exchange potential was used in combination with the local-density approximation [166]. As every semiconductor, ZB InP has a so-called band gap (BG) – an energy range in which no allowed states exist. The corresponding band gap energy  $E_g$  is one of the most important parameters for semiconductors and can be of direct or indirect nature. ZB InP has a direct BG with a band gap energy ranging from 1.42 to 1.34 eV for temperatures from 0 to 300 K. The two highest valence bands are degenerate at the  $\Gamma$ -point but have dissimilar curvature. Because the curvature of the approximately parabolic shape defines the so-called effective mass, they are referred to as light and heavy hole bands.

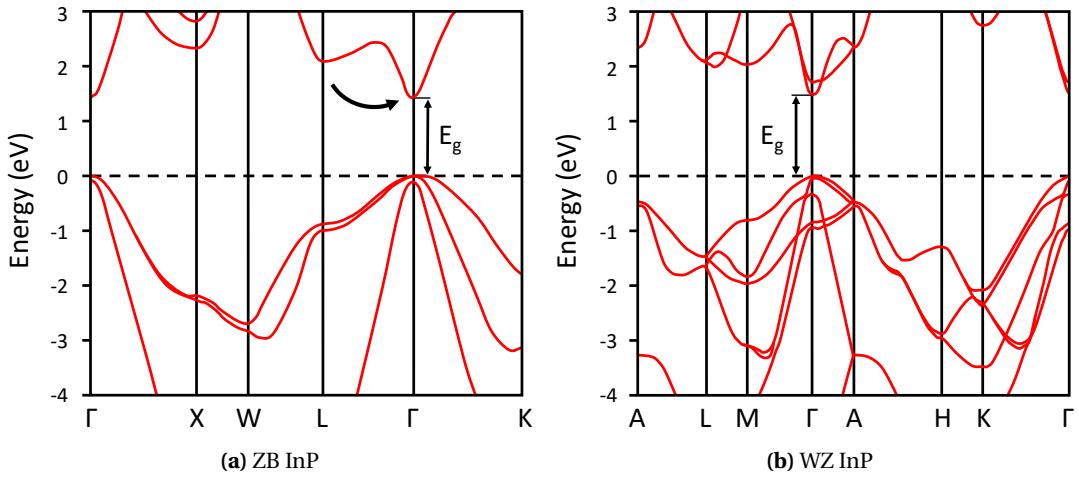


**Figure 2.5** | Electronic band structure of (a) ZB [166] and (b) WZ InP [42], represented along high symmetry directions of the Brillouin zone. The zone-folding from the  $L$  to the  $\Gamma$ -point can be seen clearly.

Up to now, group IV and III-V semiconductors are experimentally available exclusively in one of the two introduced crystal phases as bulk materials. However it is well known, mainly from theoretical predictions [48, 37, 46, 42, 30], that their physical properties change significantly when their crystal phase is changed. For example, the mechanical stability of lonsdaleite (the hexagonal polymorph of C) is considerably higher than that of conventional cubic diamond [36]. From recent band structure calculations we also know that many of their electrical and optical properties differ significantly. However unlike stable D group IV and ZB III-V compounds, which have been extensively studied over decades, the band structure (and in some cases even the mere existence [167]) of their hexagonal counterparts is still under debate in the scientific community.

One of the most comprehensive theoretical studies on both hexagonal group III-V [42] as well as group IV [30] semiconductors was carried out by Amrit De and Craig E. Pryor in 2010 and 2014, respectively. In essence, they calculate the band structure of these polytypes based on an empirical pseudopotential method with spin–orbit interactions assuming ideal WZ/LD structure. As an example, the calculated band structure of WZ InP is plotted in Fig. 2.5(b). In this study, a direct BG with  $E_g = 1.47$  eV was found [42]. Newer theoretical investigations predict 1.58 eV for the same parameter [168], whereas experimental results show values between 1.41 eV at room temperature [169] and 1.491 eV at 4 K [99]. As briefly mentioned before, due to the lower symmetry of the WZ crystal structure, heavy and light holes are split at the  $\Gamma$ -point and separated by around 63 meV [42].

To understand the relations between the ZB and WZ band structure, we can investigate how the crystal symmetries relate to each other. By describing the ZB structure in a hexagonal unit cell as it was shown in Fig. 2.2, it is possible to establish equivalences between the high symmetry points in the Brillouin zone of the two crystal symmetries. One of the most prominent features that arises from this consideration is that the  $L$ -point is zone-folded back to the  $\Gamma$ -point in WZ as can be clearly seen when comparing the two band structures in Fig. 2.5 [42]. This has important consequences. For example, that semiconductors with an  $L$ -valley conduction band minimum are expected to have a direct gap in the WZ phase. This effect is observed for example in LD Ge, as will be shown later. Another similarity that can be established from this consideration is the fact that the  $\Gamma \rightarrow L$  symmetry line in ZB corresponds to the  $\Gamma \rightarrow A$  line in WZ, as these are the  $c$ -directions of the crystal (compare Fig. 2.4).

A parameter that can not be directly deduced from the band structures (because they are normalized to the maximum valence band energy) is the valence band offset between ZB and WZ crystal phases. This parameter is especially important when investigating ZB/WZ heterostructures and characterizing their electrical transport properties. For InP, the reported band offset varies significantly between 0.11 eV [169] and 0.45 eV [170], however there seems to be a consensus that WZ InP has a higher valence band energy than its ZB counterpart. Given the larger BG of WZ InP, this results in a type II band alignment which favors the localization of electrons in ZB and holes in WZ. At least this is the case for bulk materials. Zhang et al. [171] reported that for NWs with sufficiently small diameter the band alignment changes to type I. This result points out the opportunity to create quantum wells with confinement of both carriers in the same spatial region. Other parameters that differ considerably between ZB and WZ InP are for example the effective mass [172] or the oscillator strength for the optical transition at the  $\Gamma$ -point [173]. We will address some of these dissimilarities in **Chapter 4**.

We will now look at basic properties of other group III-V and IV materials in their thermodynamically less stable hexagonal phase. As mentioned before, one of the most important parameters to consider for semiconductors is the band gap energy  $E_g$  along with the nature of the BG – direct or indirect. Fig. 2.6 shows the predicted band gap energies of hexagonal semiconductors obtained in reference [42] and [30] along with literature values of their cubic counterparts. Significant changes in the energy value can clearly be seen for a range of

materials. Most remarkably, GaP, AlP, AlAs and AlSb, all indirect in ZB phase, become direct semiconductors when their crystal phase is transformed to WZ. This has been experimentally verified for GaP [98] and for InAlP [106, 109]. As is also visible from this diagram, conventional ZB III-V semiconductors lack a direct BG as they approach the yellow-green wavelength regime. This circumstance is referred to as 'green gap' in literature [43] and prevents the fabrication of efficient green LEDs or laser diodes. WZ III-V semiconductors could present a solution to this shortcoming, however they remain difficult to synthesize. The parameters plotted on the  $x$ -axis of the diagram in Fig. 2.6, are the lattice constants  $a_{WZ}$  and  $a_{ZB}$ . The lattice constant is important to consider as it determines (along with the thermal expansion coefficient [174]) the growth compatibility of different materials. In this diagram,  $a_{WZ}$  and  $a_{ZB}$  are directly related to each other assuming ideal WZ lattice constants (Equ. 2.1). For heterostructures involving dissimilar crystal phases, one needs to take this relationship into account. For example, ZB InP is naturally compatible with WZ InP, even though the nominal lattice mismatch is around 30%. Typical hexagonal substrates such as GaN (3.19 Å [175]) or 2H SiC (3.07 Å [174]) are however still far from lattice matched to WZ III-Vs. Even InN, being the material with the

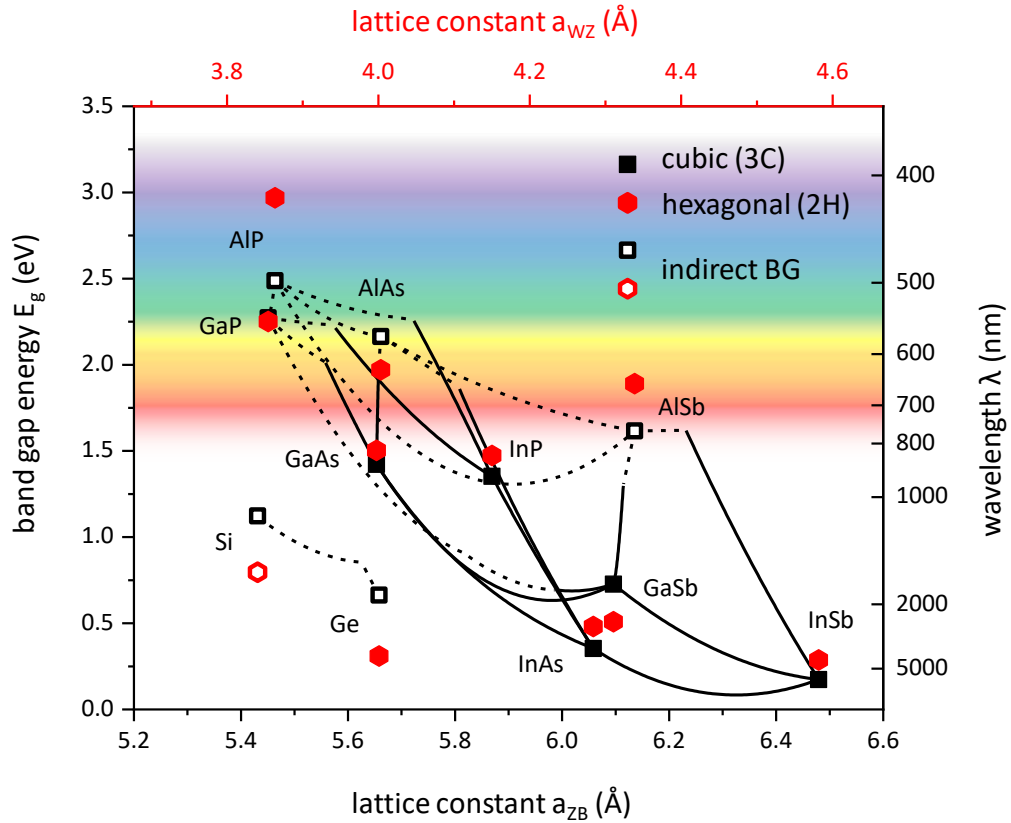


**Figure 2.6** | Band gap energy plotted against lattice constant for III-V semiconductors in ZB and WZ phase as well as Si and Ge in D and LD phase. It is indicated whether the nature of the BG is direct or indirect.  $a_{WZ}$  (top axis) and  $a_{ZB}$  (bottom axis) are related by Equ. 2.1. The right axis depicts the wavelength of a photon with the corresponding energy, and the background is colored in the appropriate color. Data taken from [42, 30].

largest unit cell among the III-Ns, has a lattice constant of only 3.5 Å [175], and therefore fails to be compatible with hexagonal GaP ( $a_{WZ}=3.85$  Å) or Si ( $a_{LD}=3.84$  Å).

Not only certain group III-V materials change the nature of their band gap, but also Ge is a direct semiconductor in its LD phase due the band folding of its conduction band minimum from the  $L$  to the  $\Gamma$  point [60]. The predicted band gap energy varies in different publications: -0.13 eV (metallic) [61], 0.23 eV [62], 0.29 eV [60], 0.31 eV [30], 0.32 eV [176], 0.48 eV [46]. In any case, such a small band gap would result in an emission in the infrared, far from telecom optical wavelength bands [177]. Fortunately, alloying with the indirect LD Si, allows for increasing the direct BG energy. Fan et. al predicted a transition at the  $\Gamma$ -point up to a composition of  $\text{Si}_{0.25}\text{Ge}_{0.75}$  with  $E_g = 0.76$  eV [46]. Newer calculations [66] even predict that LD  $\text{Si}_{1-x}\text{Ge}_x$  has a direct BG for a composition of  $x > 0.65$ , however reaching a similar energy of 0.7 eV as it is shown in Fig. 2.7. This gives great promise for group IV light emitters integrable with CMOS technology as they are desired for optical on-chip applications. However, the synthesis of LD SiGe remains extremely challenging and was so far only achieved by transferring the crystal structure from a WZ III-V NW [65, 66].

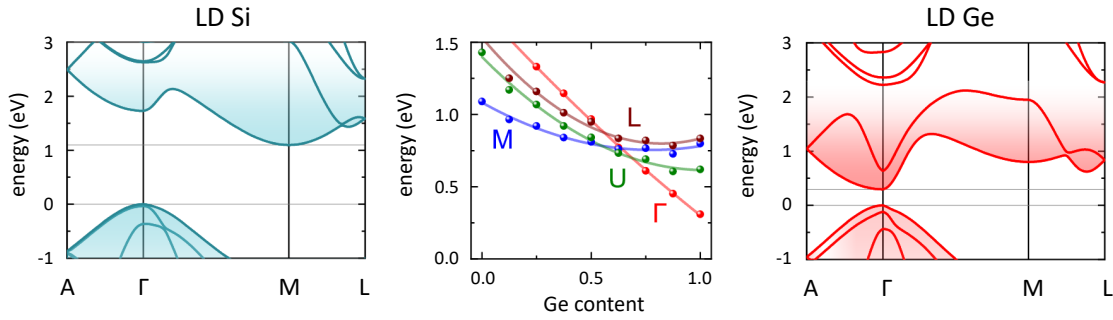


**Figure 2.7** | Electronic band structures of LD Si and Ge along with the minima at various high symmetry points for LD  $\text{Si}_{1-x}\text{Ge}_x$  as a function of Ge content. Adapted with permission from [66]

The electronic band structure of various materials and the properties that result directly from it will follow us through the course of this thesis. We will for example be able to distinguish ZB and WZ InP by looking at the photoluminescence from its direct transition at the  $\Gamma$ -point or draw conclusions on the oscillator strengths by assessing the carrier lifetime.

## 2.4 Epitaxial Growth

The synthesis of semiconductor materials with high purity and single crystalline quality is one of the main achievements that enabled the electronic revolution we have seen in the past decades and is commonly referred to as crystal growth. There are several techniques by which crystals can be grown. Large boules of Si, for example, can be pulled from a melt and are later sliced into so-called wafers that serve as basis for the majority of electronic and optoelectronic devices. Using suitable substrates, crystalline thin films can be deposited in a process called epitaxy, originating from the Greek roots epi (above) and taxis (in an ordered

manner). It is differentiated between homo- and hetero-epitaxy, for the growth of the same or another kind of material, respectively. In any case it is crucial to obtain a defined relationship between the substrate and the grown material in order to call the deposition epitaxial. Various techniques can be used such as molecular beam epitaxy (MBE), liquid phase epitaxy (LPE) or metal-organic vapor phase epitaxy (MOVPE). MBE is an ultrahigh vacuum (UHV) process in which pure source materials are evaporated in effusion cells and condensed on the growth substrate in a controlled manner. The limited scalability of MBE combined with the high costs and low throughput makes it a process that is mostly applied for research purposes rather than industrial production. In contrast, LPE is a method to grow semiconductors from the melt on solid substrates. Its low cost and simplicity makes it attractive for some commercial applications that do not require sharp interfaces or thickness uniformity [178, 179, 180].

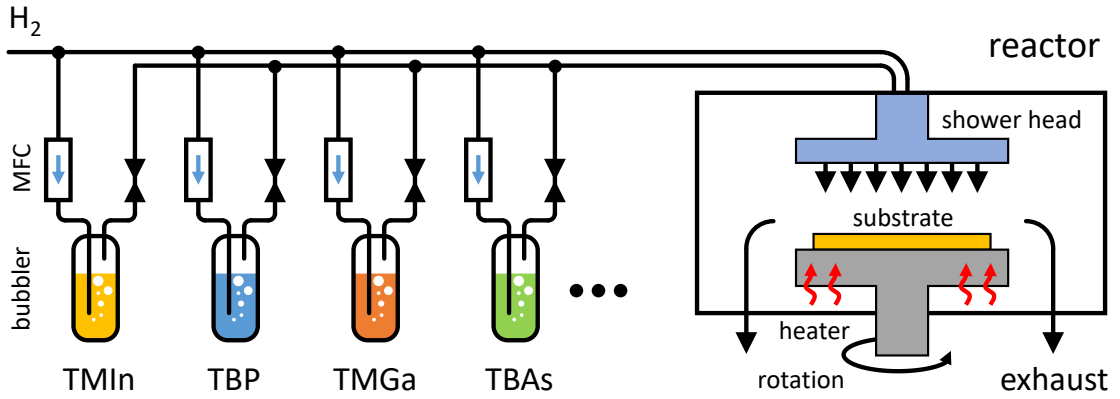


**Figure 2.8** | Schematic representation of MOVPE for III-V growth.  $H_2$  gas is bubbled through metal-organic precursor liquids and led into the growth reactor. A shower head distributes the precursor-containing gas over the substrate, which rotates at high speed. High temperature triggers the decomposition of precursor gases on the substrate surface and epitaxial growth occurs.

The technique applied in this thesis is MOVPE, for which the principle is described in Fig. 2.8. Liquid metal-organic precursors are stored in metal bottles, so-called bubblers which are kept in temperature-controlled baths. Various precursors exist to deposit materials using MOVPE. In this work, we use a reactor equipped with trimethylindium (TMIn), tertiarybutylphosphine (TBP), trimethylgallium (TMGa) and tertiarybutylarsenine (TBAs), among others. Two pipes enter the bubbler from the top, the inlet extends to the bottom of the container whereas the outlet does not enter the liquid material. To extract the precursor from the bubbler,  $H_2$  gas is injected from the inlet, bubbled through the liquid material and extracted from the outlet pipe. The amount of the metal-organic chemical that is carried by the  $H_2$  carrier gas can be quantified using the following expression [181]:

$$\Phi_M^{MO} [mmol/min] = 0.0446 \frac{p_v^{MO}(T)}{p_{bubbler} - p_v^{MO}(T)} \Phi_V^{H_2} [cm^3/min] \quad (2.4)$$

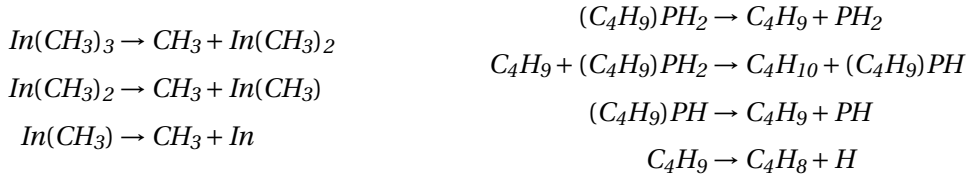
where  $\Phi_V^{H_2}$  is the volume flow of  $H_2$  through the bubbler,  $p_{bubbler}$  is the total bubbler pressure

and  $p_v^{MO}(T)$  is the vapor pressure of the metal-organic chemical.  $p_v^{MO}(T)$  can be further expressed as

$$\log(p_v^{MO}(T)) = A - \frac{B}{T} \quad (2.5)$$

where  $A$  and  $B$  are empirical values specific for each chemical and  $T$  is the bubbler temperature. While  $T$  and  $p_{bubbler}$  are usually kept constant, the amount of precursor material is determined by adjusting the flow  $\Phi_V^{H_2}$  individually for each bubbler. This can be done by using a mass flow controller (MFC) at the input line as depicted in Fig. 2.8. The outlets of all bubblers are connected before they are guided to the growth reactor where they are further diluted with  $H_2$  gas. A shower head provides for equal flow conditions on the substrate, which is mounted on a so-called susceptor. The susceptor is rotated at high speed ( $\sim 1000$  rpm) and heated up to temperatures of  $\sim 750$  °C. The reacted and remaining unreacted gases leave the chamber through an exhaust line which leads into a chemical scrubber. The reactor pressure is typically kept comparably close to ambient pressure (e.g. the Veeco P-125 system used in this thesis is operated at 80 mbar). The second important parameter during growth (besides the molar flow of the precursor materials) is the temperature of the substrate, which can be monitored by pyrometers that are mounted next to the shower head.

Group III and V atoms are released from the precursor gases through thermal decomposition in the MOVPE. This so-called cracking process can happen homogeneously in the vapor phase or heterogeneously on the substrate surface. The latter is typically preferred during epitaxy [182]. In the case of InP growth, the cracking reaction for TMIn and TBP can follow the following steps [183, 184]:



$\text{PH}$  is then believed to decompose heterogeneously on the surface to  $\text{P}_2$  and  $\text{H}_2$  [184]. The details of the reaction steps are however controversially discussed in literature [185, 186, 187]. Taking into account multiple precursors and heterogeneous surface reactions, these processes can become even more complex, various decomposition mechanism can run in parallel, influence each other or depend heavily on the growth temperature [188, 189]. In general, MOVPE is a highly complex process and as a result many growth studies are carried out largely empirically, giving crystal growth the appearance of an art [190]. Not all aspects of the growth process are thoroughly understood, however models exist which are able to predict the performance of MOVPE in dependence of certain growth parameters. For example, various growth regimes can be distinguished. At low temperature, the precursor gases do not

react entirely and the process is limited by reaction kinetics. In this regime, the growth rate is dependent on temperature, but also for example on the orientation of the substrate. At higher  $T$ , the growth rate is determined by mass-transport because precursor gases decompose efficiently and completely on the surface. This is the regime where MOVPE reactors are typically operated.

The growth temperature however does not only determine the decomposition efficiency, but also for example the surface diffusion length of adatoms of the different growth species before they incorporate into the crystal. It is important to consider these effects, especially for selective growth techniques which will be discussed later. Other parameters include the absolute and relative partial pressures of the precursor materials, which is often referred to as V/III ratio. These parameters will play a significant role on the quality of the grown crystal. Understanding and controlling them will thus be vital for this work.

Besides the reactor conditions, the quality and type of the substrate material will determine the outcome of a growth experiment. Not only the orientation, which is typically a high symmetry plane such as (001) or (111) or a defined angular miscut from such a plane, but also surface roughness, oxide formation or other contaminations will influence the quality and morphology of the grown crystal. Further, different crystal structures such as D and ZB, even though highly similar, show discrepancies in their symmetry. Because III-V compounds are binary, their mirror symmetry is broken along the {111} directions and two discriminative {111} directions with opposite polarity exist. We refer to the two polarities as A- or B-type depending on whether the surface termination is by group III or group V atoms, respectively [191, 192]. This has important consequences for the hetero-epitaxy of polar on non-polar materials, because they can nucleate with two different orientations [193]. As shown in Fig. 2.9(a), such an epitaxy can result in APBs, where atoms of the same type are connected to each other.

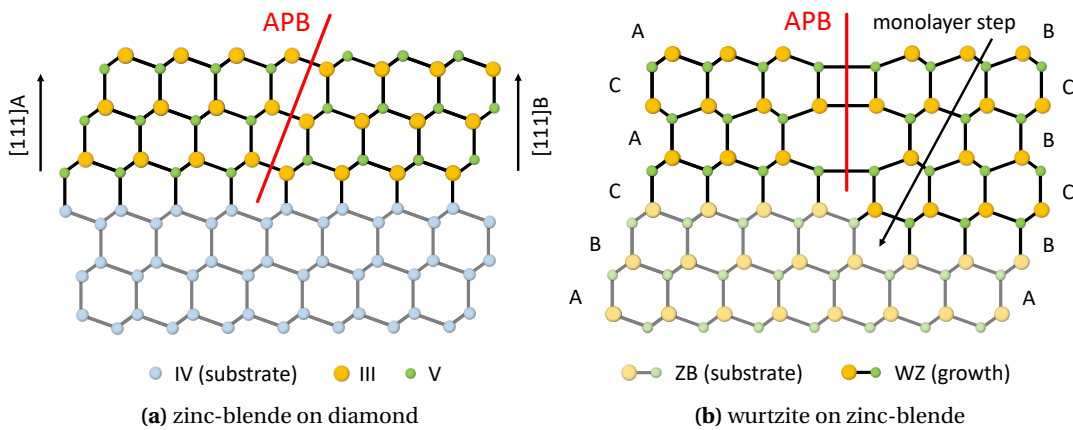


**Figure 2.9** | Antiphase boundary formation for crystal structure mismatched epitaxy. (a) Two ZB nuclei with opposite polarity merge on a non-polar D substrate. (b) WZ films that nucleate on a ZB substrate with monolayer steps follow different stacking sequences (e.g. CACA... vs. BCBC...). At the interface APBs can be created as a result.

Similar defects are expected when WZ material is grown on a ZB substrate with monolayer steps as depicted in Fig. 2.9(b) [194]. In any case, APBs should be avoided as they are electrically charged and therefore have high impact on device performance. We will address the formation of APBs in WZ InP and how it limits the size of the obtained films in **Chapter 5**.

### 2.5 Selective Growth of Nanostructures

MOVPE and MBE have been extensively used for the deposition of semiconductors in planar layers and thin films. More recently, these techniques were adapted to grow nanostructures with more complex morphology such as NWs [63] or related geometries [108]. An advantage of these elongated crystals with typically less than 100 nm diameter is the possibility to grow complex heterostructures, because lattice mismatch is much less critical than for layer growth. This also enables the synthesis of materials with high crystalline quality for which otherwise no suitable substrates exist. It is therefore not surprising that metastable wurtzite crystal phases in III-Vs were first observed in NWs, and for many materials NW growth remains the only way of synthesizing them in high quality. As a result, the formation of metastable crystal phases is mainly understood by considering the peculiarities of NW growth and the importance of surface energies in low-dimensional structures. Understanding the growth mechanisms of NWs is therefore crucial for carrying out this research project and we will discuss the fundamentals here.

The transition from planar to NW epitaxy is possible by restricting the deposition to only specific areas of the substrate. This can be facilitated either by the use of catalyst particles or by patterning a mask such that only defined areas of the crystalline substrate are exposed. The first technique was introduced by Wagner and Ellis in 1964 and is commonly referred to as vapor liquid solid method [63]. It is the more versatile technique and it allows for the growth of a large range of materials with high control over the crystalline phase [195]. As depicted in Fig. 2.10, a catalyst material (usually Au) is deposited on a crystalline substrate prior growth. After heating up and exposing the sample to the growth species in either an

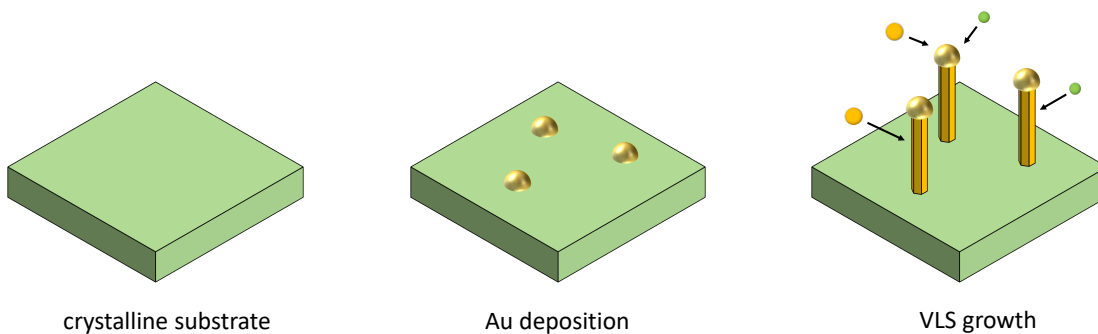


**Figure 2.10 |** VLS growth mechanism. A catalyst (e.g. Au) is deposited on a crystalline substrate and forms a liquid alloy with the growth species under growth conditions. Supersaturation in the droplet causes precipitation at the droplet-substrate interface and an elongated crystal is grown.

MOVPE or MBE reactor, an alloy is formed which remains liquid during the epitaxy process. Continuous supply of the precursor gases causes supersaturation conditions in the catalytic droplet and the growth species precipitate at the droplet-substrate interface as a solid crystal. Layer-by-layer an elongated crystal is formed, typically along a  $\langle 111 \rangle$ -direction. Whereas the diameter is defined by the size of the droplet, the length can be controlled by the growth time. The fact that this deposition is based on a material transition from a vapor to a liquid into a solid crystal gives this technique its name – VLS.

While VLS is a versatile technique that allows for the growth of many different materials, heterostructures and doping, it cannot be excluded that parts of the catalyst metal is incorporated into the crystal. This can be detrimental for the optoelectronic properties, especially in the case of Au, because it is known to create deep band gap levels in many materials. This can be avoided with the so-called self-catalyzed VLS method, where one of the growth species acts as the catalyst material. Self-catalyzed VLS has been applied e.g. for the growth of GaAs [196] and GaSb [197] NWs using Ga as a catalyst or InAs [81] and InSb [121] NWs using In. In any case, the absence of a third element has a destabilizing effect, and growing NWs with controlled and uniform diameter remains challenging [198, 199].

Another technique that does not make use of a catalytic particle of any kind is the so-called vapor-solid (VS) growth. Rather than defining the growth area by a liquid-solid interface, crystals can be shaped by making use of the high growth rate anisotropy of the various crystalline facets [200]. For example, under certain conditions efficient growth can be achieved along

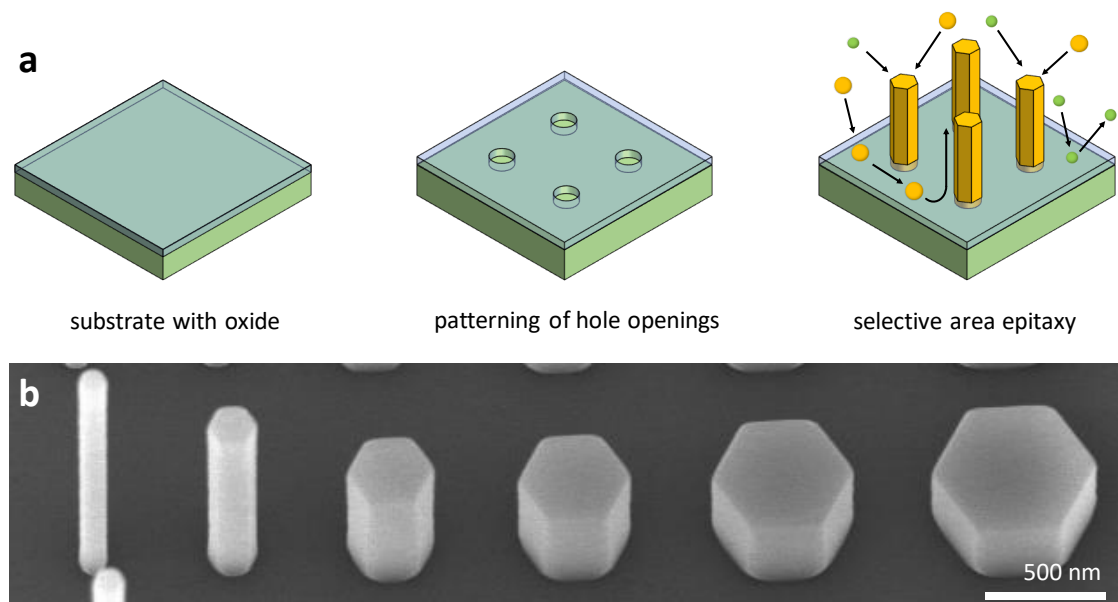


**Figure 2.11** | Selective area epitaxy of NWs. (a) Hole openings are patterned into a selective mask material by lithography and etching. Anisotropic growth conditions using MOVPE allow for the epitaxy of NWs with high aspect-ratio. (b) Tilted SEM image of GaAs NWs grown on Si(111) masked with SiO<sub>2</sub>. Surface diffusion effects cause thinner wires to grow taller.

either the (111)A or (111)B direction while other low-index surfaces such as {110} exhibit a deposition rate close to 0. Thus, a combination of the VS technique with a selective mask allows for the growth of NWs [201]. A schematic of this so-called selective area growth (SAG) or selective area epitaxy (SAE) is depicted in Fig. 2.11(a). Selective masks are typically made from  $\text{SiO}_2$  or  $\text{Si}_3\text{N}_4$  and patterned using top-down lithography techniques, which comprises the advantage of exact positioning. The growth conditions must be well chosen, both, to suppress the nucleation on the mask as well as to obtain facet selective growth along a particular direction. This results typically in less versatility than VLS growth, and considerably less control of the crystalline phase, leading to the formation of polytypic material with large amounts of PDs [202, 118, 203]. Nevertheless, position-controlled NWs have been achieved in a wide range of III-V semiconductors using SAE, including GaAs [204], InP [205], GaP [206], InAs [207], InGaAs [120] as well as nitrides [208] and oxides [209]. The direct incorporation of the growth species from the vapor phase into the crystal further allows for axial heterostructures with comparably sharp interfaces, as it has been shown e.g. for InGaAs/GaAs [210], AlGaAs/GaAs [211] or InAsP/InP [212].

An important parameter during selective epitaxy is the diffusion length of the adsorbed growth species on the various surfaces during the deposition process. It is defined as the average length an adatom can travel on a surface before it is desorbed or incorporated into the crystal. As the cross-section of NWs and thus the effective collection area for directly adsorbed material from the vapor is very small, SAE typically relies on the material supply from the substrate through surface diffusion on both the selective mask as well as the NW sidewalls [201, 213]. Effects resulting from this circumstance are often referred to as "loading effect" [214, 215, 216, 217, 218]. For example, thinner NWs tend to grow higher than thicker ones as they collect approximately the same amount of material in a given time span (Fig. 2.11(b)). The increased relative amount of group III material diffusion from the substrate to NWs with smaller diameter can also result in droplet formation and subsequent VLS growth. It has been demonstrated that SAE and VLS can occur simultaneously by varying the diameter of the mask openings [219]. Another effect is that NWs can compete with each other for adatoms when their collection area is overlapping [220].

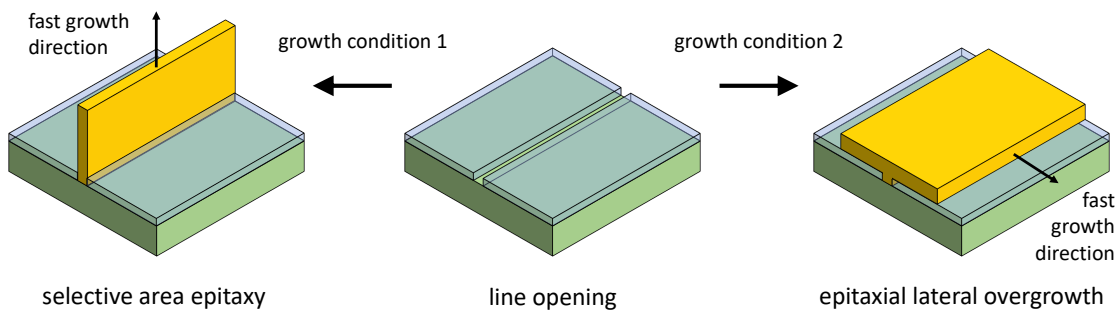


**Figure 2.12** | Depending on growth conditions and choice of opening orientation a line opening can either be used for the epitaxy of fins (SAE) or planar layers (ELO).

As opposed to VLS, SAE offers an additional advantage: Because the openings from which growth is initiated are lithographically designed, they are not restricted to simple circular holes but can be extended to virtually any shape. Taken into account growth rates for low-energy facets during epitaxy, it is possible to synthesize for example vertical membrane- prism or ring-like structures [108, 221, 222, 223]. Fin growth can be initiated from line openings oriented along specific crystalline directions as depicted on the left hand side of Fig. 2.12. Compared to NWs, such an epitaxy offers the advantage of large-area planes favorable for building electronic or optoelectronic devices [221].

For conventional device processing, however, it is even more desirable to grow planar films, preferably on insulator. This can be achieved by a technique called epitaxial lateral overgrowth (ELO). The principle is illustrated on the right hand side of Fig. 2.12. Rather than selecting the growth conditions and opening orientation such that epitaxy primarily follows vertical directions as it is typically done for SAE, a high lateral growth rate is intentionally chosen in order to obtain thin layers. This technique was initially developed using LPE for defect filtering of defective substrates or buffer layers [225, 226, 227, 228, 229]. Indeed, the dislocation density in films obtained by ELO can be reduced by orders of magnitude compared to the substrate

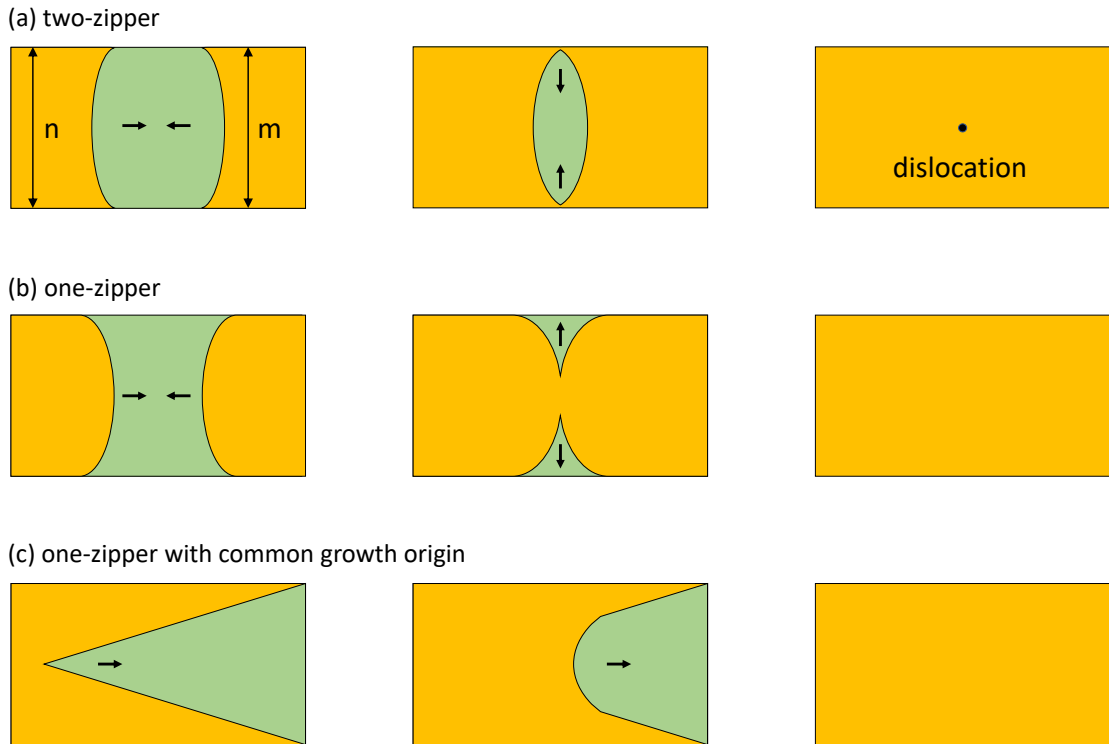


**Figure 2.13** | Top-view schematic of zipper growth modes. (a) Two-zipper growth mode, when the coalescence starts from two points. Arrows indicate the directions of lateral growth,  $n$  and  $m$  denote the number of lattice points between the two connecting points. (b) One-zipper mode, when coalescence starts from one point. No dislocations are expected in this case. (c) Realization of one-zipper growth mode with common growth origin. Adapted from [224].

material [200]. ELO from narrow line openings is also given the name microchannel epitaxy (MCE) in literature [230, 231, 232, 233, 234]. As for SAE, typically very limited growth conditions can be applied in order to achieve desired film morphologies. To obtain wide layers from ELO or MCE, structures grown from neighboring line openings are typically combined and merged into a single layer [235]. However, the area where two adjacent crystals coalesce generally contains newly nucleated dislocations that are detrimental for the material properties [236]. To suppress the nucleation of dislocations in coalesced layers, a new method was investigated by Yan et al. in 2000 [224]. In this study, the authors could identify two different growth modes when layers are merged from either two or one zipper points, as indicated in Fig. 2.13(a) and (b), respectively. In the first case, due to imperfections of the substrate and grown layers, the number of lattice points  $n$  and  $m$  between the two connection points can be unequal, in which case at least one dislocation is generated upon merging. In contrast, such a defect is likely not to be formed when the growth follows a one-zipper mode as sketched in Fig. 2.13(b). To realize the latter case, typically non-parallel seed lines are patterned and overlayed such that the layers have a common growth origin from the substrate [237, 238, 239]. This case is illustrated in Fig. 2.13(c). Not only defect formation can be suppressed by using a one-zipper growth mode, but also the lateral overgrowth from facets with otherwise negligible growth rate can be triggered by inducing a zipper point. We will use this effect combined with lateral crystal phase transfer in order to extend metastable fins into layers as detailed in **Chapter 5**.

Another technique for the selective growth of layers has been referred to as tunnel epitaxy [240, 241, 242], confined lateral selective epitaxial growth [243, 244, 245] or conformal vapor phase epitaxy [246] in literature. Originally developed for the synthesis of silicon-on-insulator (SOI) substrates, it has later been applied for the growth of lateral SiGe heterojunctions [247], III-Vs [248] and their integration on Si substrates [249, 250, 251]. We will refer to this technique simply as conformal epitaxy (CE) and it is in Fig. 2.14. The main difference to SAE is the additional capping oxide that confines the growth to a certain shape, typically a planar layer. The morphology of the grown crystal is primarily defined by the confinement of this so-called template, which comprises several advantages. For example a larger range of growth parameters is accessible, because the morphology of the crystal will be determined by the shape of the lithographically designed template oxide. Lateral heterostructures or doping can

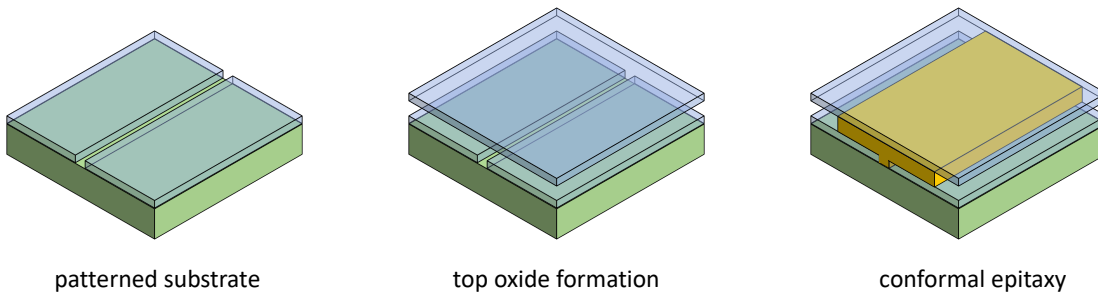


**Figure 2.14** | Conformal epitaxy of layers. Line openings are patterned into a selective mask material by lithography and etching after which a top oxide is deposited by the use of a sacrificial material. The templates are filled subsequently by MOVPE.

be achieved, because there is no overgrowth in vertical direction as compared to ELO. Newer studies report on the growth from small Si seed areas and are referred to as confined epitaxial lateral overgrowth (CELO) [252] or template-assisted selective epitaxy (TASE) [253, 254, 255]. The latter has been extensively used to fabricate both horizontal and vertical electronic and optoelectronic devices [256, 257, 258, 259, 260] as well as to study growth mechanisms [261], facet-selective group-III incorporation [262] and formation of twin-free NWs [263]. In this thesis, CE was one of the techniques applied in order to synthesize metastable wurtzite III-V materials as will be detailed in **Chapter 4**.

## 2.6 Polytypism in III-V Semiconductors

In bulk form and under ambient conditions, III-V semiconductors are stable in only one crystalline phase. For nitrides (AlN, GaN, InN) the stable phase is WZ, whereas for conventional III-Vs, ZB is the thermodynamically preferred crystal structure. In NWs it can be observed that materials with stable ZB phase can also crystallize in a metastable WZ configuration under certain conditions [264, 265, 77, 266]. This property is referred to as polytypism. As detailed before, polytypism can be an interesting opportunity to synthesize material phases with more favorable properties, for example to obtain direct band gap in the green wavelength regime or in group IV materials. Here, we will address the fundamentals of polytypism found in III-Vs and offer explanations for their occurrence especially in NWs. Later, we will make use of this knowledge in order to synthesize metastable crystal phases in the form of layers by the usage of ELO and CE.

In order to understand the preference for certain materials to crystallize in one phase or the other, we will first recall the two predominant crystal structures in semiconductors and what differentiates them from an energetic perspective. As mentioned before, ZB and WZ are equivalent up to the first nearest neighbor bonds, which are characterized by a tetrahedral configuration. The main structural difference starts to appear only in atoms at a further distance, which generally causes the two crystal phases to be energetically very similar. Fig. 2.15 depicts two neighboring bonding tetrahedra for ZB and WZ phases. In the first case, the adjacent bilayers are twisted by  $60^\circ$  with respect to the first layer, whereas for WZ the ions of opposite

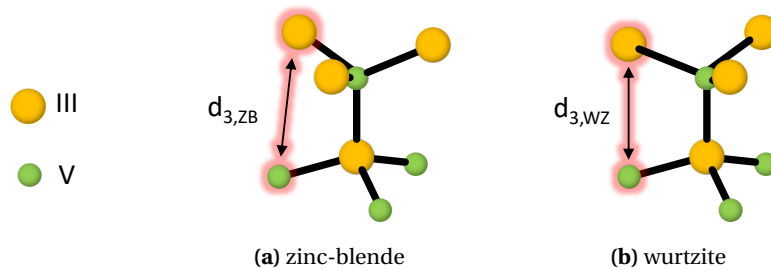


**Figure 2.15** | Local bonding configuration in (a) ZB and (b) WZ structures. The third nearest neighbor bond length is shorter in WZ.

sign are stacked exactly on top of each other [168]. This effectively reduces the distance of the third nearest neighbors for WZ with respect to the ZB phase.

To determine whether materials will favor shorter or longer bonding distances between their third nearest neighbors, we have to consider the atomic forces that are involved in the bond. There are two competing mechanisms to take into account: (1) The electrostatic repulsion of the electron clouds favoring longer and (2) the Coulomb interaction between cation and anion favoring shorter bond distance [78]. Hence, elemental group IV semiconductors with no Coulomb interaction, generally crystallize in the cubic ZB symmetry. Whether or not the attraction between ions of opposite sign in III-V materials will be dominant is mostly determined by the so-called ionicity. The ionicity is a measure for the strength of the ionic forces in an otherwise covalent bond and is largely defined by the difference of electronegativity of the respective atoms. Pauling proposed the following expression to determine the ionic character of a bond [267]

$$f_i = 1 - e^{\frac{-(X_A - X_B)^2}{4}} \quad (2.6)$$

where  $f_i$  is the ionicity and  $X_A - X_B$  is the difference in electronegativity. Using this expression, the ionicity of III-V compounds can be calculated as plotted on the x-axis of Fig 2.16 [264]. III-nitrides show a highly ionic character, which explains their preference to crystallize in WZ phase [72]. III-antimonides are on the other side of the spectrum, which according to this model makes them very stable in the ZB crystal structure [123]. In-between remain the arsenides and phosphides with intermediate ionicity and resulting tendency for polytypism when grown in NW form [76, 268, 269, 270]. Using ab-initio techniques, the bulk energy difference

$$\Delta E_{WZ-ZB} = E_{WZ} - E_{ZB} \quad (2.7)$$

between the ZB and WZ crystal structure can be calculated [29]. This value is plotted on the

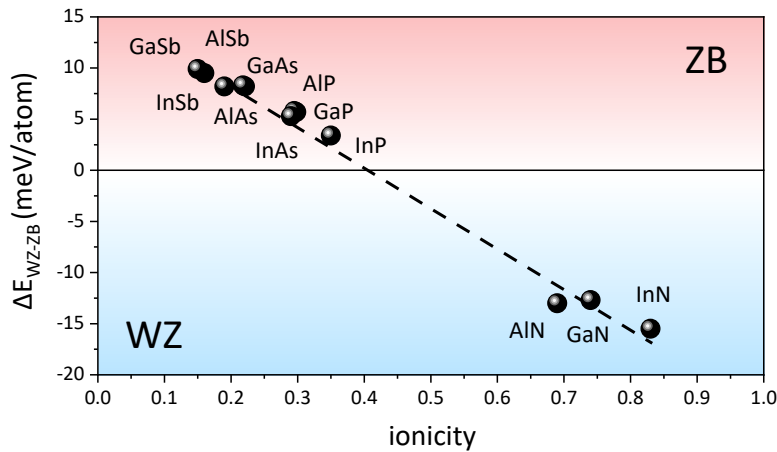


**Figure 2.16** | Bulk energy difference between the ZB and WZ crystal structure in dependence of ionicity for various III-V compounds. A clear correlation can be observed. Data from [264].

y-axis in Fig 2.16. A clear negative correlation confirms the importance of the ionicity for determining the preferred crystalline phase. Similar calculations can be applied to calculate the tendency of cubic III-V compounds to form stacking faults [271] or more complex stacking arrangements such as 4H or 6H [168].

While the ionicity explains the thermodynamically stable phase for bulk materials, in nanostructures another parameter plays a critical role: the surface energy [265]. As the surface to volume ratio increases for decreasing diameter in NWs, this parameter is especially important to consider for thin NWs. A commonly used measure for the surface energy is the density of dangling bonds at the respective interface. Considering the low-index surfaces perpendicular to the typical growth direction, a varying number of dangling bonds is obtained as depicted in Fig. 2.17. This model explains the facet formation in typical ZB and WZ NWs very well [272]. Even more important however is that the lowest surface energy is obtained only in WZ phase when the crystal is enclosed in  $\{1\bar{1}00\}$ -facets. Thus, as the importance of surface energies is increasing, WZ formation should be favored over ZB to minimize the total energy of the crystal.

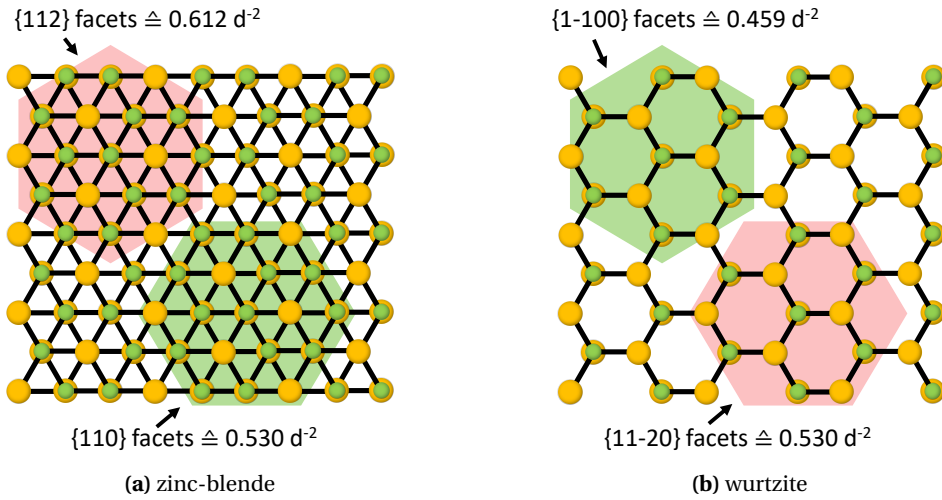


**Figure 2.17** | (a) ZB and (b) WZ crystals viewed along the typical growth direction (c-axis). Each symmetry allows for the formation of 2 types of low-index sidewall facets perpendicular to the NW axis (considering straight NWs). For each facet-type the density of dangling bonds is indicated. Green-shaded hexagons indicate the energetically preferred facet-formation for the respective crystal structure. The overall lowest surface energy is obtained for WZ  $\{1\bar{1}00\}$ -facets. After [268].

Indeed, theoretical calculations predict a strong diameter dependence of the thermodynamically preferred crystal phase of NWs [273]. If the diameter is sufficiently decreased, any III-V material will adopt the WZ phase as the surface energies dominate the system. Increasing the dimensions will lower the surface to volume ratio and before-mentioned ionicity will determine the crystalline phase. The critical diameter for which a ZB-WZ cross-over is expected is strongly dependent on the material and in the range of 12-32 nm for conventional III-V compounds [264]. The energetic similarity between ZB and WZ crystals during NW growth makes

them prone to unintentional phase intermixing and stacking faults, which is detrimental to the performance of electronic and optoelectronic devices [274]. Recently, the understanding of the formation of ZB and WZ crystal structures has improved significantly, which enabled for example crystal phase controlled VLS growth of InP [99], GaP [76], InAs [112] and GaAs [75] NWs. For self-catalyzed VLS or SAE it remains more challenging to prevent polytypism and only few studies exist reporting phase-pure NW synthesis [121, 196, 266]. Addressing the growth of metastable materials will be the scope of the following section.

### 2.7 Synthesis of Metastable Semiconductors

The synthesis of metastable semiconductors is a major challenge in material science with the promise to create a new kind of matter with superior properties. So far, most authors considered NW growth as the primary route for achieving exactly that. This thesis is dedicated to extend existing theories and routes for WZ III-V epitaxy and apply them to the growth of layers and thin films, which are more applicable to device fabrication using existing processing techniques. In this section, the state of the art of metastable NW synthesis will be summarized as a basis for new ideas developed in the framework of this research project.

Many aspects of polytypism in III-V NWs can be understood in terms of ionicity and surface energies as laid out in the previous section. However, by considering only the energetics of fully formed crystals rather than the growth kinetics as they occur in VLS and other techniques, it is impossible to fully explain all experimental observations. For example the before-mentioned predicted critical diameter is far too small compared to the occurrence of pure WZ GaAs NWs with diameters as large as 100 nm [111]. The dependence of the crystal phase on the growth parameters such as V/III ratio or temperature is an additional indicator for the importance of the growth kinetics. Tuning just the group V flux during epitaxy can for example change the phase completely from ZB to WZ in a range of materials [79]. It has further been reported that the addition of dopants can considerably influence the crystal structure. Doping with Zn is known to promote ZB formation in InP NWs [275] in contrast to S, which has the tendency to create WZ material [276]. Likewise, a high Se doping level turns InAs NWs into defect-free ZB [277]. These examples are meant to give an idea of the diverse phenomena that are experimentally observed for NW growth. Many of them are still not understood completely. In particular, it is beyond the scope of this work to explain all these phenomena in a comprehensive way, but rather introduce certain concepts that are necessary to understand experimental observations made during this research project.

Newer models consider nucleation mechanisms to describe the occurrence of metastable phases [278, 279, 68, 280, 71]. They take into account that once a nucleus of critical size is formed it will spread out laterally over the entire interface, without creating any defect. Hence, the orientation of this first nucleus will determine whether the layer is stacked in ZB or WZ type, rather than the energetics of the full crystal. At least, this is true for sufficiently small growth facets, where a nucleation event is unlikely enough for not two independent events

to happen before the layer is filled [281]. We will argue that the occurrence of the second case limits the size of WZ InP films that are grown in vertical direction in **Chapter 5**, but we will first discuss the case of single nucleation events and subsequent layer-by-layer filling. As mentioned, the nucleus orientation of each layer determines the crystal phase of the resulting material. In order to understand metastable WZ NWs we thus need to search for the reason for preferential WZ nuclei formation during their growth.

Notably, a comprehensive model to explain WZ III-V NWs during VLS growth was developed by Glas et al. in 2007 [70]. It is built around the observation that the droplet supersaturation (with Ga in this case) significantly impacts the resulting crystal phase. High supersaturation promotes both smaller critical nucleus size as well as the formation of WZ phase, which is reminiscent of the critical NW diameter criterion as discussed above. Instead however it is argued that nucleation preferentially takes place at the so-called triple phase line (TPL), that is, the interface between the vapor, liquid and solid phases involved during VLS growth (Fig. 2.18). The reasons can be explained by changes in the interface energies at different nuclei positions, but have been previously argued simply with the low solubility of group V materials in Au and the resulting low nucleation probability in the center [282]. It is subsequently argued that at the TPL, WZ nucleation is preferred at high supersaturation for minimizing the total surface energy, which is lowest in vertical  $\{1\bar{1}00\}$  type facets. Even though there is no TPL involved in VS growth, we will use a similar argument to explain WZ nucleation during InP SAE.

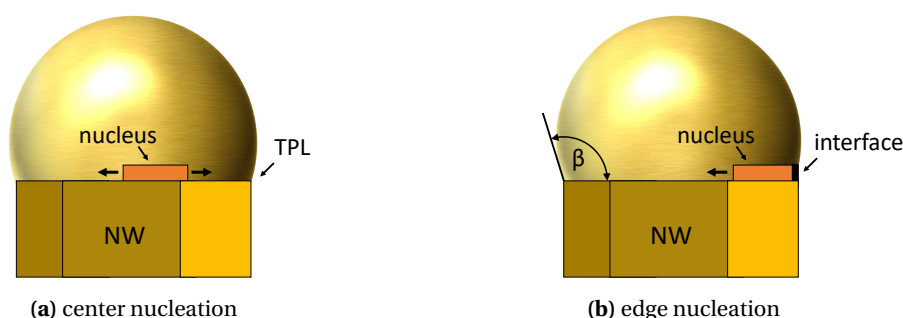


**Figure 2.18** | Side-view of a catalyst droplet on top of a NW, showing two different ways of new nuclei to be formed. (a) Nucleation event in the center. (b) Nucleation at the edge of the NW, the so-called triple phase line.

By far not all experimental observations can be understood by just considering the supersaturation of the droplet. Hence, to explain the wide range of phenomena that are observed in particular upon changing certain growth parameters, various models exist. It is for example known that surface reconstructions of crystals, and thus the surface energies, can be considerably altered by both temperature and V/III ratio [283, 284, 285]. As this will change the energetic balance during growth, it can have an influence on the preference over ZB or WZ stacking [286, 79]. Further, the shape of the droplet and in particular the contact angle at the NW interface seems to have an important impact on the growth kinetics and the facet formation (see Fig. 2.18(b)) [287, 279, 288, 289]. Interestingly, in order to explain ZB formation at higher supersaturation, some authors argue that in this case nucleation at the center takes

place which preferentially is ZB type [76, 290, 67].

As the crystal phase can be transformed primarily along the stacking axis of the crystal, it is further important to consider the crystalline directions during growth. NWs typically grow along a  $\langle 111 \rangle$ -direction which becomes  $\langle 0001 \rangle$  upon phase change to WZ. They are thus prone to stacking fault formation and phase mixing. In order to achieve phase purity, every single layer must nucleate at the correct position. Because WZ has only one stacking axis, all other directions and in particular those perpendicular to it, will have the tendency to transfer the crystal phase in order not to introduce energetically unfavorable defects. This can be useful to stabilize a crystal phase as it is sketched in Fig. 2.19. The  $\langle 1\bar{1}00 \rangle$ -directions will typically maintain the stacking order, even during hetero-epitaxy. This principle has been successfully applied to synthesize materials such as GaP [100], InAs [114], AlGaAs [115], InGaAs [117, 291, 292], AlInP [103] and AlGaP [102] in WZ phase. Even more interesting is to use this technique to grow LD group IV materials such as Si [141], Ge [66] and SiGe [65]. Such an example is given in Fig. 2.19(c).

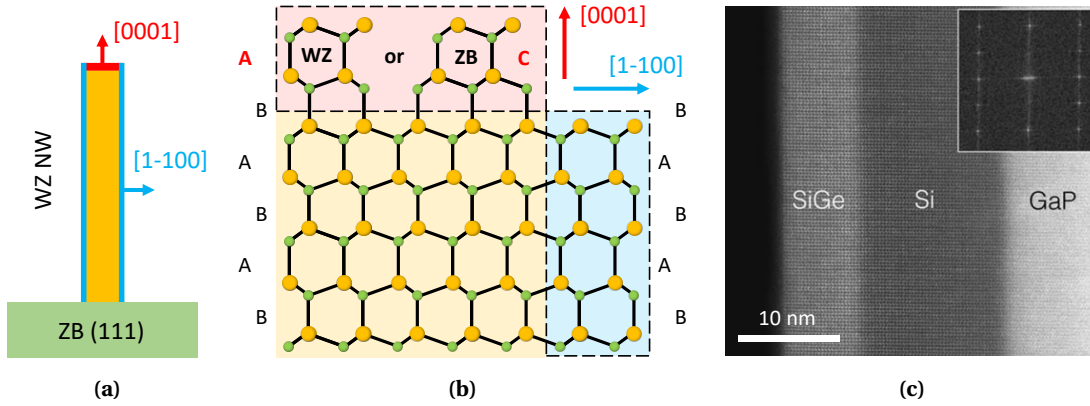


**Figure 2.19** | Principle of crystal orientations, phase change and stacking transfer. (a) Typical vertical WZ NW grown along  $[0001]$ -direction. (b) Phase change is possible along  $[0001]$ -direction, but perpendicular to it stacking is typically transferred. (c) Crystal structure transfer applied to LD Si and SiGe from a VLS grown WZ GaP NW. Adapted with permission from [65].

Most of the previously cited models are specific to catalyzed growth. However, it is not straightforward to envision a route for layer epitaxy with VLS. Instead we want to make use of selective growth methods which have been introduced before. Much less is known about the formation of metastable materials for these techniques. In particular, to the best of my knowledge, experimental proof of metastable catalyst-free III-V compounds was only obtained for InP [105, 293] and related ternaries such as InGaP [107] and InAlP [106] for In-rich alloys. As indicated in Fig 2.16, these are also the materials with highest ionicity and lowest energy difference between ZB and WZ phase. The mechanisms involved in the growth are still not fully understood. A qualitative model was introduced by Kitauchi et al. in 2010 [268]. Their theory takes the termination of the (111)A facet in InP into account, and explains how under certain conditions WZ stacking might be favored. This model is purely based on thermodynamics and does not include any growth kinetics. In particular, it can not explain the  $WZ \rightarrow ZB$  transition,

which they observe for large NW diameter, as the top facet is considered as a surface with infinite dimensions.

In contrast, we suggest that even during pure VS growth, nucleation close to the edge is favored, as the number of dangling bonds is expected to be higher in this region. By tuning the growth conditions such that the nucleation rate at the surface becomes sufficiently low, edge nucleation will become the dominant mechanism. Following the same arguments as proposed in previous models, such a nucleus will prefer WZ stacking orientation in order to minimize its vertical surface energy. As the NW diameter increases, the probability of nuclei forming at the surface rather than at the edge rises and mixed crystal phase is obtained. However as has been discussed earlier, with SAE it is not only possible to grow structures having approximately circular cross-section, but virtually any shape. Following the low-index  $\langle 1\bar{1}00 \rangle$ -directions, lines can be patterned from which stable fins can be grown. In such a structure, the surface to edge ratio is approximately the same as in NWs of equal diameter. Hence, WZ growth can be expected. Indeed, WZ InP fins were successfully synthesized recently [108]. An SEM image of WZ InP synthesized during this research project along with an atomistic model are depicted in Fig. 2.20(a). Phase change is obtained in vertical direction close to the nucleation interface.

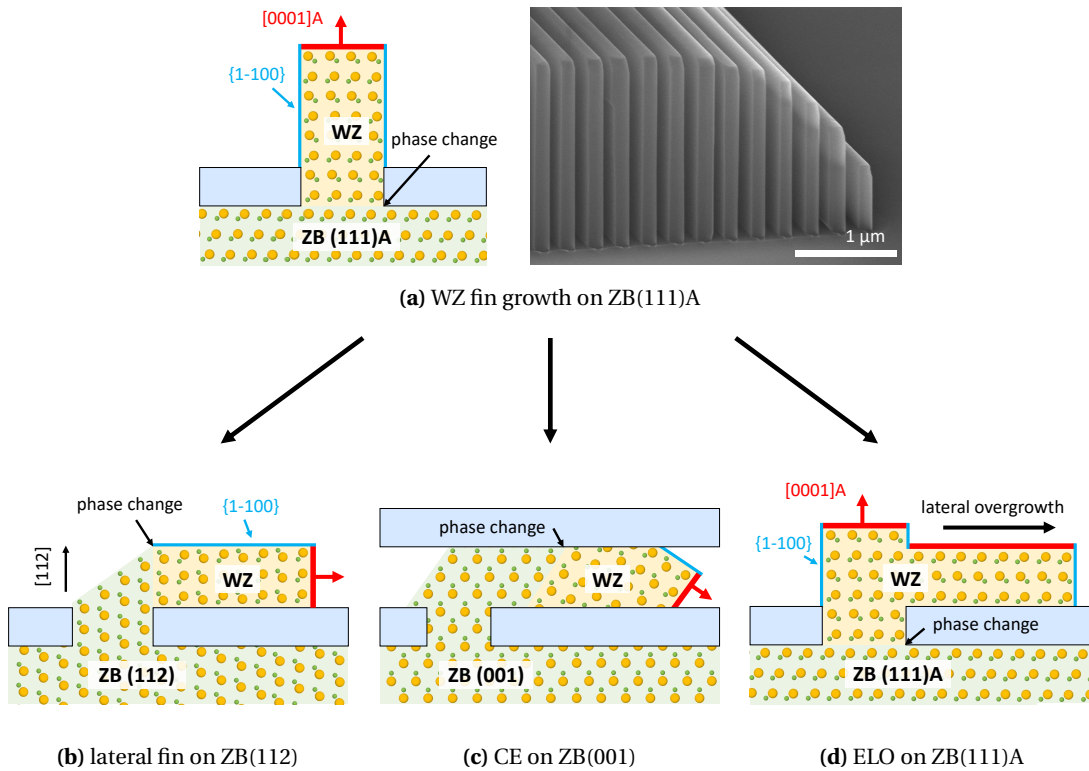


**Figure 2.20** | Concepts for epitaxy of WZ fins and planar layers. (a) Schematic and SEM image of WZ InP fins grown on ZB(111)A substrates. (b) Concept for lateral fin growth on ZB(112). (c) Concept using conformal epitaxy for growth on standard ZB(001) substrates. (d) Epitaxial lateral overgrowth can be used to expand fins into layers by transferring the stacking order. Fast growth (0001)A planes are indicated in red.  $\{1\bar{1}00\}$  facets with low growth rate are indicated in blue.

Growth conditions need to be carefully chosen, such that both WZ phase is achieved as well as high growth rate selectivity between the (0001)A facet and the side-wall  $\{1\bar{1}00\}$  facets.

Fins allow for large surfaces that can be useful for both advanced material characterization as well as for the creation of electronic and optoelectronic devices. However, even more desirable would be the growth of planar films. Based on epitaxy of WZ fins, we envision 3 distinct concepts of synthesizing planar layers by carefully choosing substrate orientation and applying previously introduced growth techniques. We present them in Fig. 2.20(b)-(d)

- (b) Lateral fin growth on a (112)-oriented substrate. Similar to Fig. 2.20(a) but with substrate orientation chosen such that fins will grow laterally. Growth can be nucleated either from holes or from etched mesa structures. Resulting layer orientation will be  $\{1\bar{1}00\}$ , ideal for layer epitaxy and crystal structure transfer. Though simple and elegant, this approach was not prioritized during this work.
- (c) Conformal epitaxy allows for engineering the morphology of the resulting material without compromising growth parameters. It is thus possible to choose the most commonly used (001)-oriented substrates. From an energetic point of view, tilted fin structures can be formed inside the oxide cavities, which provides for low growth facet to sidewall-ratio as required for single-crystalline WZ growth.
- (d) Epitaxial lateral overgrowth of fins into layers. As the stacking order in lateral direction is strongly fixed, phase transfer is expected in such an epitaxy, even when growth conditions are heavily changed to promote growth along  $\langle 1\bar{1}00 \rangle$ -direction. To achieve very high lateral growth rates we will make use of a zipper growth scheme in this work.

Even though with high potential, these techniques have not been studied until now for the growth of metastable III-V materials. In this work we will address 2 concepts for WZ layer growth as introduced in Fig. 2.20(c) and (d). Details of synthesis and characterization will be discussed in the following chapters.

## 3 Experimental Methods

*“What we find is that if you have a goal that is very, very far out, and you approach it in little steps, you start to get there faster. Your mind opens up to the possibilities.”*

– Mae Jemison

In this chapter, the experimental methods employed in this thesis will be reviewed. Starting from substrate preparation, we will discuss growth and in particular considerations for synthesis of metastable crystal phases for both conformal epitaxy as well as zipper-induced epitaxial lateral overgrowth. After that, the two main characterization techniques applied in this work will be discussed: Scanning transmission electron microscopy and micro-photoluminescence spectroscopy.

### 3.1 Conformal Epitaxy

Two approaches were followed in the course of this thesis to grow thin films of metastable III-V materials. We will first address conformal epitaxy, a technique which was traditionally developed to obtain thin films with high aspect ratio [240]. Various substrates were used as a basis for CE, including Si, GaAs and InP. To describe the fabrication process we will focus exclusively on the latter, for its importance in this work and considering the substantial similarities for the processing between all of them. Fig. 3.1 illustrates the basic steps.

- (a) Fe-doped 4 inch InP(001) wafers specified with an orientation accuracy of  $\pm 0.3^\circ$  and a resistivity  $> 10^7 \Omega\text{cm}$  were purchased from EL-CAT Inc. and are used as a substrate. A 4 nm protective SiO<sub>2</sub> layer is deposited by atomic layer deposition (ALD) at 300°C directly after unpacking from the original box. Another 50 nm SiO<sub>2</sub> is deposited using plasma-enhanced chemical vapor deposition (PECVD) at 400°C with tetraethyl orthosilicate (TEOS) as precursor material. Subsequently, 100 nm W are sputtered and
- (b) patterned using e-beam lithography (EBL) and reactive ion etching (RIE) with CF<sub>4</sub> chemistry. These structures will be used as markers for EBL alignment. Resist stripping

and cleaning steps were always carried out using acetone followed by isopropanol, and in some cases plasma ashing in oxygen.

- (c) A second lithography step is applied in order to pattern openings, in the form of holes and lines. RIE with  $\text{CHF}_3$  chemistry followed by a short buffered hydrofluoric acid (BHF) dip are used to transfer these patterns into the oxide and expose the crystalline substrate.

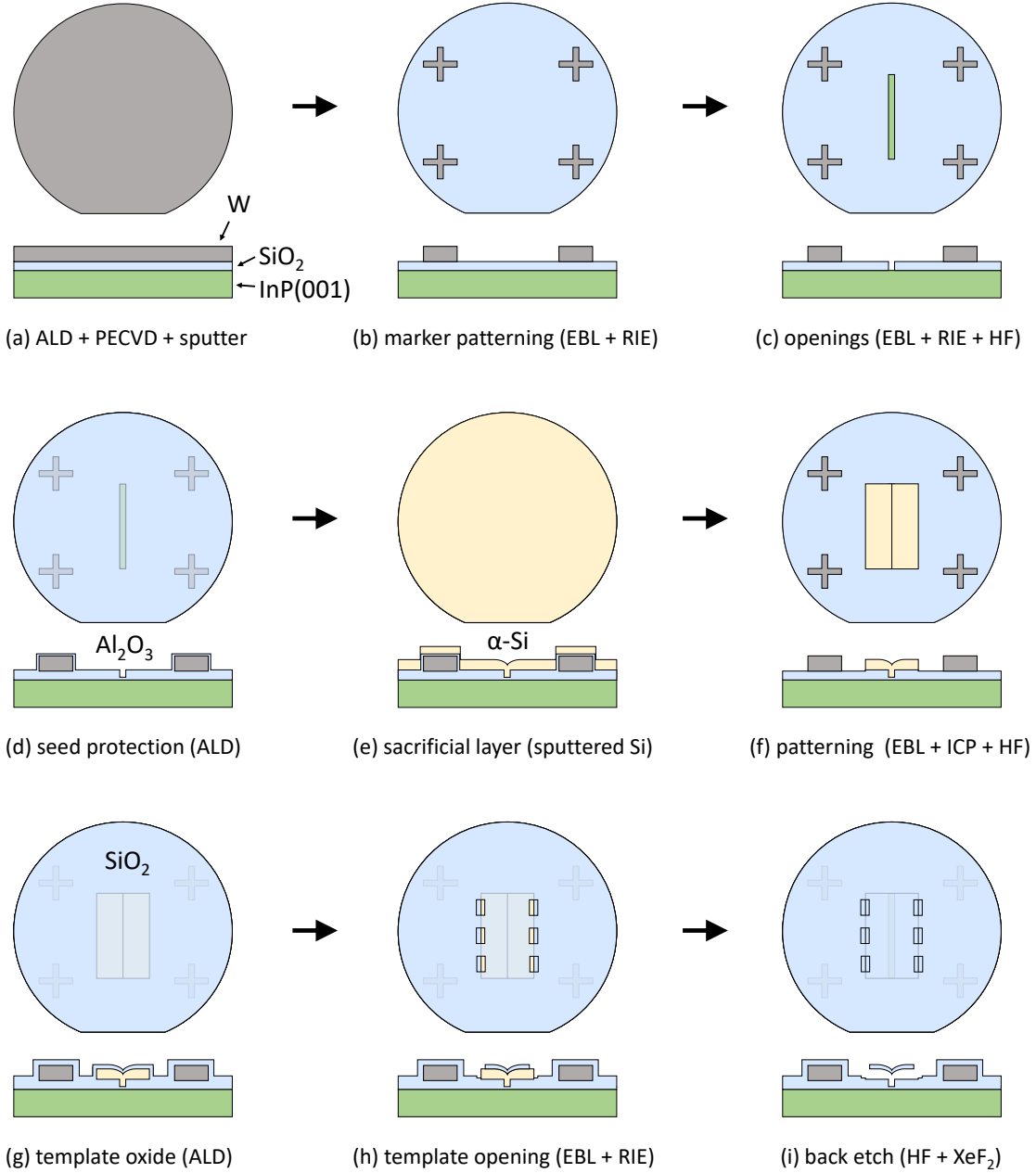


**Figure 3.1** | Fabrication steps for conformal epitaxy viewed from top and as a cross-section. Detailed description is given in the main text.

- (d) A thin layer (4 nm) of  $\text{Al}_2\text{O}_3$  is deposited to protect the areas that will later serve as seed.
- (e) A sacrificial layer of amorphous silicon ( $\alpha\text{-Si}$ ) is sputtered, here either 50 or 100 nm.
- (f) Hydrogen silsesquioxane (HSQ) in combination with EBL is then used to pattern rectangular structures around the seed area which are transferred with inductively coupled plasma (ICP) RIE in  $\text{SF}_6$  chemistry. A short dip of diluted HF (1:20) removes the remaining  $\text{Al}_2\text{O}_3$ , except below the  $\alpha\text{-Si}$ .
- (g) Again, ALD is applied to deposit 50 nm conformal  $\text{SiO}_2$ .
- (h) Holes are etched into the oxide furthest away from the opening to the substrate in order to expose the  $\alpha\text{-Si}$ .
- (i) After dicing the wafer into multiple chips and following a short dip in diluted HF, the sacrificial layer is removed in  $\text{XeF}_2$  chemistry.

Fig. 3.2(a) shows an SEM image of typical templates that have been fabricated according to these processing steps. Apart from the height of the template, several other parameters can be

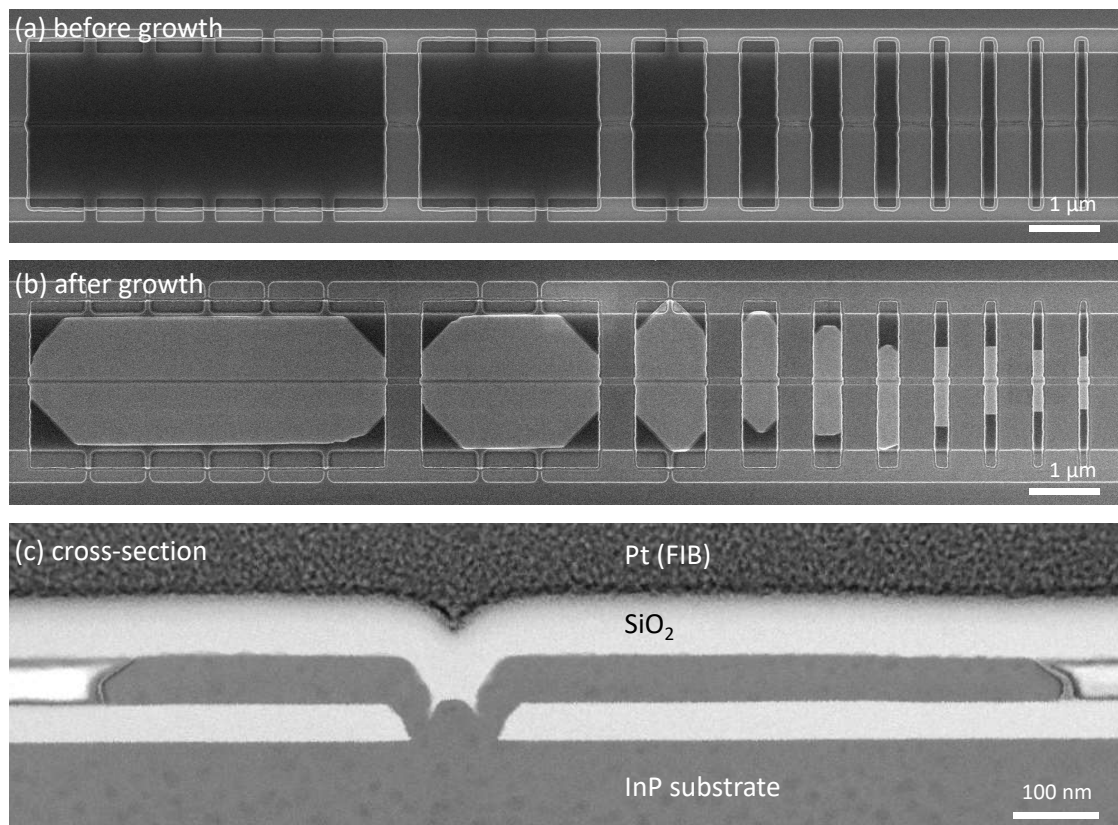


**Figure 3.2** | CE templates before and after growth. (a) Top-view SEM image of empty templates with varying sizes. (b) Typical crystals grown at 550°C for 60 min. (c) Cross-sectional view of a template after growth obtained during STEM characterization.

varied. This includes for example the template width or length but also and more importantly the orientation of the seed line with respect to the substrate. This orientation determines the crystalline directions along which the epitaxy proceeds and is thus crucial for the outcome of the growth experiment. Templates with variations of these parameters can be included in a single chip by modifying the design during EBL. It is thus possible to study how they affect the synthesized crystals independent from variations of the growth reactor.

In order to perform the growth experiment, the remaining  $\text{Al}_2\text{O}_3$  protection layer at the seed area is removed with HF:ethanol (1%) followed by isopropanol. The lower surface tension of these solvents compared to water prevents the templates from collapsing during the following drying step. The sample is then loaded into an MOVPE reactor, where it is heated in TBP atmosphere. For growth temperatures lower or equal to  $600^\circ\text{C}$  the deposition is initiated at the respective temperature by introducing TMIn. For higher temperatures, growth is initiated at  $600^\circ\text{C}$  and ramped up within the first minutes. This procedure was developed in order to prevent desorption of the thermally unstable  $\text{InP}(001)$  substrate surface at the seed line. For most experiments, partial pressures for TBP and TMIn were kept at 8.2 Pa and 82 mPa, respectively, to achieve a nominal V/III ratio of 100. Growth times are typically in the range of 30 to 60 min. After growth, substrates are cooled rapidly in TBP atmosphere until reaching a temperature below  $300^\circ\text{C}$ . An example of templates after growth is given in Fig. 3.2(b) and (c).

Until now we have discussed the general concept of CE. To obtain metastable crystal phases, additional considerations are needed. As mentioned earlier, growth needs to follow a  $\langle 111 \rangle$ -direction in order to induce a  $\text{ZB} \rightarrow \text{WZ}$  transition. Looking at the symmetry of a  $\langle 001 \rangle$ -oriented substrate, no such facet is available in lateral direction. However, even though the macroscopic growth direction is perpendicular to  $[001]$ , microscopical facet formation can be inclined during CE. This is possible because the template defines the shape of the crystal as compared to standard ELO. It can be assumed, due to symmetry reasons, that during epitaxy from a sufficiently long line seed the growth front will stay in parallel to the original nucleation line in the case of single crystalline deposition. It is thus important to consider growth facets that are

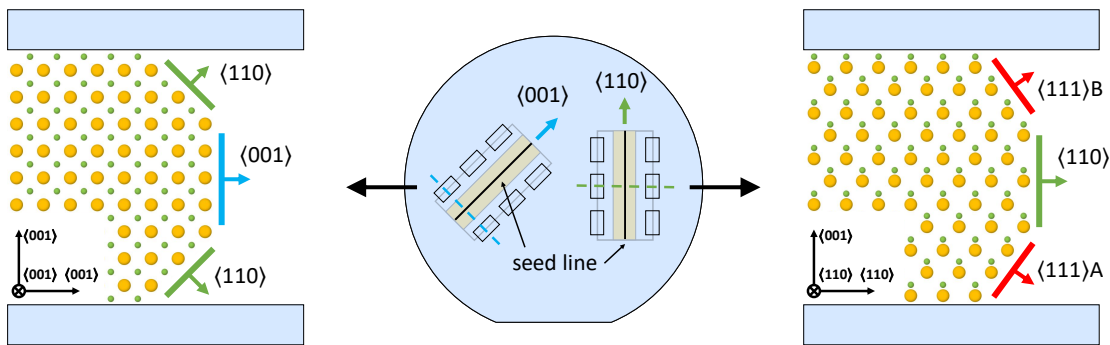


**Figure 3.3** | Cross-sectional atomistic model of possible low-index facet formation viewed perpendicular to the template-orientation for  $\langle 001 \rangle$ - and  $\langle 110 \rangle$ -oriented seed lines. Only the latter case allows for  $\langle 111 \rangle$ -facet formation during growth.

available in dependence of the template orientation. Fig. 3.3 compares possible low-index crystal facets which can be formed during epitaxy from line seeds oriented along  $\langle 001 \rangle$ - and  $\langle 110 \rangle$ -directions, respectively. Only in the second case  $\langle 111 \rangle$ -facets are available, which are essential for the synthesis of the metastable WZ phase. Additional considerations concern for example the growth conditions, which will be addressed in detail in **Chapter 4**.

### 3.2 Zipper-Induced Epitaxial Lateral Overgrowth

The second technique developed for the growth of extended metastable layers is referred to as zipper-induced epitaxial lateral overgrowth, or in short zipper-ELO. Even though process steps were adapted from sample to sample, an example of the basic fabrication steps is illustrated in Fig. 3.4

- Undoped 2 inch InP(111)A wafers with average roughness  $< 0.4$  nm were purchased from MTI Corp. and are used as a substrate. 10 nm  $\text{SiO}_2$  are deposited using ALD, after which 100 nm of W are sputtered and patterned by a combination of EBL and RIE.
- Another 50 nm  $\text{SiO}_2$  is deposited using PECVD at  $400^\circ\text{C}$ .
- A second lithography step is applied in order to pattern openings, in the form of holes and lines. RIE with  $\text{CHF}_3$  chemistry followed by a short BHF dip is used to transfer these patterns into the oxide and expose the crystalline substrate.

For different experiments various parameters such as hole diameter, line width or the total oxide thickness were modified. Details are given in the corresponding chapter.

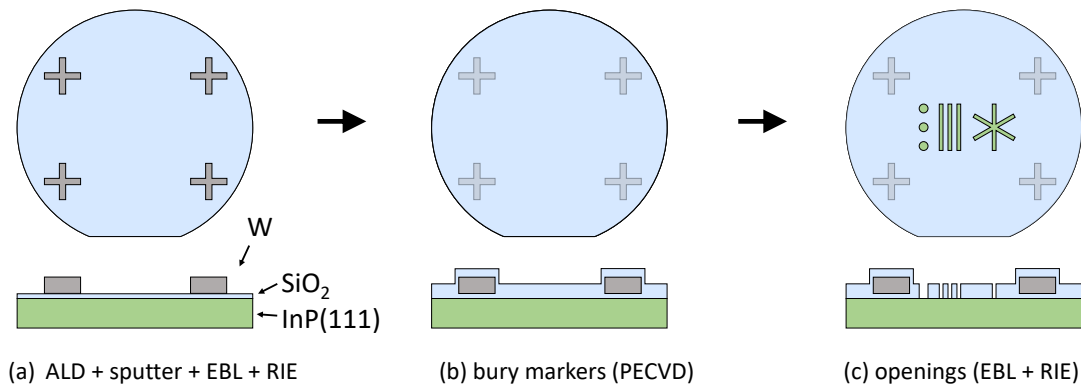


**Figure 3.4** | Fabrication steps for zipper-induced epitaxial lateral overgrowth viewed from top and as a cross-section. Detailed description is given in the main text.

As mentioned earlier, wire and fin growth can be initiated from such a masked substrate, and it has been shown that phase change can be obtained along the vertical direction given the correct growth conditions. However, the lateral growth rate of such fins and wires is very low.

Thus, ELO can not be observed directly, particularly under conditions where WZ phase is obtained as can be seen in Fig. 3.5(a).

In an attempt to overcome this limitation, the zipper mechanism as introduced in **Section 2.5** is applied. If two fins are merged at a central point, an unstable concave edge is formed, which creates high-index crystal planes, a so-called zipper point (Fig. 3.5(b)). As indicated in Fig. 3.5(c) these facets tend to have a high growth rate and a zipper-induced epitaxial lateral overgrowth is enforced. This growth continues until an enclosing low-index facet is formed as illustrated in Fig. 3.5(d). As this is a one-zipper mode with common growth origin, a defect-free layer filling can be expected. In particular, due to the growth direction perpendicular to the stacking orientation, a phase transfer into the layer is anticipated. As the fins can be grown in metastable WZ phase for InP, we will use this technique to produce metastable layers. More details will be given in **Chapter 5**.

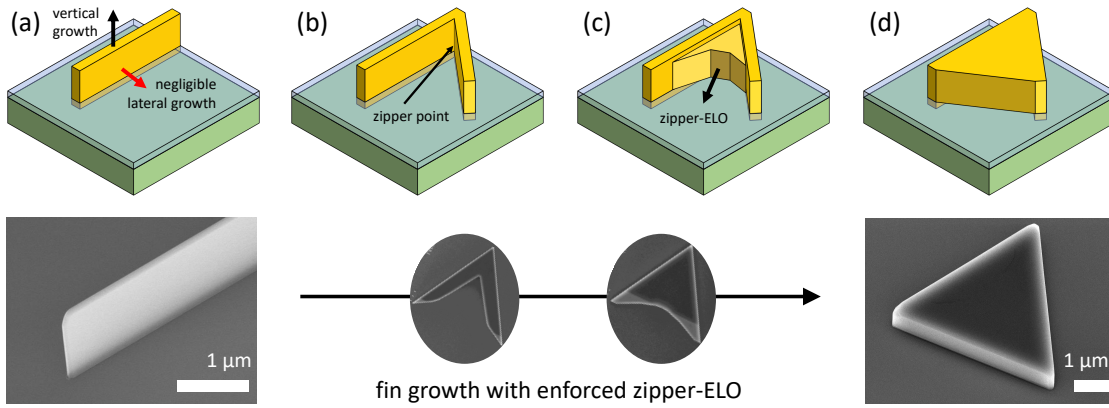


**Figure 3.5** | Mechanism of zipper-induced epitaxial lateral overgrowth. (a) During fin-growth on (111) oriented substrates, negligible lateral growth rate is observed. (b-c) To enforce lateral overgrowth a zipper point can be introduced. (d) The resulting crystal is convex and enclosed in low-index crystalline facets.

### 3.3 Structural Characterization using STEM

Scanning transmission electron microscopy is one of the main techniques to study crystal structure and defects. Consequently, large parts of the research work leading to this thesis were devoted to this instrument and we will explain the fundamentals here.

STEM is a powerful technique that enables atomic-resolution imaging of specifically prepared specimen. The main principle is illustrated in Fig. 3.6. In many ways the operation is similar to the more commonly used scanning electron microscope (SEM) [294]. An electron gun generates a beam of electrons that is focused by a series of lenses in combination with a condenser aperture. The electron spot, or probe, is then scanned across a defined area on the sample by scanning deflection coils. Spot-by-spot, these electrons interact with the specimen after which they are collected by various detectors which create an image, pixel-by-pixel. In

### 3.3. Structural Characterization using STEM

contrast to SEM, electrons transmitting through the sample are those of interest as opposed to back-scattered or secondary electrons. Thus, STEM requires a thinned sample with typically less than 100 nm in thickness. The reduced sample thickness is also responsible for the high resolution that can be obtained compared to conventional SEM [295]. Probe spreading within the sample is relatively small and the spatial resolution is primarily determined by the size of the probe which can be on the order of less than 1 Å [296], thus below the interatomic spacing of many materials.

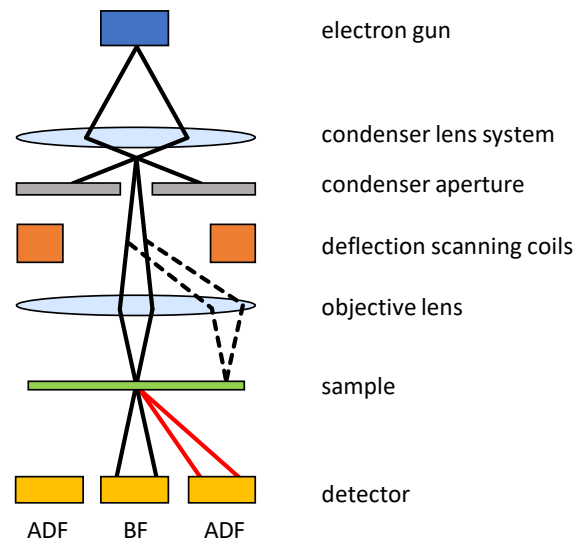


**Figure 3.6** | Simplified schematic of a typical STEM setup. An electron beam is strongly focused and scanned across a thinned sample. The transmitted and scattered electrons are collected by a range of detectors that are arranged concentrically around the optical axis.

Various detectors are used to obtain STEM images with different information. They are arranged in a concentric manner around the optical axis of the microscope [295]:

- A bright field (BF) detector is placed in the center. It records the intensity of the direct beam passing through the specimen and scattered electrons with low scattering angle. Atomic columns thus appear as dark spots in BF STEM, however the contrast is highly dependent on the sample thickness.
- An annular dark field (ADF) detector is a ring shaped semiconductor device that sits around the BF detector and collects electrons which are scattered from the optical axis. The measured contrast results from electrons diffracted in crystalline areas of the sample.
- As a special case of ADF, a high angle annular dark field (HAADF) detector is a ring with larger diameter, to detect electrons that are scattered into high angles (not shown in Fig. 3.6). This allows for the collection of nearly exclusively incoherent Rutherford scattered electrons and as a result obtaining images with strong atomic number contrast.

Apart from the principal operation mode with images created from the contrast of scattered electrons, additional instrumentation and detectors allow for the extraction of complementary information. For example, energy-dispersive x-ray (EDX) and electron energy-loss spectroscopy can be used to analyze the atomic composition of the specimen.

The STEM setup used in this thesis was a JEOL JEM ARM-200F, which is installed in the noise-free labs of IBM Research in Zurich. The instrument has a cold field emission electron source and is aberration-corrected for both TEM and STEM operation. An acceleration voltage of 200 kV allows for an estimated spatial resolution down to 80 pm. Sample preparation was carried out using an FEI Helios Nanolab 450S focused ion beam (FIB) instrument to fabricate cross-sectional lamellas. In order to investigate the stacking sequence of the crystal, the zone axis was oriented along the  $\langle 110 \rangle$ - or  $\langle 11\bar{2}0 \rangle$ -direction for ZB and WZ, respectively. Before cutting, the surface was protected with a Pt layer. After transferring the lamella to a dedicated TEM copper grid it is thinned down at the areas of interest to below 100 nm. Upon mounting on the sample holder, the grid was cleaned in oxygen plasma for 30 s and directly loaded into the TEM chamber.

### 3.4 Optical Characterization using $\mu$ -PL

Photoluminescence (PL) spectroscopy was frequently used in the course of this thesis to study optical properties of semiconductor crystals. For example, due to the different band gap energies, this characterization method allows to distinguish ZB and WZ InP. Time resolved photoluminescence (TRPL) measurements can give insights in carrier lifetimes and thus enable to draw conclusions on oscillator strengths and material quality. Moreover, lasing properties can be studied by optically pumping semiconductors, which constitute a resonant cavity as will be shown in **Chapter 6**. In the following we will give a short introduction to the technique and describe the specifics of the setup that has mainly been used for this work.

To measure PL, electrons in semiconductors are typically photoexcited from the valence to the conduction band. After a certain amount of time (carrier lifetime), an excited electron recombines with a hole and releases its energy in the form of a photon. These photons are collected and guided to a spectrometer, where the light intensity as a function of wavelength can be analyzed. It is important to note that depending on material quality and defects, not all recombination processes result in the emission of photons and so-called non-radiative recombination exists. Additionally, parameters such as surface quality, crystal morphology and setup alignment will strongly influence the amount of light that is collected, which makes quantitative analysis generally difficult. For most of the experiments presented here we will focus on qualitative comparison of dissimilar crystals, thus normalizing the spectral emission to its maximum value.

Two  $\mu$ -PL setups were employed. One setup is custom-built and capable of low temperature characterization down to 4 K. It further provides a single photon detector to measure e.g. TRPL, and a supercontinuum laser source with pulsed operation suitable for optical pumping. For

all measurements not requiring any of these features, a commercial optical spectrometer (Horiba scientific Labram HR) has been used, which is located in one of IBMs noise free labs. As sketched in Fig. 3.7, this instrument is equipped with a set of different lasers: A He-Ne laser, emitting at 633 nm and a Nd:YAGVO<sub>4</sub> diode pumped laser, emitting at 532 nm. In order to be able to excite electron-hole pairs, a wavelength needs to be chosen which is higher than the band gap energy of the material under investigation. With a few exceptions, most of the experiments presented here were performed using the laser emitting at 633 nm. An internal set of interchangeable neutral density filter allows for reducing the incident laser power by a factor of up to  $10^4$ . The laser beam is then guided to an objective where it is focused on the sample with a sub-micrometer spot-size. A three-axis piezo-stage enables lateral movements with nanometer-precision and automatic scans across the surface. A flip beam splitter allows for optical imaging of the sample and is used for aligning the laser spot to the desired area. Photons emitted by the sample are partially collected by the objective and follow back the the same optical path at first. An edge filter then splits larger wavelengths from the reflected excitation beam and guides them through a confocal hole and a slit before they hit a grating with 300 grooves per millimeter. The grating disperses the light onto a Si-based CCD spectrometer, where the wavelength-resolved light power is measured.

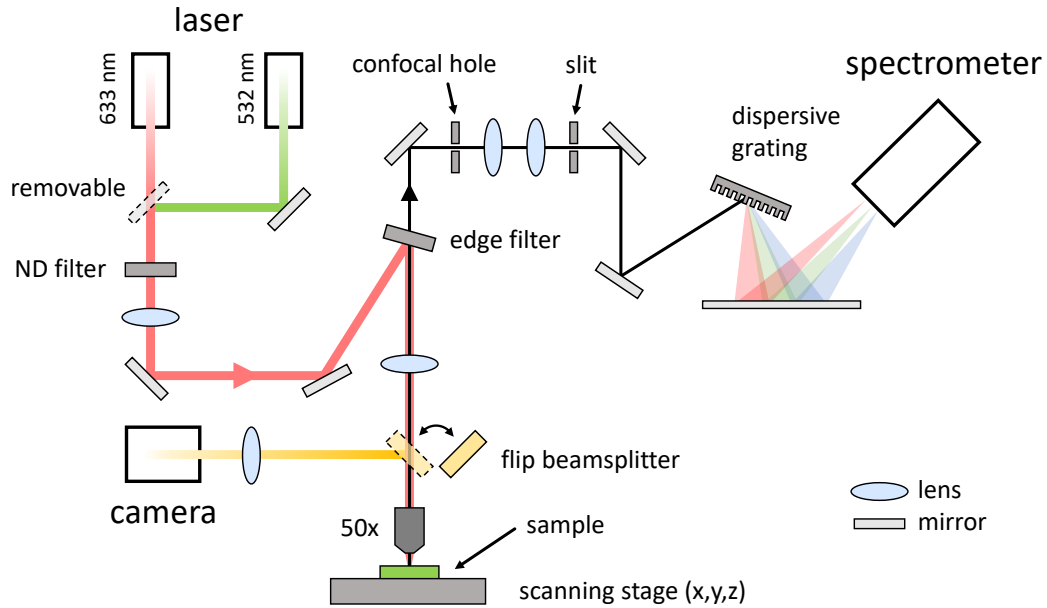


**Figure 3.7** | Schematic representation of the  $\mu$ -PL setup used for room temperature spectroscopy measurements. Image adapted from [297, 162].

We will apply these techniques along with others to synthesize and characterize crystal phase tuned III-V semiconductors in the course of this thesis. Complementary characterization performed during this work includes for example SEM, atomic force microscopy (AFM), cathodoluminescence (CL) and electrical measurements. Modifications and additional details are indicated for each experiment in the following chapters.



## 4 Metastable Film Formation by Conformal Epitaxy

As a first strategy towards wurtzite III-V film growth, conformal epitaxy will be explored. This technique, in different variations, has been developed in the late 1980s [240, 246] and has ever since been used to grow Si, Ge and III-V materials in the form of thin layers. Compared to standard layer epitaxy, the main target application was to synthesize semiconductor-on-insulator material, which improves performance for many devices such as field effect transistors [298]. While CE was largely displaced by wafer bonding for large scale fabrication of SOI substrates [299], it is now seen as a promising pathway for the local integration and co-integration of various materials to add functionalities to the mature CMOS technology platform [300, 301].

Owed to the epitaxy inside templates which are along (at least) one dimension confined to the nanoscale domain, many aspects of CE are similar to NW growth. For example, this technique is known to be plagued by stacking fault defects and rotational twins, which are rarely observed in standard planar epitaxy. Recent efforts demonstrated the ability of CE to grow defect free material in GaAs NWs [263] and InP layers [302]. This is explained by the formation of specific growth facets during the epitaxy. While twin-free III-V materials could be successfully synthesized, the potential of this technique for *crystal phase engineering* has largely been overlooked so far.

In this chapter, we present our results on crystal phase tuning using CE. As for the majority of this thesis, we will mainly use InP as a model material system. However, certain aspects are believed to be applicable to many other III-V semiconductors. In particular, the growth of III-Ns in their metastable zinc-blende phase could be an interesting application. The main findings have been published in a peer-reviewed journal and will be presented in the next section [303]. Some additional results will be discussed afterwards, including cathodoluminescence characterization and GaAs layer growth. The comprehensive findings have been presented at various international conferences, including the Compound Semiconductor Week 2019 [304] and the European Workshop on Metal-Organic Vapour Phase Epitaxy 2019 [305], where they have been recognized with the *Best Student Paper Award* and a *Young Scientist Award*, respectively.

## **4.1 Publication 1 | Concurrent Zinc-Blende and Wurtzite Film Formation by Selection of Confined Growth Planes**

Conformal epitaxy is a technique with high potential for the local integration of materials with added functionality. However, as of today, the crystallographic quality remains challenging to control, typically resulting in the formation of a large number of stacking faults and intermixing of ZB and WZ segments. Hence, achieving phase-pure material is one of the most important remaining challenges and could significantly boost the device performance by increasing quantum efficiency, carrier lifetime and mobility [306].

As discussed in **Section 2.7**, facet formation plays an integral part for phase transitions and their occurrence determines for example the presence of twin-defects [263], but also deposition rate or incorporation of dopants or growth species [262]. Achieving control of the facets that form during epitaxy is thus seen as a major milestone for realizing controlled integration of III-Vs with high material quality. Our study is the first comprehensive analysis of the effects of deliberate growth plane selection during conformal epitaxy on the structural properties of the deposited material. By exploiting the crystal symmetry of standard (001)-oriented substrates we were able to fabricate templates, which allow for designing the faceting during growth. Side-by-side we could thus compare crystals synthesized in the same run, but locally grown along different crystallographic orientations. In this study we focus on the analysis of two template orientations. One of them allows for the formation of local {111}-facets, while the other does not (compare **Section 3.1**). We could prove that only in the first case planar defects, such as stacking faults and rotational twins are formed. Using the other template orientation, we established defect free and thus phase-pure growth of ZB InP, which is one of the important results of this study. Going further, we could demonstrate that the amount of stacking faults in the first case is tunable by the growth conditions, in particular the reactor temperature. In the extreme case of 650°C, 97% of the bilayers were twinned (Fig. 4.5(a)), which corresponds to the WZ phase in nearly pure form.

As this is the first time that a III-V semiconductor could be deposited simultaneously in ZB and WZ phase with very high phase purity and with form factors beyond NW geometries, it is an ideal platform to study and compare various properties of stable and metastable phases. Besides the structural, we specifically focused on the optical properties, as they can give insights to the electronic band structure and thus the physics of the material under investigation. To exclude influences from the growth substrate we transferred grown crystals to a piece of polystyrene beforehand, which serves as a new handling substrate for photoluminescence experiments. Both at room as well as at cryogenic temperatures, PL spectroscopy revealed similar linewidth for WZ and ZB crystals, which indicates comparable crystal quality. Even bulk material showed only marginally narrower linewidth measured with the same setup. Additionally, we obtained a blueshift of 70 meV for the WZ phase, in agreement with earlier literature reports on WZ InP NWs. A lower lifetime could be an indicator for the theoretically predicted enhanced oscillator strength of WZ InP. Spatially resolved luminescence spectroscopy was performed by CL and will be reported in the next section. To explain our observations, we

further present an atomistic model for phase changes during conformal epitaxy.

The following article is reproduced with permission from *P. Staudinger et al.*, "Concurrent Zinc-Blende and Wurtzite Film Formation by Selection of Confined Growth Planes", *Nano Letters*, 18, 12, 7856–7862, 2018. © 2018 American Chemical Society. Further permission requests related to this material should be directed to ACS. With unchanged content from the post-print version, the text, layout and references of this article have been re-formatted in the style of this thesis.

For the work presented here, I performed the majority of experiments, including template fabrication, MOCVD growth, STEM investigation and PL characterization at room temperature. I further interpreted the results, developed a growth model and wrote the manuscript in collaboration with H. Schmid.

NANO LETTERS

Cite This: *Nano Lett.* 2018, 18, 7856–7862

Letter

pubs.acs.org/NanoLett

## Concurrent Zinc-Blende and Wurtzite Film Formation by Selection of Confined Growth Planes

Philipp Staudinger,<sup>✉</sup> Svenja Mauthe, Kirsten E. Moselund, and Heinz Schmid<sup>\*✉</sup>

IBM Research - Zürich, Säumerstrasse 4, 8803 Rüschlikon, Switzerland

### Abstract

Recent research on nanowires (NWs) demonstrated the ability of III-V semiconductors to adopt a different crystallographic phase when they are grown as nanostructures, giving rise to a novel class of materials with unique properties. Controlling the crystal structure however remains difficult and the geometrical constraints of NWs cause integration challenges for advanced devices. Here, we report for the first time on the phase-controlled growth of micron-sized planar InP films by selecting confined growth planes during template-assisted selective epitaxy. We demonstrate this by varying the orientation of predefined templates, which results in concurrent formation of zinc-blende (ZB) and wurtzite (WZ) material exhibiting phase purities of 100% and 97%, respectively.

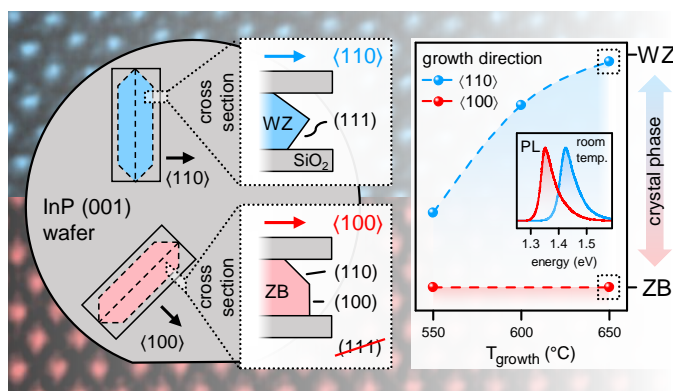


Figure 4.1 | Table of contents figure.

Optical characterization revealed a 70 meV higher band gap and a 2.5x lower lifetime for WZ InP in comparison to its natural ZB phase. Further, a model for the transition of the crystal structure is presented based on the observed growth facets and the bonding configuration of InP surfaces.

### Keywords

crystal structure, zinc-blende, wurtzite, indium phosphide, template-assisted selective epitaxy

### Main Text

Group III-V semiconductor nanostructures are key components for high-speed electronic [307], optoelectronic [308], and photovoltaic [17] applications due to their favorable material properties and the flexibility to employ various kinds of heterostructures [268]. One of the main challenges is the formation of high-quality material, because nanostructures and in particular grown NWs typically suffer from high densities of planar defects (PDs) such as rotational twins and stacking faults. PDs lead to lower performance by reducing quantum efficiency, carrier lifetime, and mobility as well as introducing nonradiative recombination centers and scattering planes [309, 310, 306]. Moreover, the control of the crystal phase is of key importance because, for example, for InP it has been reported both theoretically [42, 171] and experimentally [266, 105] that the band structure varies significantly between the cubic ZB and the related hexagonal WZ structure resulting in a bandgap energy difference of about 70 meV and type-II superlattices if they are intermixed [311, 169]. While it is obvious that uncontrolled polytypism limits the opportunities for applications, the possibility to selectively tune electronic and optical properties within the same material system by crystal phase engineering results in a unique degree of freedom for enhancing the functionality of emerging devices. Spirkoska et al. demonstrated the spatial carrier confinement in quantum-well structures formed by ZB/WZ heterostructures in GaAs [312], whereas other materials such as GaP, AlP and Ge even change the bandgap from indirect to direct when the crystal structure is converted from cubic to hexagonal [98, 42, 37]. These findings recently enabled efficient emission in the amber-green region of the visible spectrum from AlInP NWs [106] and may pave the way toward SiGe light sources with a bandgap close to the telecommunication wavelength [65]. So far however, the crystal phase remains challenging to control and phase intermixing is a commonly observed problem for III-V integration [120, 78, 263]. In addition, the two most explored techniques, vapor-liquid-solid (VLS) [63] and selective area growth [313], cannot surmount the size constraints of NWs with diameters below a few hundreds of nanometers causing fundamental challenges for device integration which is conventionally based on planar structures.

In this study we report on micron-sized InP layers epitaxially deposited inside hollow SiO<sub>2</sub> cavities on top of an InP(001) substrate. We demonstrate that the crystal structure can be controlled by confining and guiding the growth along specific crystalline directions, namely  $\langle 100 \rangle$  and  $\langle 110 \rangle$  for ZB and WZ, respectively. Thus, we achieve simultaneous formation of

planar films exhibiting both crystal phases at sizes up to  $50 \mu\text{m}^2$ . Crystal structure and defects are characterized by scanning transmission electron microscopy (STEM) along with micro-photoluminescence ( $\mu$ -PL) measurements and are found to be pure and without defects for ZB and with a stacking-purity of about 97% for WZ crystals. This is the first report demonstrating the fabrication of micron-sized WZ InP layers, thus opening new pathways for exploring fundamental material properties as well as establishing novel devices. Although InP was used as a model system, to some extent these findings are expected to be valid also for other compound semiconductor materials.

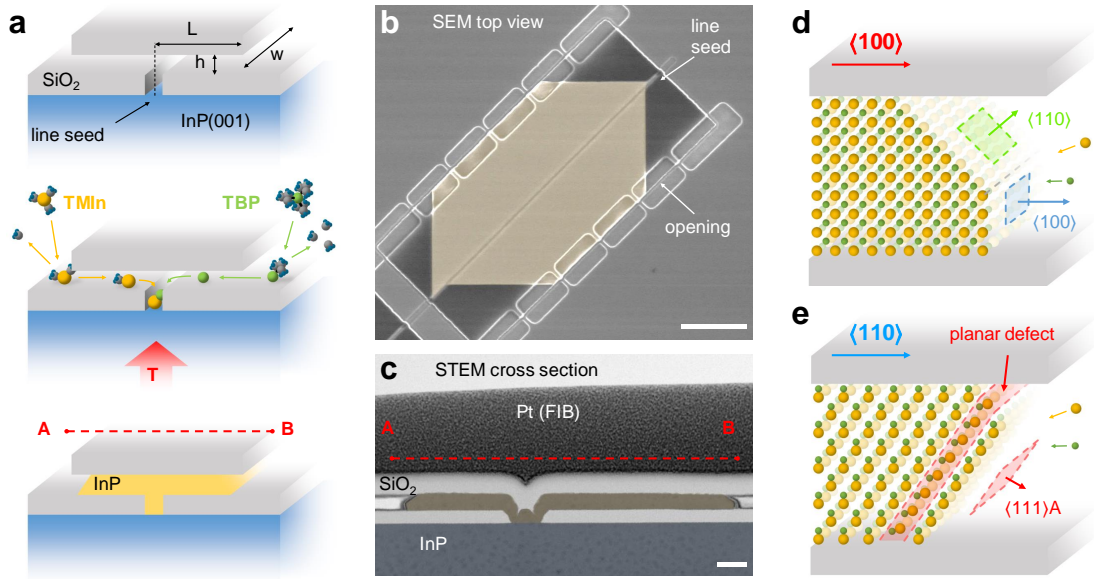


**Figure 4.2** | Experimental implementation of confined growth planes. (a) From top to bottom: empty  $\text{SiO}_2$  cavity as processed on top of an  $\text{InP}(001)$  substrate, sketch of the selective epitaxy process and template after MOCVD growth. (b) SEM top view image of an InP crystal after growth (colored in yellow). The crystal expands from the central line seed toward the openings. Scale bar:  $1 \mu\text{m}$ . (c) Low-resolution BF-STEM image showing the cross section of a crystal (yellow) on top of the  $\text{InP}(001)$  substrate (blue). Scale bar:  $100 \text{ nm}$ . (d - e) Illustrations to show faceting along different growth orientations.  $\{111\}$  facets and therefore PDs can only be formed when the crystals are grown along  $\langle 110 \rangle$ .

To grow InP films on  $\text{InP}(001)$ , we employ a method similar to template-assisted selective epitaxy (TASE) [253] but using much larger and elongated seed areas as reported in tunnel epitaxy [240], confined lateral selective epitaxial growth [243], or conformal vapor phase epitaxy [246]. In essence, we pattern line seeds on top of  $\text{SiO}_2$  covered  $\text{InP}(001)$  substrates, which are aligned along various crystalline orientations and capped again with an  $\text{SiO}_2$  layer (Figure 4.2(a) top). Selective epitaxy of InP is carried out in an MOCVD reactor using trimethyl-indium (TMIIn) and tertiarybutylphosphine (TBP) at a V/III precursor ratio of 100 and variable temperatures ( $T_{\text{growth}}$ ) until the templates ( $L = 1 \mu\text{m}$ ) are filled (Figure 4.2(a) bottom). Growth rates are in the range of  $0.5 - 1 \mu\text{m/h}$  depending on reactor conditions, with excellent selectivity to the  $\text{SiO}_2$  cavity. See **Methods** for more details on the process. An SEM top view micrograph of a typical crystal exhibiting a width  $w = 5 \mu\text{m}$  is depicted in Figure 4.2(b). Clear faceting demonstrates the homo-epitaxial and single-crystalline nature of the deposition process and

was observed irrespective of template width up to 50  $\mu\text{m}$  (the widest investigated in this study). A cross sectional low-resolution bright field (BF)-STEM image of another crystal is shown in Figure 4.2(c).

To demonstrate the effect of confined growth planes we compare films grown from two different template orientations. In the first case the line seed is oriented along  $\langle 100 \rangle$  and the crystals thus grow along another  $\langle 100 \rangle$  direction perpendicular to it (Figure 4.2(d)). Given that there is a single growth front in parallel to the seed line, which is typically observed in our experiments (compare Figure 4.2(b)), the local growth direction must lie within the plane perpendicular to this seed line. Low order facets in this direction include  $\{100\}$  and  $\{110\}$ , but notably no  $\{111\}$  facets along which PDs could be formed. Thus, we expect pure ZB phase for crystals grown along this direction [263]. InP grown along a  $\langle 110 \rangle$  orientation in contrast allows for different faceting, since both  $\langle 111 \rangle_A$  and  $\langle 111 \rangle_B$  directions are available locally and hence we expect to obtain PDs as indicated in Figure 4.2(e). In the second case, controlling the stacking sequence would yield the possibility to transform the crystal phase from ZB (ABC stacking) to other polytypes such as the WZ structure (ABAB stacking).

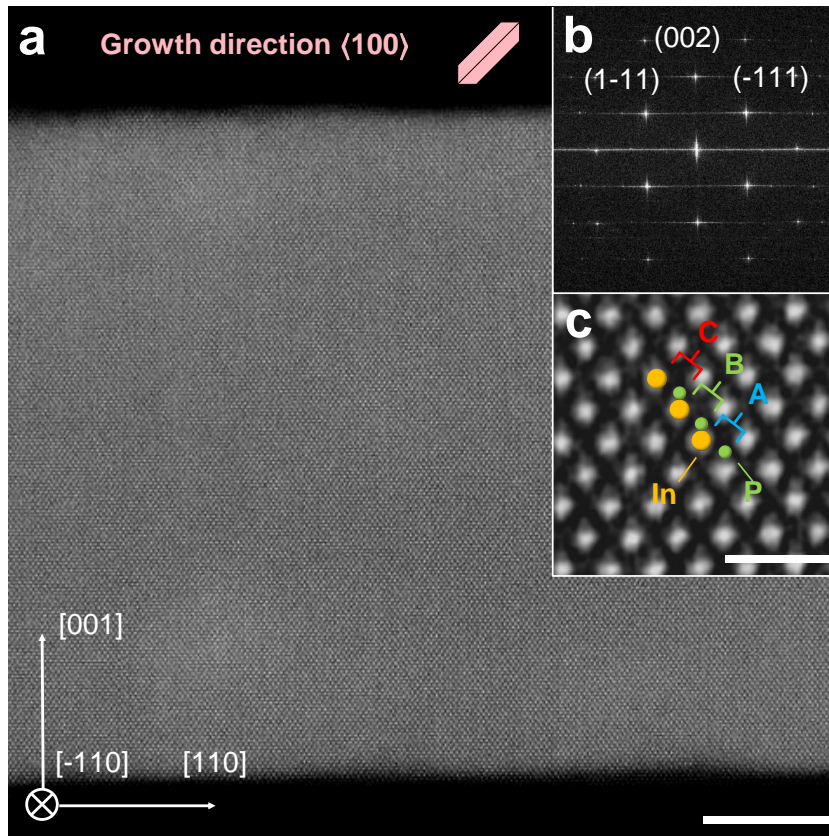


**Figure 4.3** | STEM investigation of an InP crystal grown along  $\langle 100 \rangle$ . (a) Cross-sectional overview of the film with height  $h = 50$  nm. Scale bar: 10 nm. (b) Corresponding FFT pattern showing ZB symmetry. (c) HR-image demonstrating the ABC type stacking. Scale bar: 1 nm.

First, we characterize crystals grown along the  $\langle 100 \rangle$  direction using STEM. Figure 4.3(a) depicts

a representative high angle annular dark field (HAADF) image of a film grown at standard conditions for InP growth ( $T_{\text{growth}} = 550^{\circ}\text{C}$ ,  $V/\text{III} = 100$ ). Note that the zone axis is  $[\bar{1}10]$  and thus not perpendicular to the growing direction but rotated by  $45^{\circ}$ . The entire cross-section of the  $h = 50$  nm high film is shown in this image. We have not found any defects along the entire crystal and thus pure ZB phase is obtained, which is attributed to the specific growth geometry and the related absence of  $\{111\}$  facets. Figures 4.3(b)-(c) depict the corresponding fast Fourier transform (FFT) pattern as well as a high-resolution (HR)-STEM image showing the ABC type ZB stacking.

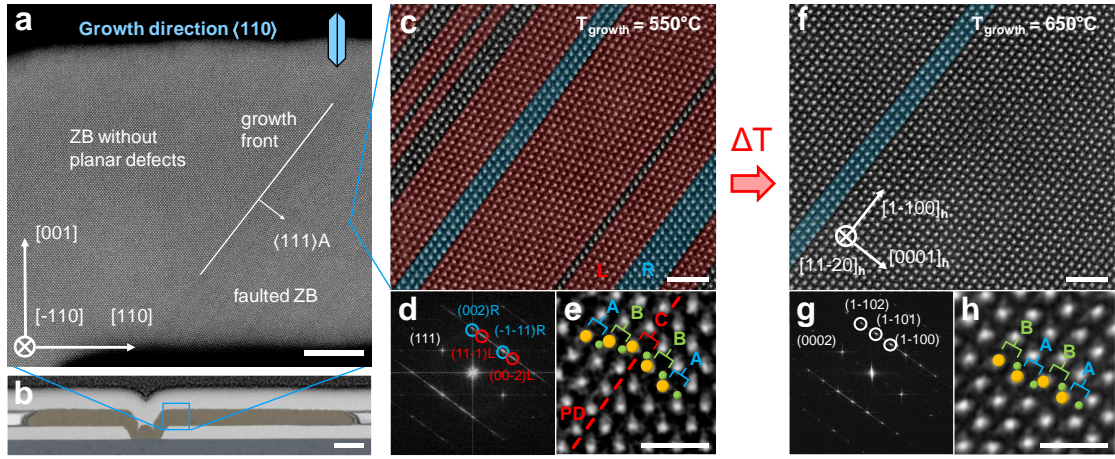


**Figure 4.4** | STEM investigation of InP films grown along  $\langle 110 \rangle$ . (a-b) Cross-sectional overview of the crystal with height  $h = 50$  nm close to the seed area. Scale bars: 10 nm and 100 nm. (c, f) HR-STEM images of InP crystals grown at  $550^{\circ}\text{C}$  and  $650^{\circ}\text{C}$ , respectively. Colored areas represent ZB segments with the two possible stacking orientations (ABC, CBA). Scale bars: 2 nm. (d, f) Corresponding FFT patterns showing faulted ZB and WZ symmetry, respectively. (e, h) Detailed micrographs of the crystal stacking. Scale bars: 1 nm.

Similarly, an InP film grown with identical conditions but along the  $\langle 110 \rangle$  direction is shown in Figures 4.4(a)-(e). First, we investigate the area close to the beginning of the growth as seen from the  $[\bar{1}10]$  zone axis indicated in the BF-STEM micrograph in Figure 4.4(b). We typically observe pure ZB InP without PDs for the first few tens of nanometers (Figure 4.4(a)), but as soon as the first PD occurs we immediately obtain a high defect density (1 PD/nm), as it is depicted in more detail in Figure 4.4(c). We therefore conclude that the crystal as it is expanding from the horizontal substrate follows growth directions deviating from  $\langle 111 \rangle$  in the beginning, however as soon as the (111)A facet is present it remains stable and PDs can be formed easily due to its high susceptibility to twinning. The presence of these PDs also manifests itself in the corresponding FFT pattern presented in Figure 4.4(d). A single rotational twin and the related inversion of the stacking sequence is depicted in Figure 4.4(e) in more detail. In a second experiment the growth temperature is increased by  $100^{\circ}\text{C}$  to  $T_{\text{growth}} = 650^{\circ}\text{C}$ , by ramping up from  $600^{\circ}\text{C}$  within the first 5 min, to prevent desorption of the otherwise unstable InP (001) surface under the growth conditions accessible in our MOCVD reactor. As shown in Figures 4.4(f) the number of ZB segments is reduced strongly. Although only a small area is shown in this image we observe similar crystal quality and defect density throughout

the entire template, apart from the area close to the seed. The characteristic FFT pattern and ABAB stacking sequence along the  $[0001]_h$  direction are clearly visible in Figures 4.4(g)-(h) demonstrating the formation of nearly pure WZ material. At the beginning of the growth we obtain pure ZB material again, followed by a short polytypic region (20 nm), which we believe originates from the temperature ramping procedure.

We use statistical analysis proposed by Joyce et al. [286]. to quantify the crystalline purity of our InP films. Every deviation from the perfect ZB stacking order (ABC) is accounted for as a single twinned bilayer (e.g. ABA). As the proportion of twinned bilayers in ZB InP is increased from 0 to 100%, the crystal phase is thus transferred to pure WZ. In Figure 4.5(a) we employ this analysis for different growth temperatures and directions by counting PDs in HR-STEM images. We observe that the number of twinned bilayers increases with temperature from 32% to 97% for films grown along  $\langle 110 \rangle$  to nearly pure WZ at 650°C. InP grown in  $\langle 100 \rangle$ -direction on the other hand remains free of PDs and is pure ZB in any case. Hence, we achieve simultaneous formation of both phases during the same growth run as demonstrated in Figures 4.5(b)-(g). Increasing the temperature further is expected to result in even higher phase purity, however the TBP pressure in our MOCVD reactor was not sufficient to stabilize the InP surface under such conditions.

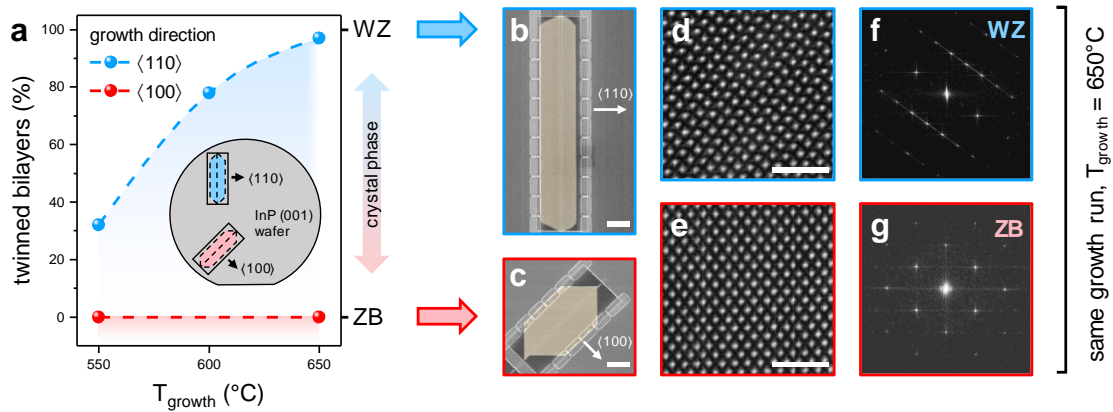


**Figure 4.5** | Simultaneous growth of ZB and WZ InP layers. (a) Number of twinned bilayers as a function of growth temperature for InP films grown along  $\langle 110 \rangle$  and  $\langle 100 \rangle$ . Simultaneous formation is achieved at 650°C. (b, c) Colored top-view SEM images of typical crystals. Scale bars: 1 μm. (d, e) HR-STEM images of InP crystals grown along  $\langle 110 \rangle$  and  $\langle 100 \rangle$ , respectively. Scale bars: 2 nm. (f, g) Corresponding FFT patterns showing WZ and ZB symmetry, respectively.

To further confirm the crystal phase transition and purity, we perform  $\mu$ -PL on individual crystals after removal from the underlying InP substrate to exclude measurement interferences (see **Methods** for more details). Figure 4.6(a) depicts representative  $\mu$ -PL emission spectra of InP crystals grown along  $\langle 100 \rangle$  and  $\langle 110 \rangle$ , respectively, as well as of bulk InP as a reference. The PL measurements reveal a blueshift of about 70 meV for crystals grown along  $\langle 110 \rangle$  with respect to bulk InP and crystals grown along the  $\langle 100 \rangle$  direction. This shift, which is clearly observed for RT and low T measurements, is thus attributed to the phase change of the material. For WZ InP we extract band gap energies corresponding to 1.41 and 1.47 eV for 293 K and 5 K,

respectively, which is in excellent agreement with previous reports on WZ InP NWs [311, 205]. Additionally, at low T we obtain a much smaller emission peak exactly at the position of bulk InP. This is believed to be due to the area close to the seed line which is ZB irrespective of template orientation. The FWHM of the spontaneous emission peaks for crystals grown along  $\langle 100 \rangle$  and  $\langle 110 \rangle$  is comparable to the one measured for bulk InP indicating high material quality and phase purity. Further, we use time-resolved PL (TRPL) to assess the overall effective carrier lifetime in our InP films. In Figure 4.6(b) we compare TRPL-measurements performed at 5 K from two crystals obtained during the same growth run and having the same defined morphology, the only difference being the growth direction and thus crystal phase. We obtain a 2.5-fold longer lifetime for ZB InP. According to the equivalent crystal morphology and assuming that there is no fundamental difference between the quality of the WZ and ZB InP surfaces, we thus conclude that the shorter exciton recombination lifetimes are an inherent property of the crystal phase and reflect the increased oscillator strength of the optical transition at the  $\Gamma$ -point [173, 314]. These findings suggest the enhanced light emission from WZ InP as compared to its natural ZB crystal structure, which could result in more efficient light sources.

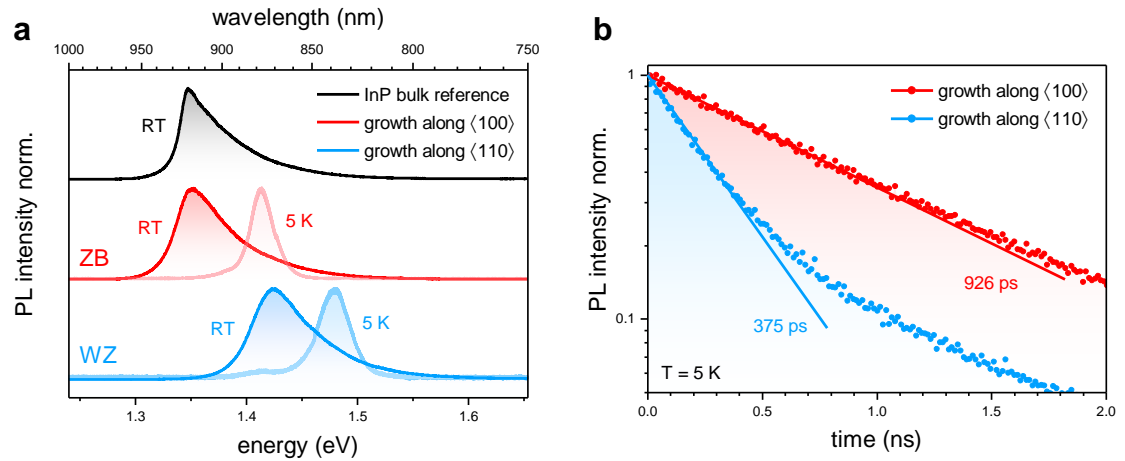


**Figure 4.6** | PL measurements of ZB and WZ InP films. (a) Normalized emission spectra of typical crystals along with bulk InP(001) at room temperature (RT) as well as 5 K. (b) Normalized TRPL measurements at 5 K demonstrate lifetime differences of ZB and WZ InP crystals exhibiting the exact same morphology.

Next, we describe a model to explain the structural transition observed in crystals grown along the  $\langle 110 \rangle$  direction. It is crucial to understand which type of facets are formed during the deposition process as they have a substantial influence on the growth dynamics. For example, PDs which are essential to facilitate a phase transition are exclusively formed along either the ZB  $\langle 111 \rangle_A$  or  $\langle 111 \rangle_B$  direction. In Figure 4.7(a) we show the end facets of a typical WZ InP film, which consist out of a relatively small  $(0001)_h$  A facet at the bottom and a larger  $(1\bar{1}00)_h$  facet perpendicular to it. As sketched in Figure 4.7(b), the stacking sequence can easily be changed along the  $\langle 0001 \rangle_h$  direction which corresponds to the  $\langle 111 \rangle$  direction in ZB. Hence, a transition from ZB to WZ is possible without introducing miscoordinated atoms [100].

The question remains, why under certain conditions WZ stacking is preferred over ZB, which is known to be more stable in bulk form. Earlier experiments on vapor-liquid-solid (VLS) grown NWs suggest that, once a nucleus of critical size is formed it spreads out laterally over the entire surface resulting in a layer-by-layer deposition mechanism [80, 83]. The orientation of the initial nuclei for every layer therefore determines the stacking sequence and thus the crystal phase of the resulting material. It is further known from VLS growth that if such a nucleus is formed at the edge to the  $(1\bar{1}00)_h$  facet, WZ is preferred to minimize the overall surface energy, otherwise ZB stacking is energetically more favorable under typical growth conditions [70, 264]. Hence, it is important to control the position of the nuclei on the  $(0001)_h$  A surface to achieve control over the crystal phase.

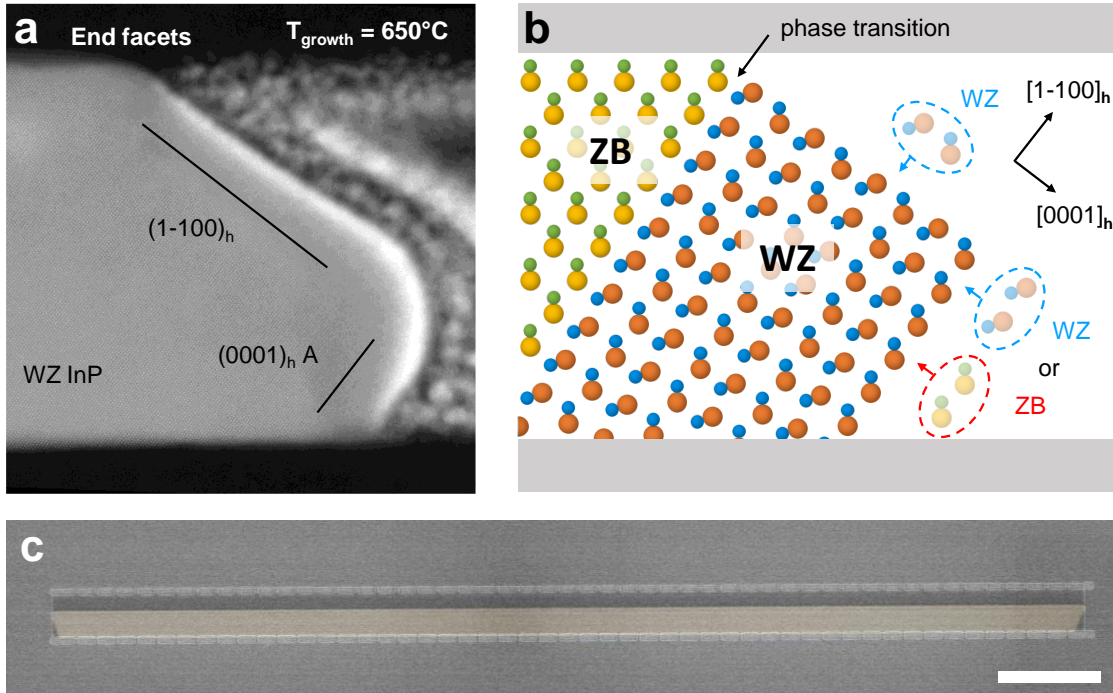


**Figure 4.7** | (a) End facets of a typical InP film grown in  $\langle 110 \rangle$  direction and exhibiting WZ phase. (b) Atomistic model for structural transition in InP crystals. The variable stacking axis along the  $[0001]_h$  A direction allows for an initial phase transition, which needs to be maintained during growth by forming nuclei at the edge toward the  $(1\bar{1}00)_h$  facet. In  $[1\bar{1}00]_h$  direction the stacking is strongly fixed and the WZ structure is transferred irrespective of growth conditions. (c) WZ InP film exhibiting a width  $w = 50 \mu\text{m}$  and a length  $L = 1 \mu\text{m}$  demonstrating the scalability of this approach. Scale bar:  $5 \mu\text{m}$ .

Keeping this information in mind, we can have a closer look at the InP  $(111)A / (0001)_h$  A surface. It is reported both theoretically [284] and experimentally [285] that its surface reconstruction is either In-rich  $(2 \times 2)$  or P-rich  $(\sqrt{3} \times \sqrt{3})R30^\circ$  depending on growth temperature and precursor partial pressures. In the former case, which is at high  $T_{\text{growth}}$  [284], to proceed growth on the In-terminated surface, P atoms need to be adsorbed first. However, this bonding configuration is thought to be weak since it has only a single bond toward the surface, and the P atoms are desorbed easily [268]. We thus speculate that under such conditions the formation of nuclei exceeding the critical size becomes unlikely at the surface. Instead new layers start to

form at the edge toward the  $(1\bar{1}00)_h$  facet where a high amount of dangling bonds is available and WZ phase is preferred in analogy to the existing models for the much more explored VLS technique [70]. This model can explain how the WZ phase becomes more dominant at higher  $T_{\text{growth}}$ , because the direct nucleation at the surface is suppressed and new nuclei are forced to be formed at the edge line. This is also in agreement with the fact that we observe a decrease of the growth rate when  $T_{\text{growth}}$  is increased from 550°C to 650°C.

Our model suggests that a low ratio between the  $(0001)_h$  A surface and its accompanying edge to the neighboring  $(1\bar{1}00)_h$  facet is required to prevent ZB nucleation on the  $(0001)_h$  A surface. Because in NW growth this ratio scales with diameter, stable WZ formation has not been observed in NWs exceeding a few hundred nanometers, nor in any planar epitaxy. For the same reason, increasing the height ( $h$ ) of InP films grown by TASE is expected to result in polytypic material at a certain point. However, this ratio is constant irrespective of another parameter in our constrained geometry: the template width ( $w$ ). We do not believe that there is any restriction to this value, which would enable the growth of arbitrarily wide crystals in a planar way. This was demonstrated by growing WZ films exhibiting an area of  $50 \mu\text{m}^2$ , as shown in Figure 6c. Using such planar films as virtual substrates by subsequently transferring the crystal phase in vertical direction holds great promise for integrating more complex WZ thin-film heterostructures, perfectly suited for electro-optical devices.

In conclusion, by carefully selecting confined growth planes using TASE, we achieved the concurrent growth of pure ZB and nearly pure WZ InP films. Thus, we demonstrated a new pathway for facilitating complete phase transitions in a III-V material system. STEM, FFT and PL analysis revealed the phase purity and optical quality of the obtained crystals and demonstrated a blueshift for the WZ phase in agreement with earlier literature reports on WZ InP NWs. By TRPL measurements we obtained lower exciton lifetimes in the WZ phase which is a strong indicator for the increased oscillator strength of the optical transition and the resulting enhanced light emission of the material. We further proposed a model to describe our findings and demonstrated the scalability of our approach by growing WZ InP at sizes up to  $50 \mu\text{m}^2$ . Remarkably, the growth of WZ InP has only been demonstrated in NW structures, with the first WZ film formation shown in this work. Our study provides a new route for facilitating phase transitions in large area III-V material growth, which could bring us one step closer to the integration of a new class of optical devices with outstanding properties.

## Methods

**Template Fabrication.** Line seeds with nominal widths of 50 nm were patterned along the  $\langle 100 \rangle$  and  $\langle 110 \rangle$  direction on a standard InP(001) wafer covered with 50 nm plasma-enhanced chemical vapor deposited (PECVD)  $\text{SiO}_2$  by e-beam lithography (EBL), reactive ion etching (RIE) and buffered hydrofluoric acid (BHF). Seeds were protected with 4 nm atomic-layer deposited (ALD)  $\text{Al}_2\text{O}_3$  after which 50 or 100 nm amorphous Si ( $\alpha$ -Si) was sputtered for structural and optical characterization, respectively. Sacrificial structures were patterned

perpendicular to the seed lines with varying widths and lengths using EBL, inductively coupled plasma (ICP)-RIE and a short diluted HF (DHF) dip to remove the  $\text{Al}_2\text{O}_3$  after which, the actual 50 nm thick  $\text{SiO}_2$  templates are deposited using ALD. The  $\text{SiO}_2$  is opened at the position furthest away from the seed line using EBL, RIE and DHF, and the  $\alpha$ -Si within is etched using  $\text{XeF}_2$  chemistry. Finally, the protective  $\text{Al}_2\text{O}_3$  at the seed line is removed by DHF directly before the growth.

**InP Growth.** InP film growth was performed by MOCVD using TBP and TMIn at a total pressure of 60 torr. Partial pressures for TBP and TMIn were kept at 8.2 Pa and 82 mPa, respectively to achieve a nominal V/III ratio of 100. Upon loading, the reactor was heated in a TBP atmosphere, and deposition was initiated subsequently by introducing TMIn. Growth temperature was held constant for growth at 550°C and 600°C and ramped up from 600°C within the first 5 min for growth at 650°C to prevent desorption of the thermally unstable InP(001) substrate surface at the seed line. Growth times were varied between 40 and 60 min. After growth, substrates were cooled under a TBP atmosphere until reaching a temperature below 300°C.

**Structural Characterization.** The structural quality of individual crystals was investigated by scanning transmission electron microscopy (STEM) along the  $[\bar{1}10]$  zone axis. The sample lamellas were prepared by means of a FEI Helios Nanolab 450S focused ion beam (FIB) either in parallel to the growth direction for films grown along  $\langle 110 \rangle$  or rotated by 45° for crystals grown along  $\langle 100 \rangle$ . BF and HAADF micrographs were generated using a double spherical aberration-corrected JEOL JEM-ARM200F microscope operated at 200 kV.

**Optical Characterization.** For optical characterization, crystals were transferred from their growth substrate to a piece of polystyrene (PS) after stripping the  $\text{SiO}_2$  templates with BHF. Two different  $\mu$ -PL setups were employed. At RT a continuous laser source at 633 nm was used to excite the InP layers in ambient conditions, whereas for measurements at 5 K the crystals were pumped using a pulsed supercontinuum laser at 640 nm (pulse length 15 ps at 78 MHz repetition rate) in vacuum. Both setups, RT and low T, excite, as well as collect the photoluminescent response from the top using a 50× objective and they are linked to a liquid nitrogen cooled Si CCD and InGaAs detector, respectively. TRPL measurements are performed at 5 K using the supercontinuum laser at 640 nm and 78 MHz, as well as a cooled InGaAs single-photon detector.

### Author Contributions

P.S. and H.S. conceived and designed the experiments. P.S. carried out template fabrication, MOCVD growth, STEM investigations and optical characterization at room temperature. H.S. prepared the TEM lamellas. PL and TRPL measurements at 5 K were done by S.M. All authors analyzed and discussed the results. The manuscript was written by P.S. and H.S., with contributions of all authors, and all authors have given approval to the final version of the manuscript.

## Acknowledgments

The authors gratefully acknowledge Antonis Olziersky, Marilyne Sousa, Yannick Baumgartner, Lukas Czornomaz, Emanuel Lörtscher, Anna Fontcuberta i Morral, Heike Riel and Walter Riess. The work presented here has received funding from the European Union H2020 program SiLAS (Grant Agreement No. 735008), the ERC Starting Grant project PLASMIC (Grant Agreement No. 678567) and the Swiss National Science Foundation under Project Number 200021\_156746.

## 4.2 Additional Results

Apart from the main publication, further results on conformal epitaxy have been established afterwards. For example, a detailed investigation of the growth evolution from ZB to WZ in templates oriented along  $\langle 110 \rangle$ -direction was carried out. An HR-STEM image of a typical crystal is shown in Fig. 4.8. As expected from the growth model, due to the absence of a  $\{111\}$ A-facet in the early stages of the growth, pure ZB material is formed at first (see inset 1). As soon as the first stacking fault is obtained along  $\langle 111 \rangle$ A-direction, immediately a high density of such is observed. Nevertheless, the density of stacking faults is still gradually increasing before nearly pure WZ material is obtained (inset 4). We attribute this to the ramping procedure of

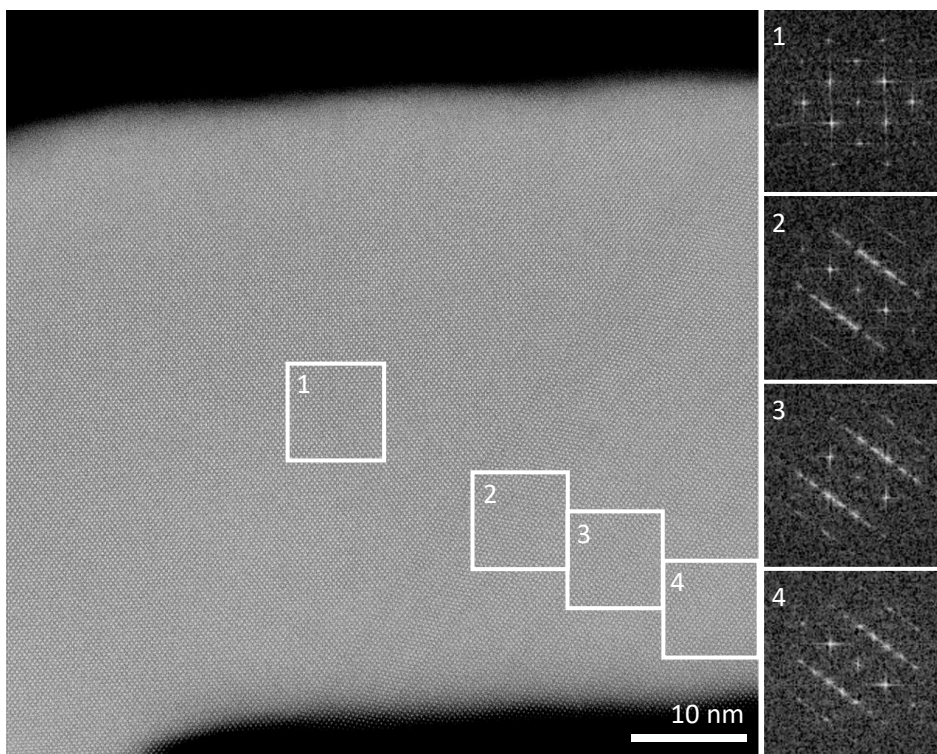


**Figure 4.8** | HR-STEM image of the phase transition in an InP crystal grown along  $\langle 110 \rangle$ -direction. The FFT patterns obtained from different areas along the growth direction demonstrate a transition from pure ZB to WZ within approximately 20 nm.

the growth temperature that was carried out during the first 5 min. Continuing further in growth direction, the defect density remains approximately constant.

Complementary CL characterization was carried out by N. Tappy at EPFL to obtain high-resolution data of the optical emission in grown crystals. Fig. 4.9(a) depicts room temperature emission spectra of a crystal grown along  $\langle 110 \rangle$ -direction at 650°C. The data is largely consistent with previous PL characterization. A clear blueshift of the optical emission is obtained in the grown planar film apart from the area close to the seed, which is consistent with the delayed phase transition as shown in Fig. 4.8. While STEM allows to characterize only small sections at a time, with CL we could prove that the entire crystal shows WZ emission as depicted in Fig. 4.9(c).

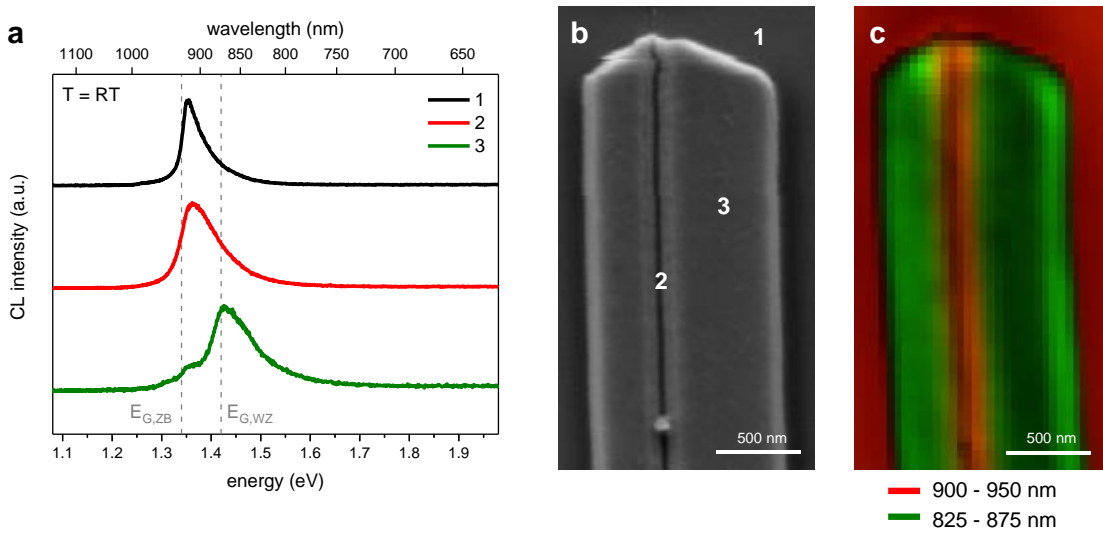


**Figure 4.9** | (a) Room temperature CL emission spectra of a crystal grown along  $\langle 110 \rangle$ -direction as obtained from 3 positions indicated in (b). (c) CL map showing integrated emission intensities from 900 – 950 nm (red) and 825 – 875 nm (green).

To prove the versatility of growth plane selection during CE, we performed additional experiments on GaAs. A complete set of new samples was fabricated for this purpose with GaAs(001) as substrate. Compared to InP, a higher growth uniformity could be achieved during epitaxy. To this end, however, grown films were limited to pure ZB and ZB with high amounts of planar defects. An example with direct comparison to InP is given in Fig. 4.10. HR-STEM images show that pure ZB phase can be obtained in both cases. However, the amount of planar defects observed in GaAs is significantly lower for growth along  $\langle 110 \rangle$ -direction, thus preventing us from growing pure-phase WZ GaAs. Future studies could investigate a larger range of growth parameters or the incorporation of dopants in order to induce a higher stacking fault density – and ultimately WZ phase.

In order to synthesize WZ GaAs layers in this research project, another, more elaborate technique was developed. As illustrated in Fig. 4.11, this approach combines the potential of phase switching during VLS growth and the stabilization of crystal structures by selection of

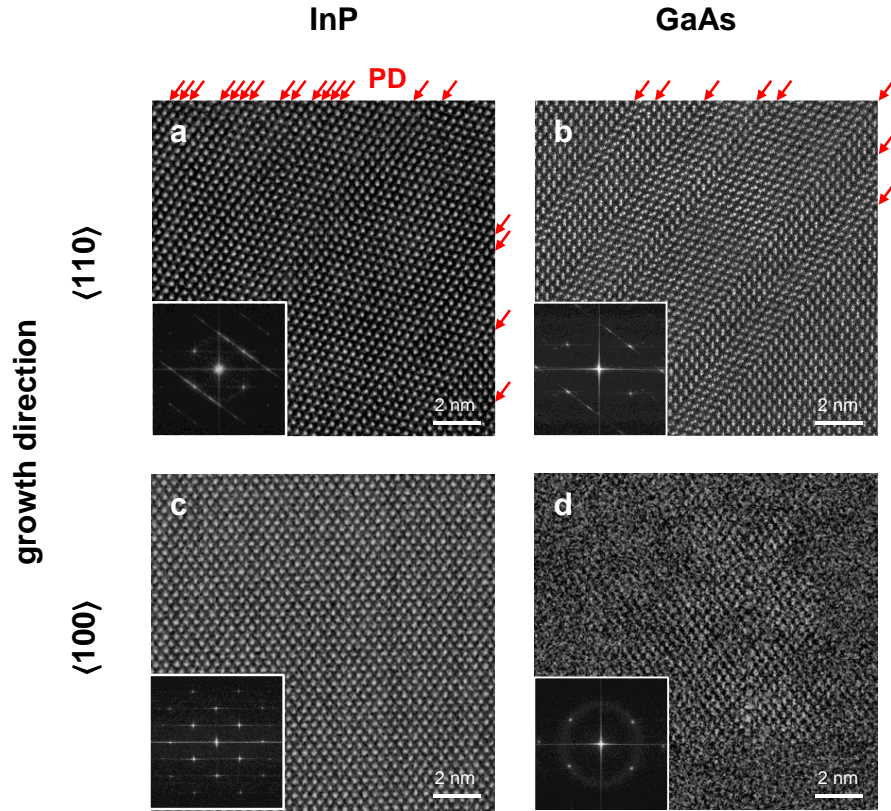


**Figure 4.10** | STEM investigation of InP and GaAs films. (a, b) HR-STEM images of InP and GaAs crystals grown along  $\langle 110 \rangle$ -direction. Red arrows indicate PDs as is also visible in the FFT patterns shown in the insets. (c, d) HR-STEM images of crystals obtained throughout the same growth run as in (a) and (b), respectively but grown along  $\langle 100 \rangle$ -direction. Pure and defect free ZB phase is obtained as substantiated by the FFT patterns depicted in the insets.

confined growth planes. First, a GaAs NW is grown by VLS along  $c$ -direction, which allows for phase change to pure WZ. Such NWs, in extraordinary length and quality, were supplied by our project partners around E.M.T. Fadaly and E.P.A.M. Bakkers at TU Eindhoven. Using a cleanroom wipe, the NWs are transferred to an  $\text{SiO}_2$  covered Si substrate, where they preferentially lie on one of their  $m$ -plane facets. This is important, as we can benefit from the low-index top surface of the resulting layer for an additional epitaxy step (see **Chapter 7**). In a specifically developed process we build a template around the NW. As a sacrificial material, an organic resist is used that can be patterned by e-beam lithography. The template itself is then formed with HSQ, which turns into  $\text{SiO}_2$  upon exposure in a second e-beam lithography step. In a following CE step the growth will be guided along  $a$ -direction. This direction is suitable for crystal structure transfer, as it is orthogonal to the only  $c$ -axis (stacking direction) in the WZ crystal phase. Hence it is expected that WZ GaAs will be formed.

To test this hypothesis, STEM characterization of such a film is performed as shown in Fig. 4.12. An in-plane lamella is prepared in order to enable imaging of the entire layer. By acquiring multiple HR-STEM images across the layer, we found pure WZ crystal phase, as exemplified in

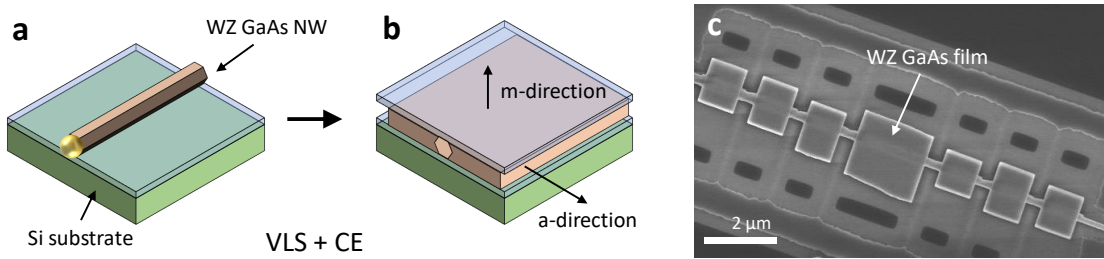


**Figure 4.11** | Two step epitaxy technique for synthesizing WZ GaAs films. (a) VLS-grown WZ GaAs NWs are deposited on a Si substrate covered by SiO<sub>2</sub>. (b) A template is built around the NW for CE. In a following GaAs epitaxy step, growth planes are confined to the a-direction, which effectively hinders phase-change. A WZ GaAs film is obtained with m-plane top surface. (c) SEM image of multiple GaAs films grown from a single NW after removal of the top oxide.

Fig. 4.12(c). Given the versatility of VLS growth, this technique could enable the synthesis of WZ films for a large amount of materials. Using NWs with twinning super lattices or with multiple crystal phases along the growth axis, these features should be expandable into layers, opening many interesting applications. A publication of the results in a peer reviewed journal is aspired, once more insights have been gained.

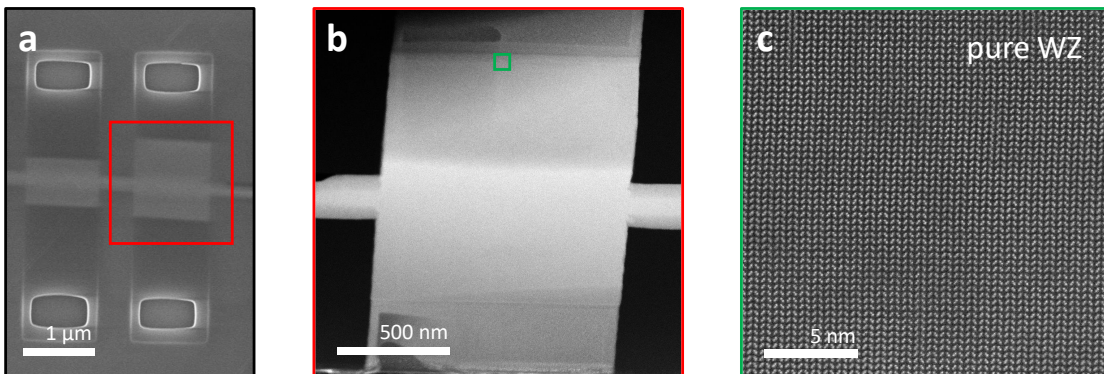


**Figure 4.12** | STEM characterization of a WZ GaAs film. (a) Top-view SEM image of film before lamella preparation. (b) Overview STEM image after preparing an in-plane lamella, viewed in an angle of 30° (along a-direction). (c) HR-STEM image at one extremity of the grown film. Pure WZ phase is observed.

## **4.3 Main Achievements**

In summary the following results and achievements have been obtained, extending the understanding and possibilities of metastable film synthesis:

- We studied the effects of confined growth planes during conformal epitaxy and found that only specific growth planes allow for phase change to metastable crystal phases.
- The first metastable WZ film of any III-V material was synthesized in this thesis.
- Using the effects of confined growth planes, both ZB and WZ InP films can be obtained concurrently in the same growth run in a controlled way, providing an ideal platform to study the properties of metastable phases.
- A growth model was developed, explaining our results.
- Experiments on other materials were performed, resulting in defect free ZB GaAs.
- We developed a two-step approach using a VLS seed NW to grow WZ GaAs layers.
- We found indications for a higher oscillator strength at the  $\Gamma$ -point in WZ InP, favorable for optoelectronic applications.
- The band gap energy was determined to be 70 meV higher in WZ InP across a large temperature range, in accordance with theory and experiments on NWs.
- The work presented in this chapter was recognized with the *Best Student Paper Award* at CSW2019 in Japan and the *Young Scientist Award* at EW-MOVPE 2019 in Lithuania.
- We filed 2 US patent applications related to this research work.



## 5 Metastable Film Formation by Zipper-Induced Epitaxial Lateral Overgrowth

Whereas conformal epitaxy allows for the highest control over the growth conditions and substrate orientation and offers additional advantages such as lateral doping profiles or co-integration of multiple materials, it is an elaborate technique that requires careful preparation of the substrate and a large number of fabrication steps. For advanced applications we believe that it has the highest potential with a clear route towards lattice mismatched hetero-integration on standard Si substrates. However, in order to produce large layers in an economical way, we were exploring other approaches that require less substrate preparation.

In an effort to increase crystal sizes of metastable materials, fin growth has been investigated in the past [108]. This technique, similar to SAE of NWs, allows for phase change along the  $\langle 111 \rangle$  growth direction. Thus, (111)-oriented substrates are typically used in order to obtain vertical WZ fins enclosed in m-plane facets. Interestingly, these facets, similar to NW sidewalls should allow for phase transfer along lateral direction (compare **Section 2.7**). To prove this hypothesis, we performed experiments on core-shell fin structures. InGaAs or InAlP was deposited on WZ InP fins directly after growth and characterized by STEM. Fig. 5.1 depicts typical results obtained for InAlP. Indeed, the WZ stacking established during vertical InP fin growth was transferred in lateral direction to the InAlP layer.

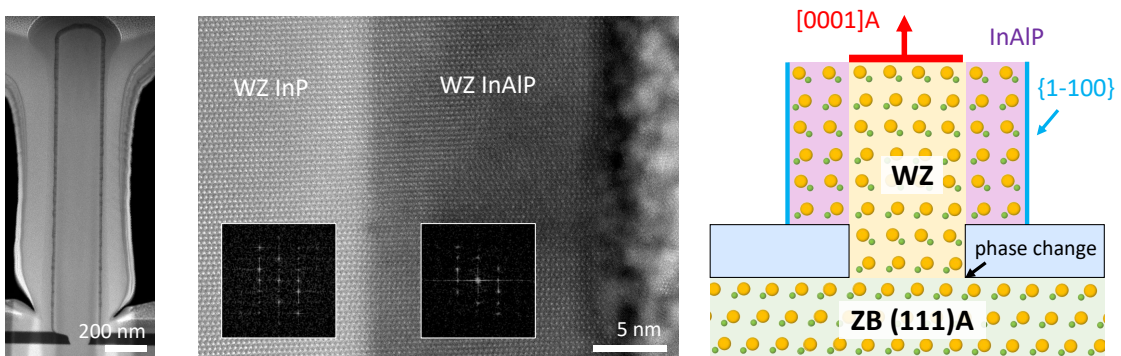


**Figure 5.1** | STEM characterization of InP-InAlP core-shell fins. The metastable WZ crystal phase of the fins is transferred to the InAlP shell.

On the other hand, ELO techniques exist, in which lateral growth dominates over vertical one. To achieve this in a conventional way, growth conditions must be met or specific substrate orientations used. However, these parameters are substantially restricted if at the same time phase change should be obtained. As a matter of fact, such an epitaxy has not been reported in literature to the best of our knowledge.

Instead, to combine the potential of phase change fin growth with the favorable planar form factor of ELO, we apply a trick that makes use of so-called zipper points (compare **Section 2.5**). Fins that are grown in different but crystallographically equivalent directions can be merged in a central point. Concave edges that are formed in such a way are unstable during growth and expand laterally over the oxide layer. Thus, a film is formed which is isolated from the substrate. Due to the phase transfer along lateral direction, the metastable phase is obtained in the entire film. We call this technique zipper-induced epitaxial lateral overgrowth, and abbreviate it to zipper-ELO.

In this chapter we will investigate scaling of WZ films grown by zipper-ELO and explore size limitations related to epitaxy of metastable crystals. Our main findings have been published in a peer reviewed journal [315] and will be presented in the following sections.

### 5.1 Publication 2 | Exploring the Size Limitations of Wurtzite III-V Film Growth

After successfully demonstrating zipper-ELO to be a viable technique for obtaining planar layers of WZ III-V materials, we were addressing the question of how far we can increase the film dimensions before they will relax to their thermodynamically preferred stable phase. Such a limitation is believed to exist due to the energetics of the metastable system. However, the exact value can depend on details of the growth process which will determine not only the diffusion lengths of adatoms but also the energy difference between the two stacking positions during growth. Given the restricted deposition parameters to obtain WZ films in our MOVPE reactor, we could not study such an effect. Instead we focused on the limitation at given growth condition and compared it with epitaxy from extended hole openings. In this way we established a transition point from WZ to ZB of around  $100\text{ }\mu\text{m}^2$ . Our publication is not only the first comprehensive study exploring the size limitations of metastable film synthesis, but also laying out growth strategies in order to achieve unprecedented WZ layer dimensions.

To scale films grown by zipper-ELO, an intuitive approach is to increase the diameter of the underlying star pattern. However, this will drastically increase the deposition time as the lateral expansion can slow down when intermediate low-index facets are formed. Hence, we followed an additional approach in which we tile individual star patterns. This allowed us to synthesize fully-grown large area films in relatively short deposition times. We studied crystal quality and phase purity of the obtained films by STEM as well as scanning  $\mu$ -PL. Based on our findings we further developed a model which is based on the formation of multiple

stacking-misaligned nuclei at extended growth surfaces.

The following article is reproduced with permission from P. Staudinger et al., “Exploring the Size Limitations of Wurtzite III–V Film Growth”, *Nano Letters*, 20, 1, 686–693, 2020. © 2020 American Chemical Society. Further permission requests related to this material should be directed to ACS. With unchanged content from the post-print version, the text, layout and references of this article have been re-formatted in the style of this thesis.

For the work presented here, I conceived and designed the experiments together with H. Schmid. I performed substrate fabrication, MOCVD growth, STEM and PL characterization. I developed a growth model based on the obtained results and wrote the majority of the manuscript.

NANO LETTERS

Cite This: *Nano Lett.* 2020, 20, 686–693

Letter

pubs.acs.org/NanoLett

## Exploring the Size Limitations of Wurtzite III–V Film Growth

Philipp Staudinger,<sup>✉</sup> Kirsten E. Moselund,<sup>✉</sup> and Heinz Schmid<sup>\*✉</sup>

IBM Research - Zürich, Säumerstrasse 4, 8803 Rüschlikon, Switzerland

### Abstract

Metastable crystal phases of abundant semiconductors such as III–Vs, Si or Ge comprise enormous potential to address current limitations in green light-emitting electrical diodes (LEDs) and group IV photonics. At the same time these non-conventional polytypes benefit from the chemical similarity to their stable counterparts, which enables the reuse of established processing technology. One of the main challenges is the very limited availability and the small crystal sizes that have been obtained so far. In this work we explore the limitations of wurtzite (WZ) film epitaxy on the example of InP. We develop a novel method to switch and maintain a metastable phase during a metal-organic vapor phase epitaxy process based on epitaxial lateral overgrowth and compare it with standard selective area epitaxy techniques. We achieve

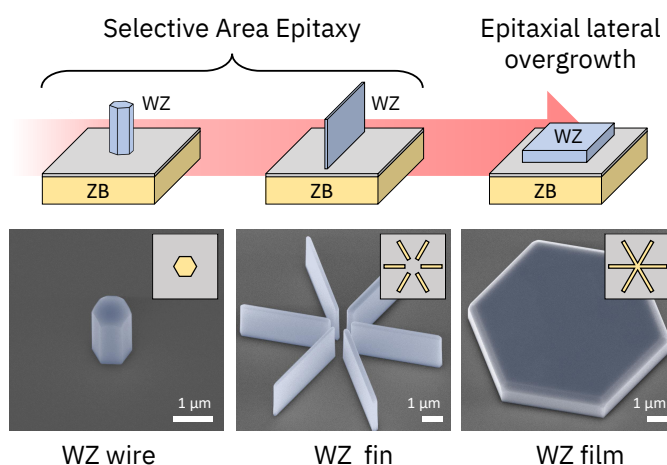


**Figure 5.2** | Table of contents figure.

unprecedented large WZ layer dimensions exceeding  $100\text{ }\mu\text{m}^2$  and prove their phase purity both by optical as well as structural characterization. On the basis of our observations we further develop a nucleation-based model and argue on a fundamental size limitation of WZ film growth. Our findings may pave the way toward crystal phase engineered LEDs for highly efficient lighting and display applications.

### Keywords

crystal structure, wurtzite, indium phosphide (InP), selective area epitaxy (SAE), epitaxial lateral overgrowth (ELO)

### Main Text

Wurtzite (WZ) group III-V (-As/-P) and the closely related Lonsdaleite [37] (LD) group IV semiconductors are currently of high interest because of their potential applications in solid state lighting and on-chip photonics. AlAs, AlSb, AlP, GaP and Ge all possess indirect bandgaps in their bulk-stable cubic phase, whereas both electronic band structure calculations [42, 30, 46, 60] as well as recent experimental reports on nanostructures [98, 109, 316] suggest their band transition to become (pseudo-) direct once their lattice periodicity is changed to the hexagonal WZ or LD symmetry. These findings open new pathways for creating efficient light sources in the important amber-green wavelength region of the visible spectrum where a lack of suitable emitting materials currently limits the performance of LEDs and semiconductor lasers [43, 317]. Direct-bandgap Ge and SiGe compounds on the other hand could even pave the way toward silicon-based optoelectronic devices [318]. Even though research has intensified in recent years, synthesizing these materials in their thermodynamically less stable phase remains challenging. The most explored techniques result in thin nanowires (NWs) and rely on the use of a gold catalyst [77, 70, 286, 134, 319, 78], which hinders technological exploitation. Significant advances were made in the self-catalyzed synthesis of pure WZ InP [320, 311] and GaAs [312, 321] NWs and the catalyst-free selective-area epitaxy (SAE) method, where InP [105] and related ternaries such as AlInP [106] and InGaP [107] NWs have been successfully grown in WZ phase. This recently lead to the development of efficient green NW emitters [106]. Progress in the crystal structure transfer technique in which the stacking of a core NW is transferred to a heteroepitaxially grown shell further allowed for synthesizing a higher range of material systems, including GaP [100], InAs [114], AlGaAs [115], InGaAs [117, 291, 292], AlInP [103], AlGaP [102], Si [141] and SiGe [65]. To explore the rich potential of these new materials, crystal sizes well above  $1\text{ }\mu\text{m}$  are needed to support optical modes and effectively suppress surface recombination. However, it is predicted that the WZ phase becomes unstable above a critical diameter, which is in the range of only a few tens of nanometers [264]. Several demonstrations have surpassed these limitations which resulted in WZ InP [169, 268] and InGaAs [31] NWs with diameters up to several hundreds of nanometers, even though the mechanisms involved are not well understood yet. Other efforts include the merging of arrays of laterally overgrown WZ NWs [194]. In that case, phase transformation

due to misaligned stacking sequences prevents the formation of WZ layers and a mixture of crystal structures is obtained. The Fukui group succeeded in transferring the WZ stacking sequence from a GaN substrate to AlInP along the  $\langle 1\bar{1}00 \rangle$  direction, which however faces fundamental limitations due to the large lattice mismatch and the resulting high density of stacking faults [109]. By growing fin structures vertically [108] or films laterally with the use of template-assisted selective epitaxy [303, 304, 302, 254] the growth facet is kept small, which can help to promote the formation of larger layers of metastable material. However, the former technique is lacking a planar geometry as desired for many device applications and in the second example significant microfabrication processes are needed. Independent of the applied epitaxy techniques, a general understanding of the size limitations and mechanisms that prevent the fabrication of large WZ III-V layers is missing.

In this work, we investigate techniques to scale WZ film growth to larger dimensions and experimentally explore their size limitations. InP is particularly suited for this comparative analysis as both the WZ and zinc-blende (ZB) phases exhibit a direct, but distinctive bandgap, which facilitates an optical analysis. Starting from standard SAE nanowires and fins on top of patterned InP (111)A substrates, we develop a novel method which relies on the enforced epitaxial lateral overgrowth of interconnected fins by creating so-called zipper points. We report on pure WZ layers on insulator exceeding areas of  $100 \mu\text{m}^2$ , which can be grown in dense arrays ideal for micro-LED integration [322]. The grown material is analyzed by high-resolution scanning transmission electron microscopy (HR-STEM), atomic force microscopy (AFM) and micro-photoluminescence ( $\mu$ -PL). By modifying the mask layout toward larger dimensions we establish an upper size limit for growth of WZ films, which is consistent for all techniques investigated in this study. A general model based on nucleation mechanisms is developed to explain our present and former observations.

Growth is carried out using patterned  $\text{SiO}_2$  covered InP(111)A substrates with reactor conditions optimized for WZ formation (see **Methods** for details on this process). In a first experiment we explore epitaxy from hexagonal holes. The sidewalls of the holes are aligned with the  $\{112\}$  ZB orientations to support the  $\{1\bar{1}00\}$  low energy WZ facets [323]. As shown in the SEM images of Figure 5.3(a), growth along the ZB  $\langle 111 \rangle$  or WZ  $\langle 0001 \rangle$  direction dominates and vertical wires are formed. An immediate extension of this technique is to reduce the spacing in-between individual holes along a specific direction until they are merged together – a pattern of straight lines. We explore growth from such a selective mask with nominal line widths of 50 nm, similar to N. Wang et al. [108]. As shown in Figure 5.3(b), 2D fins are formed after growth which again are bounded by straight  $\{1\bar{1}00\}$  sidewalls, suggesting the formation of WZ phase.

The structural stability of fin structures intuitively suggests to just overgrow and coalescent parallel fins into a larger structure. However, it is well known that merging of individual growth fronts will lead to detrimental dislocation defects and was therefore not considered. In contrast, dislocation formation can be avoided by controlling the coalescence front in a zipper growth mode using a common growth origin [237, 239]. Combining our robust fin epitaxy

with a zipper-like growth should accordingly allow the defect-free merging of structures. If we pattern our fin design such that lines of the 3 equivalent orientations intersect, we can intentionally create concave edges at the merging points, inducing zippers as described in the schematic of Figure 5.3(c) and in more detail in Figure 5.9. We expect these edges to be unstable during growth, since every small nucleus creates a facet with a growth rate much higher than for the  $\{1\bar{1}00\}$  sidewalls of the fins. This results in radial growth from the central point until stable edges are formed again. Importantly, we expect the WZ crystal structure of the fin to be transferred along this lateral growth direction. As can be seen in Figure 5.3(c) we in fact obtain a full hexagon which is enclosed in  $\{1\bar{1}00\}$  facets instead of a star formed from fins. Hence, we triggered a zipper induced epitaxial lateral overgrowth (zipper-ELO), which compared to conventional ELO is well controlled by the geometry of the structure. Remarkably, even though individual fins show negligible lateral growth rate, efficient ELO could be enforced by arranging the fins in a star configuration and thus inducing a zipper growth mode.

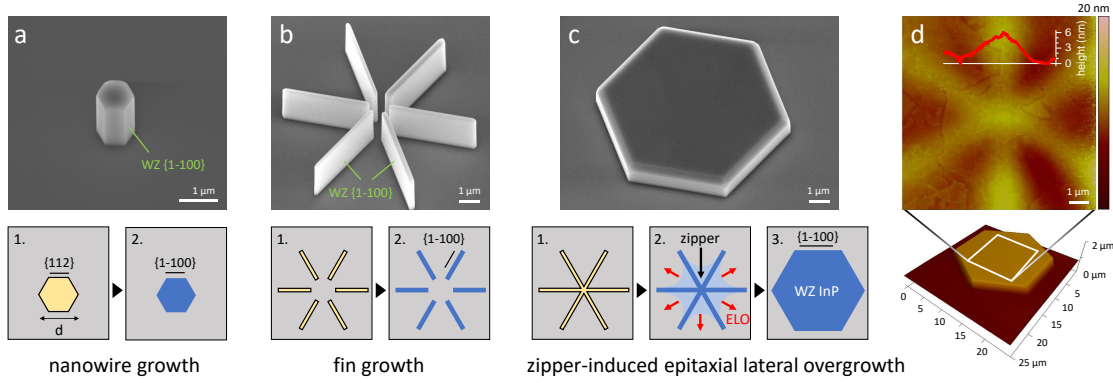


**Figure 5.3** | From nanowire to film growth for large area WZ structures. Representative 30° tilted SEM view of (a) an InP nanowire, (b) InP fins arranged along all equivalent  $\langle 110 \rangle$  directions on top of an (111)A substrate showing pronounced  $\{1\bar{1}00\}$  sidewall facets, and (c) same arrangement but with fins connected in the center. The 6 concave zipper edges that emerge close to the center are not stable during growth and continue to grow until the enclosing  $\{1\bar{1}00\}$  facets are reached, and a hexagon is formed as schematically shown on the bottom. (d) AFM characterization of a 20  $\mu\text{m}$  zipper-ELO hexagon overgrown for 60 min. The star pattern from the substrate is still visible, indicating a fin-dominated zipper growth mode. Bottom shows investigated area on a 3D overview image.

In this technique fin-growth is expected to dominate the epitaxy during the entire deposition process and only as a consequence the spaces in-between the fins are filled by fast growth of high index planes. In support we carried out atomic force microscopy (AFM) on top of a 20  $\mu\text{m}$  wide zipper-ELO hexagon (Figure 5.3(d)). Even though SEM characterization suggests a flat top surface, the underlying star pattern can still be observed on top of the 1  $\mu\text{m}$  high hexagon which shows a remaining fin height of around 5 nm. Also visible are rounded facets and surface defects which we attribute to InP desorption during the cool-down step. Our observations indicate that fin-growth dominates and stabilizes the formation of the WZ phase during zipper-ELO.

The crystal structure of the hexagon is assessed by STEM investigation. We prepare a FIB lamella of the hexagon close to the center, such that the viewing direction is along the  $\langle 110 \rangle$  ZB or the  $\langle 11\bar{2}0 \rangle$  WZ direction. The high angle annular dark field (HAADF) overview image is shown in Figure 5.4(a). At the center (marked in blue) the central mask opening is indicated. Nearby on either side, an intensity variation in the  $\text{SiO}_2$  mask is noticeable due to other mask lines crossing in a diagonal. A high-resolution-HAADF image in Figure 5.4(b) shows the transition from the ZB phase in the substrate to the WZ phase in the grown plate, which occurs while the crystal is confined within the narrow oxide lines. The fast Fourier transform (FFT) pattern on three different spots along the growing direction support this observation. Every other spot investigated in the hexagon shows pure WZ phase, as exemplified in Figure 5.4(c), which depicts a high-resolution-HAADF image together with an FFT pattern on one exterior of the crystal. Complementary PL analysis of another sample is shown in Figure 5.4(d)-(f). Figure 5.4(d) depicts 225 room temperature  $\mu$ -PL emission spectra of a 2D scan. The scan was carried out across a  $15 \times 15 \mu\text{m}^2$  area with a spatial resolution of  $1/\mu\text{m}^2$  at a laser wavelength of 633 nm and a spot size below  $1 \mu\text{m}^2$ . Two distinct emission peaks are visible which can be well correlated with the band gap energies of ZB (1.34 eV) and WZ (1.41 eV) InP, respectively. Some measurements show both peaks, which is attributed to the emission from both the grown WZ structure and the underlying ZB substrate. The comparable line width and amplitude of the emission peaks further suggest excellent optical properties. Figure 5.4(e) and (f) show the

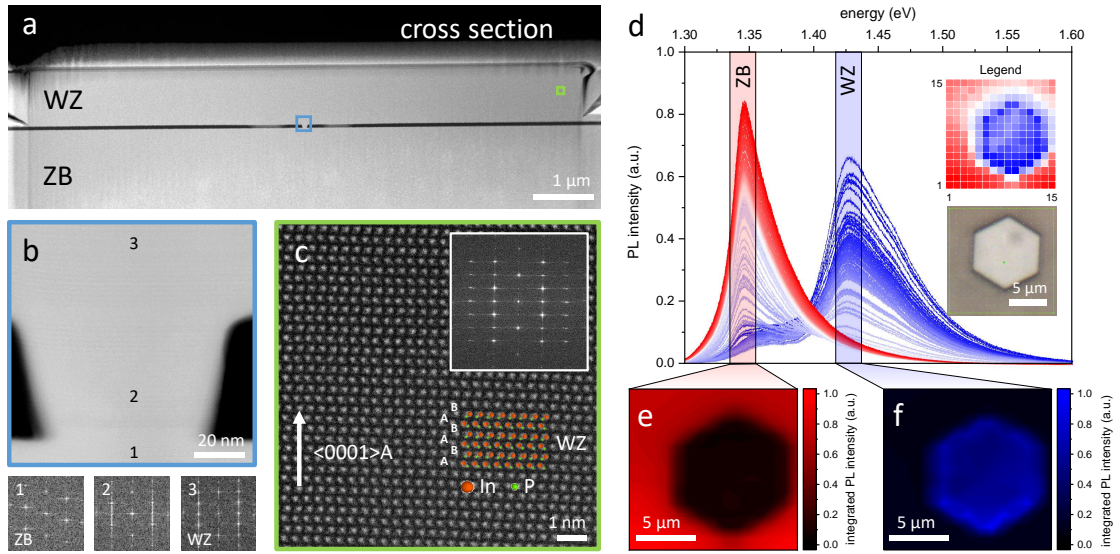


**Figure 5.4** | HAADF-STEM and PL characterization of a zipper-ELO hexagon. (a) FIB cross section of a  $1 \mu\text{m}$  thick and  $10 \mu\text{m}$  wide hexagon with the central mask opening visible. (b) High-resolution image at the central opening together with FFT-patterns from three positions that show the ZB  $\rightarrow$  WZ transition. (c) High-resolution image and FFT pattern close to the edge of the crystal showing WZ type ABAB.. stacking. (d) 2D room-temperature PL scan with  $15 \times 15$  measurements. Color in legend shows spectrum position corresponding to the microscope image below. Order of colors has been chosen to create smooth gradients from highest to lowest emission for both peaks. (e, f) Integrated PL intensity around (b) the ZB and (c) the WZ emission peak for each measurement. A clear phase transition is observed for the entire hexagon.

integrated intensities around the two distinct peak energies for every measurement point, indicating high phase purity in agreement with the STEM data.

Next, we explore the scaling behavior of the different structures investigated in this study. Growth from hexagonal holes with increasing diameter is shown in Figure 5.5(a). NWs are formed in small holes while decreased height is observed in openings with larger diameter, causing the formation of low aspect-ratio plate-like structures. This can be well explained with the change in precursor supply from the surrounding oxide [293]. Clear hexagonal faceting further suggests the formation of WZ phase up to crystal sizes of around 5  $\mu\text{m}$  [308], while inclined 3-fold symmetrical tetrahedron-like facets in the case of 20  $\mu\text{m}$  is a signature of the ZB structure [324]. More statistics can be found in Figure 5.8. Straight line patterns with increasing length up to 0.5 mm are investigated next. Whereas in the case of holes the diameter was limited to around 10  $\mu\text{m}$ , here no such obvious restriction can be seen. Clear  $\{1\bar{1}00\}$  sidewalls are obtained up to the longest fins grown in this study, however due to angular lithography misalignment, longer fins tend to become wider than short ones as is detailed in Figure 5.10. Concerning structural characterization, we do find segments with crystal phase mixing in long fins (0.3 mm), with WZ remaining the dominant phase (Figure 5.11). The surprising structural stability of fins even approaching macroscopic dimensions suggests the possibility to grow large layers with our zipper-ELO technique. To test this hypothesis, we pattern star-shaped holes with varying size and grow structures for 30 min using our standard recipe. Figure 5.5(c) shows that in this case full hexagons are obtained for star diameters up to 10  $\mu\text{m}$ , whereas larger structures do not fully develop the enclosing  $\{1\bar{1}00\}$  boundaries yet but show intermediate  $\{11\bar{2}0\}$  facets and thus remain incomplete in most cases. Experiments with extended growth durations allow for the reliable formation of zipper-ELO hexagons with 20  $\mu\text{m}$  diameter as shown in Figure 5.7. This demonstrates that growing larger hexagons is conceptually feasible but comes at an increased expense due to the exceeding growth time and precursor consumption. Consequently, we evaluate an extension of this process based on tiling individual star-mask openings as shown in Figure 5.5(d). Growing this grid-layout should result in continuous films applicable to wafer scale areas while keeping the same limited growth time. Initially, looking at the grown test structures indicates the feasibility of this approach, with the structures following the given mask layout. However, closer inspection reveals that facets belonging to the hexagonal symmetry formed for smaller structures whereas in the case of 25  $\mu\text{m}$ , the appearance of inclined  $\{111\}$  facets clearly suggest the formation of ZB phase similar to SAE from large holes (Figure 5.5(a)). This experimental finding points toward a fundamental size limitation of the WZ InP epitaxy process, which will be discussed below. To obtain a virtually continuous film of WZ InP with larger dimensions we propose to pattern zipper-ELO structures closely together but avoiding coalescence as shown in Figure 5.5(e).

In the view of our observations we develop a nucleation-based model as sketched in Figure 5.6(a). It is known from VLS and assumed in SAE that NWs tend to grow in a layer-by-layer fashion [74, 73]. This essentially means that a nucleus of critical size is randomly formed at the surface and subsequently expands quickly to fill up the entire area virtually defect-free. This is true for small growth surfaces. However, as the dimension of layers increases, the probability

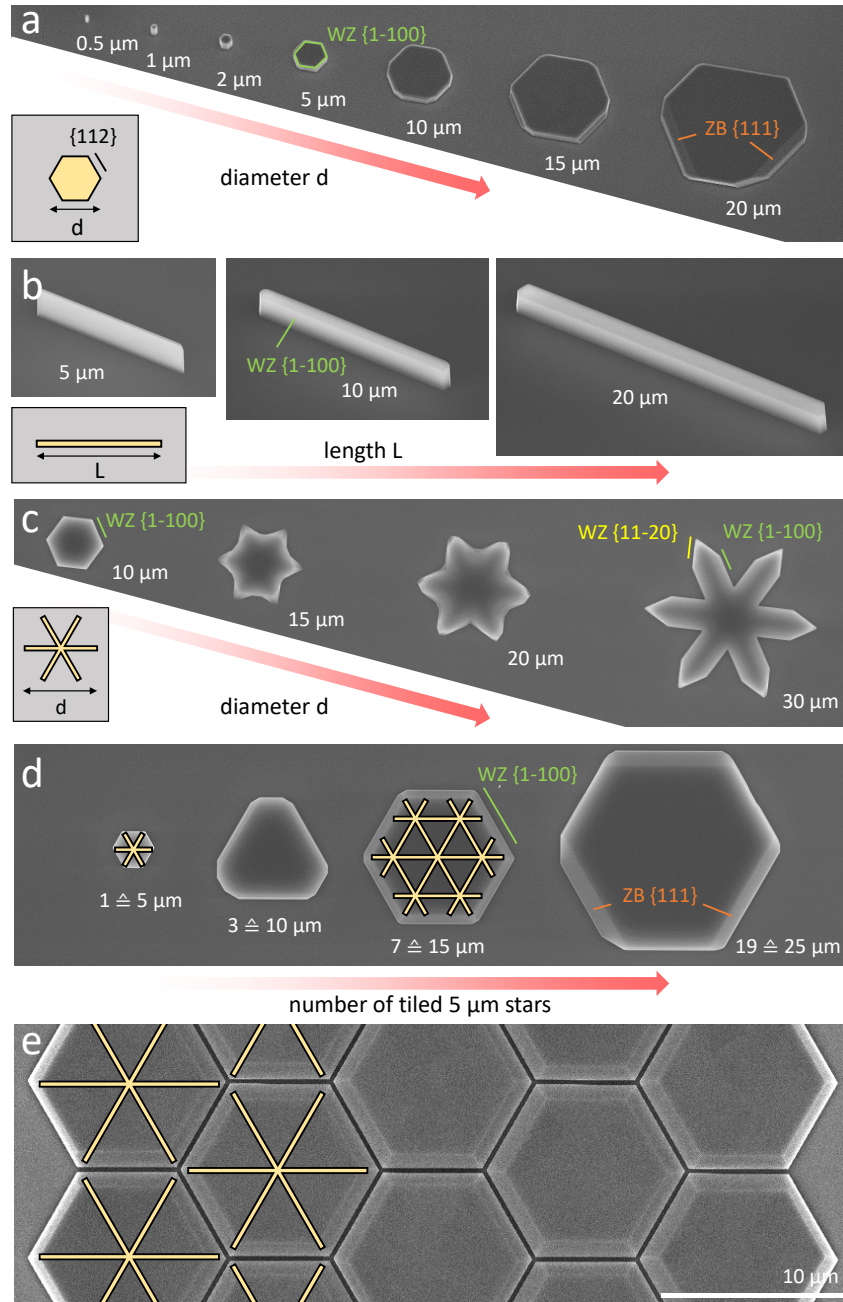


**Figure 5.5** | Scaling behavior of InP structures. Representative 30° tilted SEM view of (a) InP crystals grown in hexagonal holes with increasing diameter and (b) InP fins with  $\{1\bar{1}00\}$  sidewalls and increasing length. Faceting reveals a WZ  $\rightarrow$  ZB transition between a diameter of 15 and 20  $\mu\text{m}$  for holes while no such effect is seen for fins up to 0.5 mm in length (Figure 5.10). Representative top view SEM images of 30 min overgrown (c) star-openings with increasing size and (d) grid-openings with increasing number of tiled star-openings. In the first case the occurrence of the  $\{11\bar{2}0\}$  facets significantly slows down the formation of full hexagons above a certain size, while in the second case WZ  $\rightarrow$  ZB transition is observed similar to crystals grown from holes, indicating a fundamental limit in InP (0001) epitaxy. (e) In order to obtain arbitrarily large areas of WZ InP, we propose to pack hexagons from zipper-ELO closely together. The resulting gaps can be considered during following device processing or further minimized by careful engineering.

of two independent nuclei reaching critical size before they merge increases significantly and growth of a defective film is expected [325]. We therefore distinguish two distinct regimes in Figure 5.6(a). As long as the growth area is small and the conditions are such that ABAB.. stacking is favored we expect pure WZ to be grown in our structures, because every layer is nucleated from a single nucleus. We define this as case A. If the dimensions are increased, we assume defects to be formed because of unavoidable monolayer steps in the substrate and the merging of independent nuclei. Such imperfections can result in localized dislocations [325] or vertical antiphase boundaries as sketched in Figure 5.6(a). Antiphase boundaries are expected to have a high defect energy which is proportional to the area of the respective plane. Hence, we assume that these kind of defects only remain stable for the growth of thin fins (case B). In broader structures where the defect plane is much larger another process is triggered. Here, the merging of mismatched layers induces a propagation of the defect line toward the exterior of the crystal. In such a case the formation of the thermodynamically more stable ZB phase is expected (case C) as described previously for the merging of NWs by D. Jacobsson et al. [194].

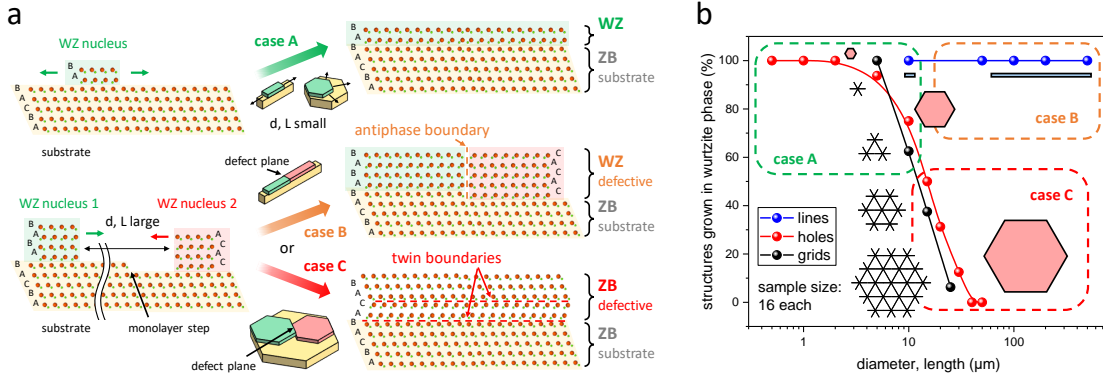


**Figure 5.6** | (a) Atomistic model for size-dependent structural transitions in III-V SAE. If the structure size is small, every layer is started from a single nucleus or competing nuclei merge before they reach a critical size and pure WZ material can be obtained under the right growth conditions (case A). In the case of large growth planes, competing nuclei with mismatched stacking order can merge after they reach critical size, in which case two scenarios can occur: A defect plane is formed in the crystal, while it remains WZ (case B) or the defect propagates through one of the nuclei which changes the stacking to cubic ZB with twins and stacking faults (case C) [194]. The latter scenario is expected to occur in case of high defect energy, that is, when the defect plane area is large. (b) Experimental validation of our model through statistical analysis of crystals grown during the same growth run from line (blue), hole (red) and grid (black) openings as a function of feature size in semilogarithmic scale. Solid lines are a guide for the eye. Drawings schematically show the seed from which respective structures were grown. Crystal phase is determined by  $\mu$ -PL analysis. Nearly 100% of structures with feature sizes below 10  $\mu\text{m}$  show WZ PL emission, indicating primarily occurrence of case A. Fin structures grown from lines remain WZ independent of length. We speculate that the defect energy in this case is too small to induce a gliding of the planes  $\rightarrow$  dominated by case B. Both hole and grid structures above 10  $\mu\text{m}$  in size show ZB emission in most cases, indicating the crystal phase has been transformed. This is expected in our model due to the large defect plane area as described in case C.

To test our model, we use PL to statistically analyze the crystal phase obtained in our structures. The PL-emission spectra of 304 measurements is analyzed; if a distinct peak at the WZ position is visible, we categorize them as WZ, otherwise they are ZB. It should be noted that all crystals

that possessed 3-fold tetrahedral symmetry during SEM analysis, as, for example, the 20  $\mu\text{m}$  sized structure in Figure 5.5(a), have no WZ peak, whereas for the remaining structures the crystal phase cannot be unambiguously assessed from their morphology. In Figure 5.6(b) we show the percentage of crystals that show WZ phase for line, hole and grid seeds in dependence of their dimension. For small diameters and lengths all investigated structures show WZ phase, which is in agreement with our model (case A) and previous observations in NWs [268]. Next, we look at fin structures with lengths ranging from 5  $\mu\text{m}$  to 0.5 mm (blue). In that case, all PL measurements show the WZ peak, even though the dimensions of the longest fins exceed the critical length and nucleation from multiple seeds can be expected. Thus, we conclude that the defect plane energy of antiphase boundaries is too small to trigger a gliding process and case B is obtained primarily, but not exclusively. Indeed, we find extended sequences of crystal intermixing in long fins (0.3 mm), with WZ remaining the dominant phase (Figure 5.11). On the other hand, for hole and grid openings we obtain a change to ZB phase for larger diameters, which is predicted by our model due to the high defect energy at the antiphase boundary and the resulting plane gliding (case C). We expect a similar phase transition for single zipper-ELO structures once they exceed a certain size, however we excluded them from this diagram, because they do not develop to full hexagons under investigated growth duration (30 min).

Our suggested model extends existing models based on mononucleation [326, 265] and essentially combines two previous observations: defect-formation under the condition of multiple nucleation sites [325] and phase transformation in merged WZ structures which are stacking-misaligned and exceed certain dimensions [194]. The former model was developed for VLS growth and predicted only nonradiative step facets to be formed due to the small dimensions investigated. The latter observation concerned the radial merging of previously grown vertical NWs. We claim that this mechanism is not only valid for macroscopic structures nucleated from different sites on the same substrate but is also obtained for epitaxy on a single facet if it exceeds critical dimensions. We speculate that this mechanism is the primary cause for the size limitation of WZ films and more generally any metastable material phase formed along a stacking direction. Confining the growth area in one dimension prevents the phase transformation to the thermodynamically more favored crystal structure by keeping the defect energy small, which was utilized in this and other [108] studies to grow fins with large dimensions or films with the usage of a template [303]. The expansion of such fins laterally however increases the defect area and triggers a gliding of crystal planes to the ZB phase as was observed for the grid structures. We believe that this model is general for both catalyst-free as well as VLS techniques and can be applied to a wide range of materials.

In conclusion, we experimentally determined the limitations for WZ film growth using the example of InP. Pure WZ structures of 20  $\mu\text{m}$  diameter were obtained by a newly developed zipper-ELO which is based on WZ fins. Even though individual fins showed negligible lateral growth rate, efficient ELO could be enforced by arranging the fins in a star configuration which induced lateral growth in the concave center corners of the star. In addition, most of the structure covers an underlying insulating oxide, which can be interesting for implementing

electronic and optical devices. As was revealed in this study, individual hexagons or tiled arrangements cannot be grown infinitely large without going through a phase transition to a thermodynamically more stable crystalline phase, independent of the growth conditions. However, by arranging hexagons closely spaced on a substrate a virtually continuous WZ film can be obtained with arbitrary dimensions. On the basis of our findings, we developed a generalized nucleation-based model to explain our observations, which is in accordance with previous findings. The combination of fin structures which may support a phase change and the creation of a zipper to force ELO could find interesting applications in material synthesis, heterointegration and device fabrication.

### Methods

**Growth.** A standard InP(111)A wafer was covered with 60 nm plasma-enhanced chemical vapor deposited (PECVD) SiO<sub>2</sub>. Hexagonal openings with varying diameter and line seeds with nominal widths of 50 nm were patterned along the 3 equivalent  $\langle 110 \rangle$ -directions by e-beam lithography (EBL) and reactive ion etching (RIE) in a CHF<sub>3</sub>/O<sub>2</sub> plasma. InP growth was performed in a cold-wall showerhead MOCVD reactor using tertiarybutylphosphine (TBP) and trimethylindium (TMIn) at a total pressure of 60 torr. Partial pressures for TBP and TMIn were kept at 8.2 Pa and 82 mPa, respectively to achieve a nominal V/III ratio of 100. Upon loading, the reactor was heated to 630°C in a TBP atmosphere, and growth was initiated subsequently by introducing TMIn. Reactor temperature was ramped up within the first 60 s to 640°C, the final growth temperature. This procedure was developed in order to prevent substrate desorption prior the nucleation process. Deposition time was 30 min if not stated otherwise. After growth, substrates were cooled under a TBP atmosphere until reaching a temperature below 400°C.

**Characterization.** The morphology of InP nanostructures and films was characterized using a Hitachi SU8000 SEM and a Veeco Instruments AFM with a NanoScope V controller. The structural quality of individual films was investigated by STEM along the  $\langle 110 \rangle$  and  $\langle 11\bar{2}0 \rangle$  zone axis for ZB and WZ, respectively. The sample lamellas were prepared by means of a FEI Helios Nanolab 450S focused ion beam. HAADF micrographs were generated using a double spherical aberration-corrected JEOL JEM-ARM200F microscope operated at 200 kV. For optical characterization, a continuous laser source at 633 nm was used to excite the InP layers in ambient conditions. Excitation as well as collection of the photoluminescent response was facilitated from the top using a 50× objective which was linked to a Peltier cooled Si CCD detector from Horiba Scientific.

### Acknowledgments

The authors gratefully acknowledge Antonis Olziersky, Steffen Reidt, Marilyne Sousa, Emanuel Lörtscher, Anna Fontcuberta i Morral and Heike Riel. The work presented here has received funding from the European Union H2020 program SiLAS (Grant Agreement No. 735008) and

the Swiss National Science Foundation under Project Number 200021\_156746.

## 5.2 Additional Results

The following figures have been published (in different order) as supporting information along with the publication presented in the previous section from where they are referenced. Descriptions are given in the corresponding figure captions.

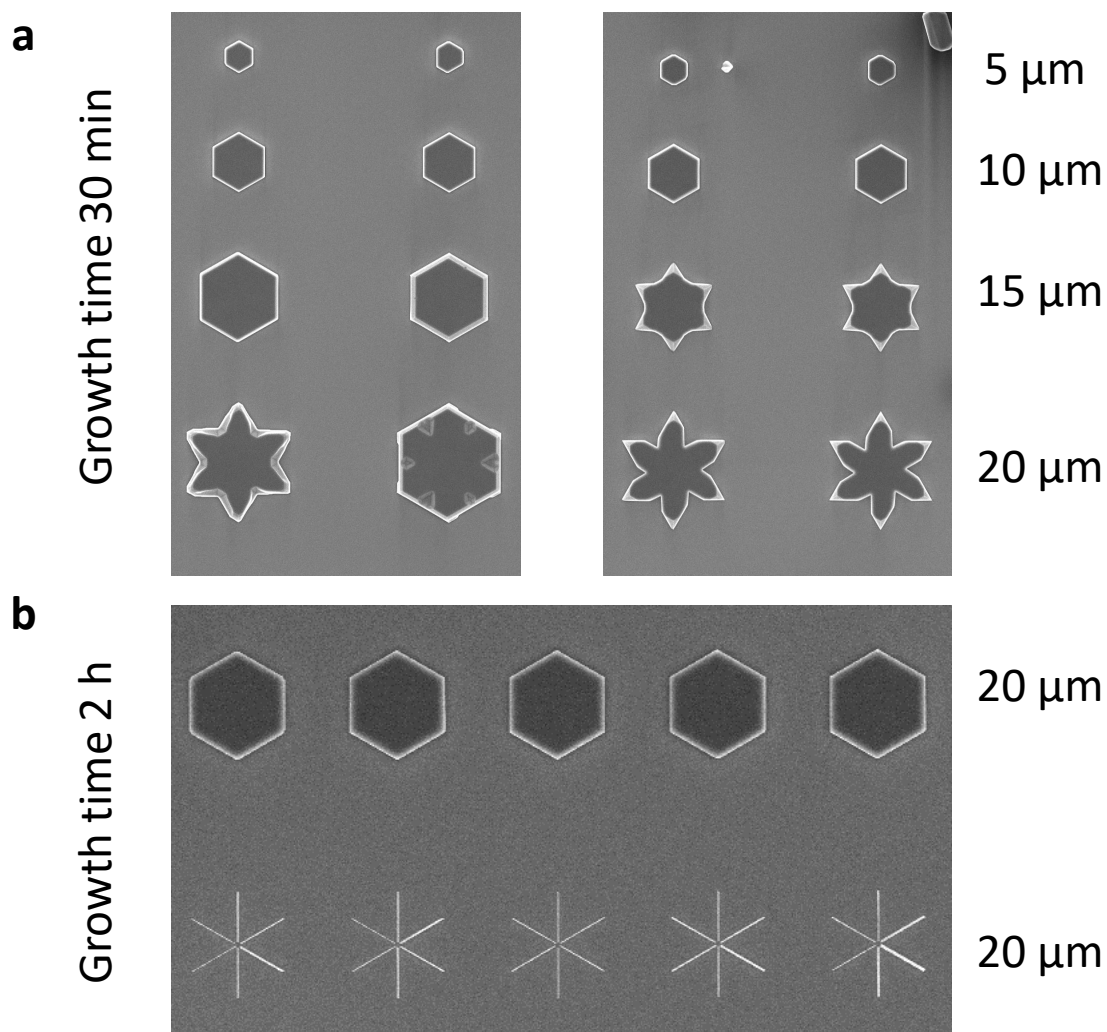


**Figure 5.7** | (a) SEM images of zipper-ELO structures grown for 30 min with increasing diameter to show growth statistics. The largest fully-grown hexagons are obtained for a diameter of 15  $\mu\text{m}$ . Incomplete hexagons show rich and diverse faceting. (b) In contrast, after 2 h of growth time we obtain a yield of fully-grown 20  $\mu\text{m}$  hexagons of close to 100%. Star structures without connected central point show pure fin-growth also after prolonged growth runs (bottom).

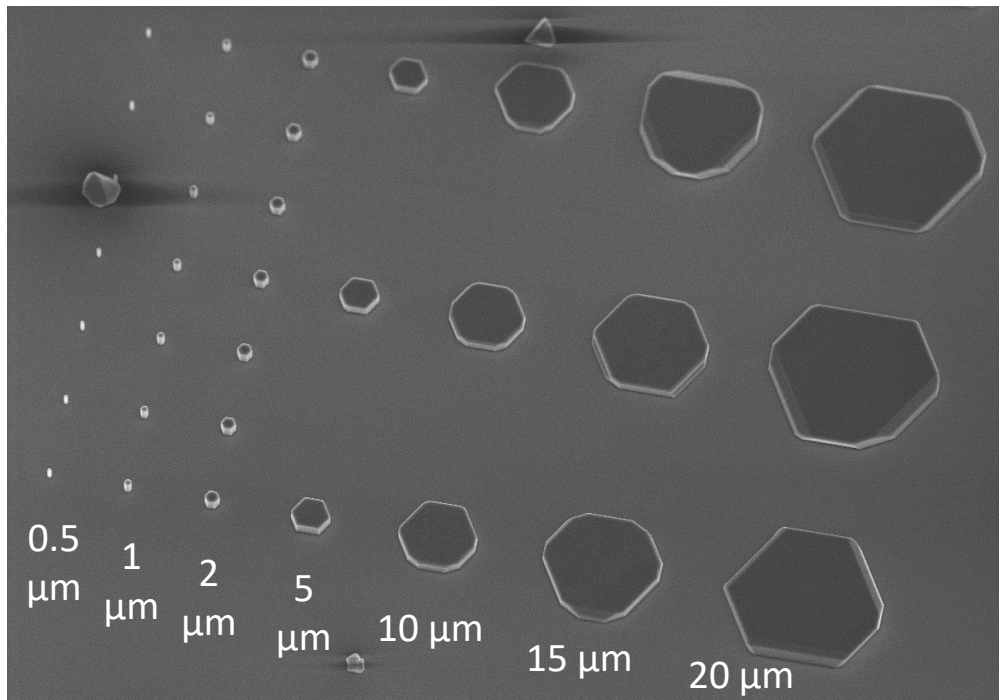


**Figure 5.8** | 30° tilted SEM images of InP crystals grown in hexagonal holes with increasing diameter to show typical distribution of growth morphologies. Hexagonal symmetry dominates until a diameter of 5  $\mu\text{m}$ . Above, more complex faceting appears, and the formation of tetrahedral structures is observed in many cases. Apart from the intentionally grown structures, additional polycrystals are observed on some spots, which we attribute to dirt particles that were present on the sample already before the deposition.

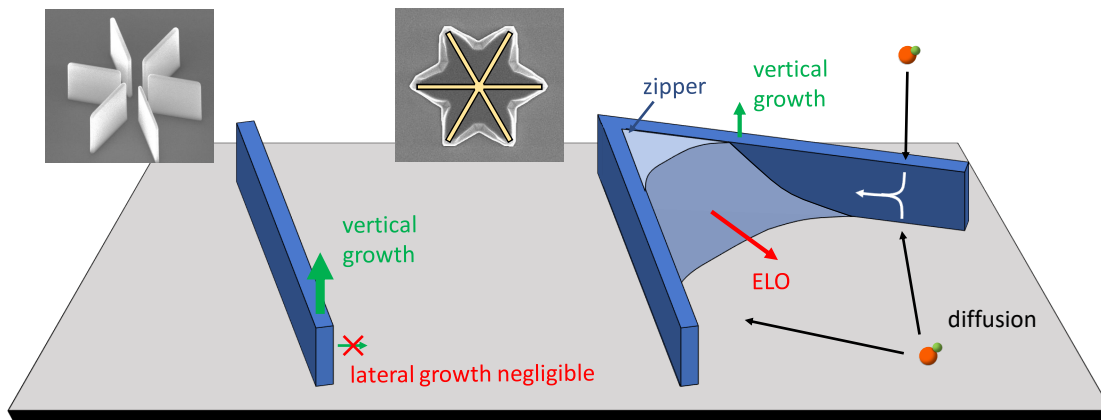


**Figure 5.9** | 3D schematic of zipper-ELO. Vertical growth is facilitated by fin-growth, which by itself shows negligible lateral growth. An arrangement of intersecting fins however allows for inducing zipper points, which trigger an ELO to fill up the layer until stable facets are formed again. The metastable crystal phase is transferred from the fins into the layer. Surface diffusion of the growth species on the  $\text{SiO}_2$  mask as well as the fin facets results in high lateral growth rate.

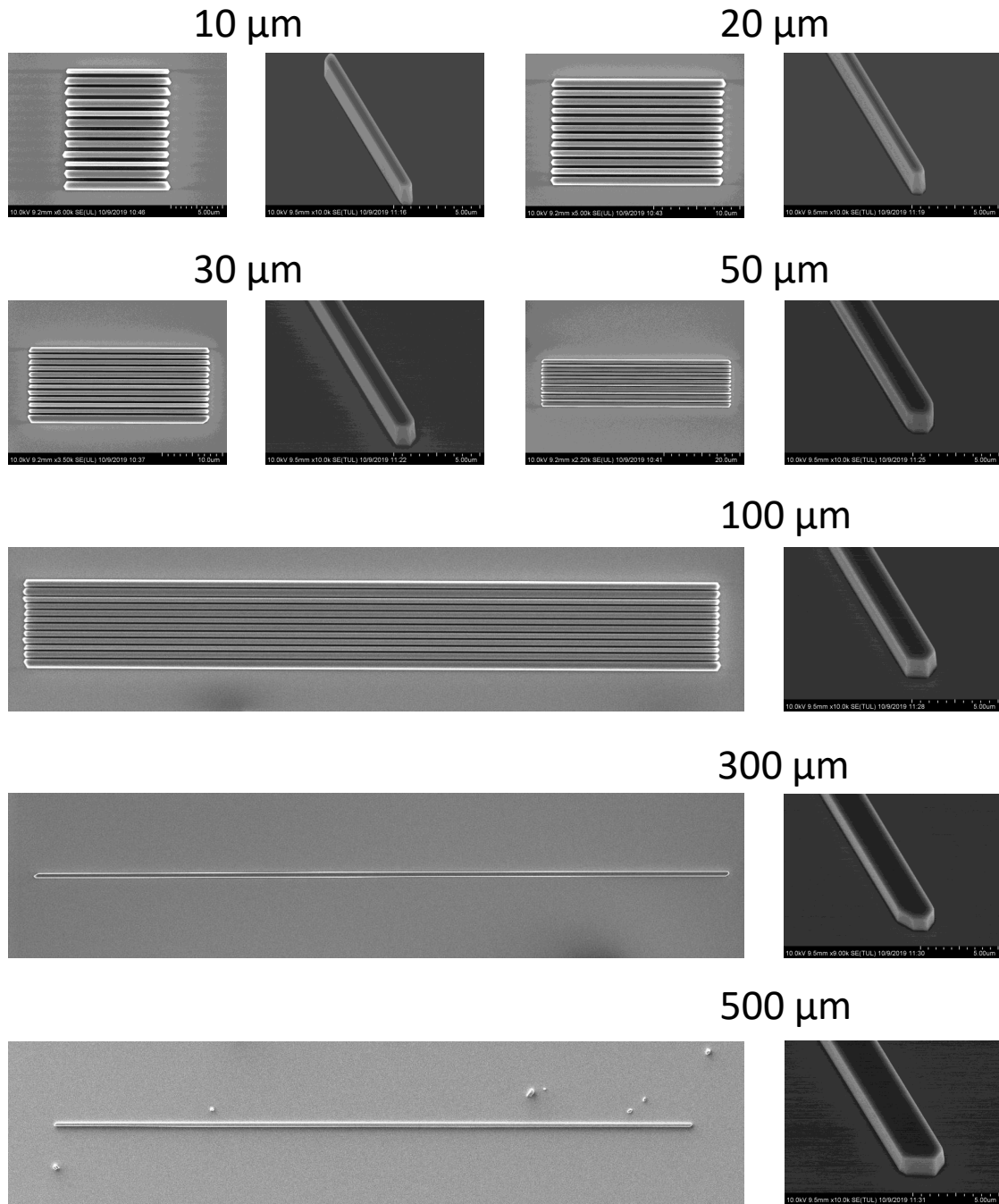


**Figure 5.10** | SEM images of InP fins with increasing length showing both overview images as well as details with equal magnification for every fin. For the 0.5 mm fin the low-magnification mode of the SEM was used in order to fit the entire crystal. The broadening of longer fins is clearly visible, which originates from the angular misalignment of the e-beam lithography. Straight  $\{1\bar{1}00\}$ -plane side-wall facets suggest the formation of WZ crystal phase, in contrast to the richer faceting obtained in the case of large hexagonal holes (Figure 5.8).

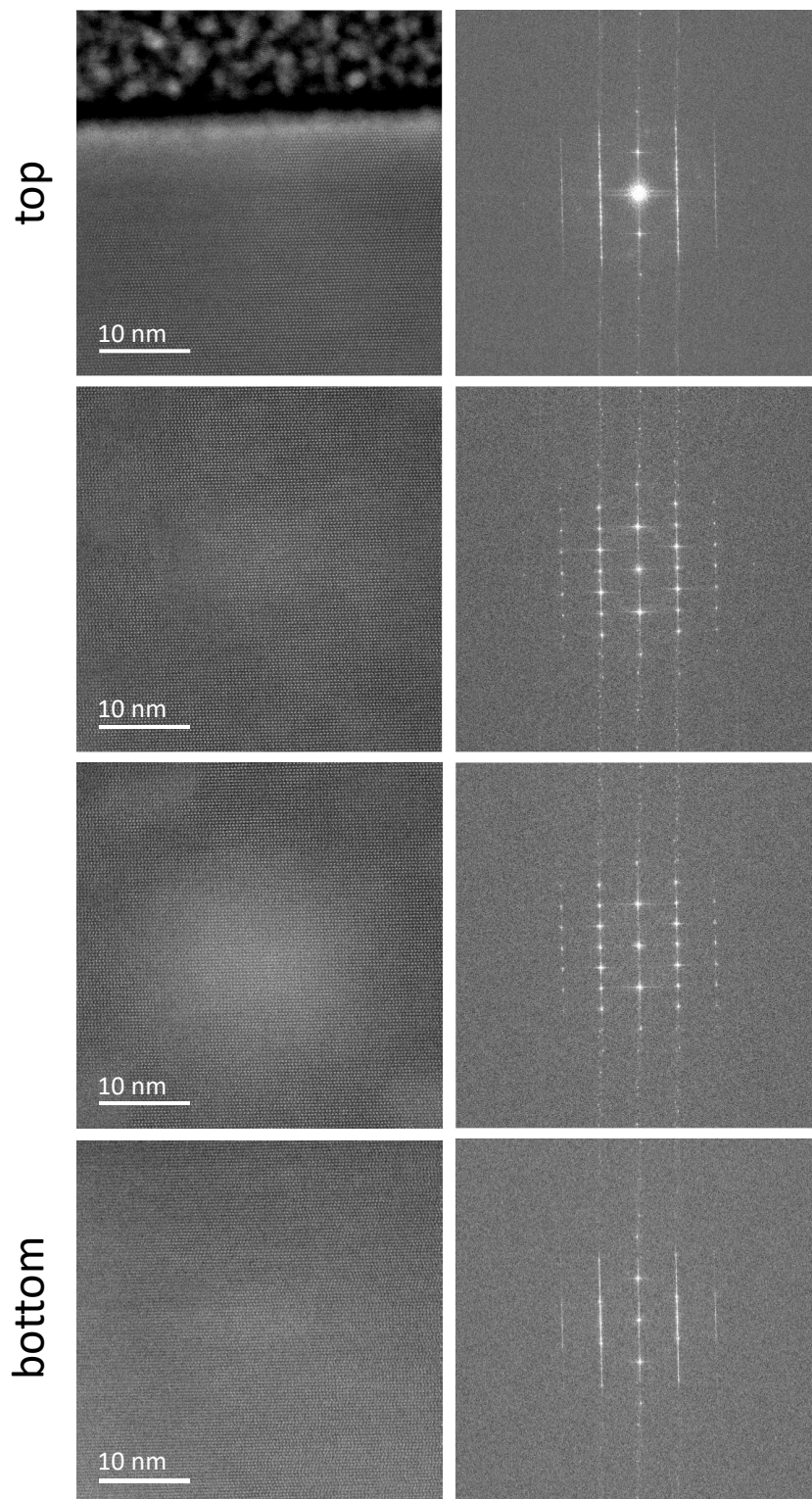


**Figure 5.11** | STEM characterization of an InP fin with 300 μm length from four different positions (bottom to top). Areas with pure WZ material and crystal phase intermixing were found. This is in contrast to observations on shorter fins or zipper-ELO structures where only pure WZ was found (Figure 5.4).

## 5.3 Main Achievements

In summary the following results have been obtained in this chapter:

- We developed a methodology to enforce epitaxial lateral overgrowth from metastable fins, which transfers the crystal phase into a layer.
- This was demonstrated for WZ InP layers, but might be applicable to other material systems.
- We explored size limitations of film growth using several related techniques.
- Metastable films larger than  $100\text{ }\mu\text{m}^2$  could be achieved with high phase purity and crystal quality, the largest ever demonstrated.
- A fundamental size limitation was found and explained by a nucleation-based model.
- Larger layers can be obtained by tiling individual segments in close proximity.
- In an invited contribution to the Compound Semiconductor Magazine we present an overview of our results on *crystal phase engineering*.



## 6 Room Temperature Lasing from Wurtzite InP Microdisks

Zipper-ELO allows for the growth of crystals with large spatial footprint and aspect ratio, and is therefore useful for the epitaxy of metastable films. Another advantage of this technique is that it allows for lithographically precise positioning of as-grown nano- and micro-structures. The dimensions and geometries of the crystals are well controlled and at the same time largely separated from the substrate, as this is a lateral overgrowth technique. By progressively increasing the oxide thickness, we explore the possibility to create structures that are optically isolated, and can serve as basis for advanced photonic structures.

In this chapter, we present our latest results based on WZ InP crystals. Our main findings are currently under review and will be shown in the following section.

### 6.1 Publication 3 | Wurtzite InP Microdisks: from Epitaxy to Room-Temperature Lasing

In this article we develop a versatile photonic platform using zipper-ELO. We explore the synthesis of optically isolated nano- and micro-structures in metastable phase, and demonstrate high control on the shape, position and dimensions of individual crystals. This allows for the direct growth of periodic arrays or more advanced arrangements of closely positioned disks and related geometries. Such an approach could be highly interesting for designing photonic crystals or coupled laser arrays. We demonstrate the capabilities of our platform by showing room-temperature lasing from WZ InP microdisks.

The following article presents the pre-print version of the manuscript published on arXiv.org. For the work presented here, I performed the majority of experiments, including substrate fabrication, MOCVD growth and STEM characterization. I conceived the epitaxy experiments and wrote the majority of the manuscript.

### Wurtzite InP Microdisks: from Epitaxy to Room-Temperature Lasing

*Philipp Staudinger, Svenja Mauthe, Noelia Vico Triviño, Steffen Reidt, Kirsten E. Moselund, and Heinz Schmid*

IBM Research - Zürich, Säumerstrasse 4, 8803 Rüschlikon, Switzerland

#### Abstract

Metastable wurtzite crystal phases of semiconductors comprise enormous potential for high-performance electro-optical devices, owed to their extended tunable direct band gap range. However, synthesizing these materials in good quality and beyond nanowire size constraints has remained elusive. In this work, the epitaxy of wurtzite InP microdisks and related geometries on insulator for optical applications is explored. This is achieved by an elaborate combination of selective area growth of fins and a zipper-induced epitaxial lateral overgrowth, which enables co-integration of diversely shaped crystals at precise position. The grown material possesses high phase purity and excellent optical quality characterized by STEM and  $\mu$ -PL. Optically pumped lasing at room temperature is achieved in microdisks with a lasing threshold of  $365 \mu\text{J}/\text{cm}^2$ , thus demonstrating promise for a wide range of photonic applications.

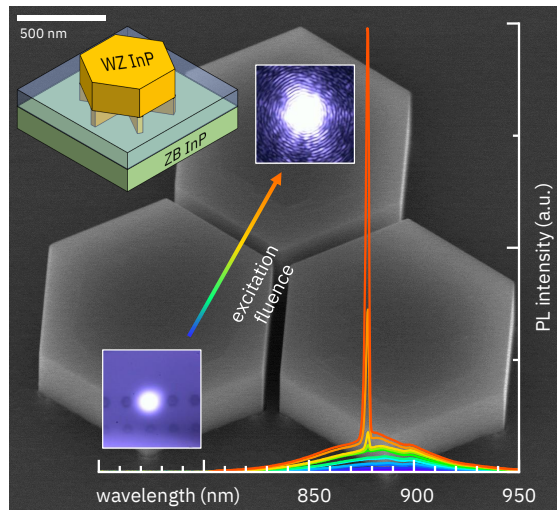


**Figure 6.1** | Table of contents figure.

#### Keywords

Indium Phosphide, III-V, wurtzite, microdisk, room-temperature lasing

#### Main Text

III-V materials have attracted great interest throughout the past decades, due to their unique optical and electronic properties. The direct and tunable bandgap allows for scaled electro-optical devices with efficient emission and absorption properties. Novel concepts like on-chip optical communication [327], complex optical networks [328], topological photonics [329], or metasurfaces [330] have been proposed and rely on the unique features of scaled III-V devices such as microdisk lasers [256] or photonic crystals [331]. Using a top down approach based on wafer bonding, lithography and etching, advanced III-V nanostructures on insulator can readily be formed for photonic applications [332, 333, 334, 335]. These approaches

however, come at the cost of fabrication complexity and surface damage created during the etching process which negatively impacts device performance. An alternative approach is the direct monolithic growth of semiconductor micro- and nanostructures [336, 337, 338, 339, 254]. Advancements in epitaxy techniques recently enabled the synthesis of high quality single crystalline material in various shapes, like nanowires [201], nano- and microfins [221], microdisks [340], or microrings [341]. In contrast to semiconductor geometries obtained from etching, these structures are enclosed by as-grown crystal facets with superior quality. Moreover, materials that are not available in bulk form, like metastable wurtzite (WZ) III-Vs, can be grown and investigated [105, 342, 268]. Synthesizing these materials in their thermodynamically less stable phase is challenging, but highly interesting in terms of optical properties. For instance, the entire composition spectrum of WZ InAlGaP shows a direct band gap transition, in contrast to their natural zinc-blende (ZB) counterparts [42, 98, 106]. Hence, metastable III-V materials are seen as a potential solution for the long-standing problem of realizing efficient green LEDs and laser diodes, commonly referred to as “green gap” [54]. Using conformal epitaxy or zipper-induced epitaxial lateral overgrowth (ELO) techniques, we demonstrated the growth of extended and pure WZ InP layers with layer dimensions ranging from  $<1\ \mu\text{m}^2$  to  $>100\ \mu\text{m}^2$  [303, 315]. In addition, the growth of various WZ microstructures, such as membrane-, prism-, and ring-like shapes by selective area epitaxy was recently shown [108].

In this work, we present a versatile optical platform by demonstrating the growth of various InP micro- and nanostructures on an InP substrate with 300 nm oxide to provide optical isolation from the substrate. The structures are grown in a single growth run and thorough optical characterization is performed. The platform allows for exact positioning of epitaxially grown hexagons and related micro- and nano-sized shapes enclosed by a subset of the low-energy m- and a-plane facets, such as triangles, rhombi, fins, stars, or wires. Complex arrangements, e.g. arrays of hexagons with diameters ranging from 500 nm to 5  $\mu\text{m}$  and precise spacing can be achieved. Since the epitaxially grown crystals are only connected to the substrate via thin fins and otherwise separated by an oxide layer, optical isolation is achieved.

Devices are fabricated using a three-step growth sequence: (1) inducing the transition of crystal phase to WZ, (2) anisotropic growth of WZ-fins and (3) zipper-induced ELO. The main steps of the formation process for a cavity of a microdisk laser are sketched in Figure 6.2(a)-(d). A standard InP(111)A substrate is covered by 300 nm PECVD  $\text{SiO}_2$  after which narrow ( $\sim 50$  nm) lines are patterned by e-beam lithography and dry-etching techniques (see **Experimental Section** for details on the fabrication). The diameter of the microdisk will be determined by the length of the lines which are connected centrally and follow the three equivalent  $\langle 110 \rangle$ -directions. Metal-organic vapor phase epitaxy (MOVPE) allows for the selective nucleation of InP in the trenches and switching to WZ phase, followed by a highly selective and vertical growth along the  $[111]\text{A}$  direction. After the fins extend out of the oxide layer, the zipper-points at the center induce an ELO process until the stable  $\{1\bar{1}00\}$  (m-plane) or metastable  $\{11\bar{2}0\}$  (a-plane) WZ facets are formed [108]. Figure 6.2(e) depicts a scanning electron microscope (SEM) image of a typical InP microdisk obtained during a growth time of 5 min, and after removing the oxide masking layer to reveal the underlying pedestal fin structure. The resulting

microdisk has noticeable lower sidewall surface roughness compared to the underlying fin structures as well as to InP structures obtained by reactive ion etching processes.

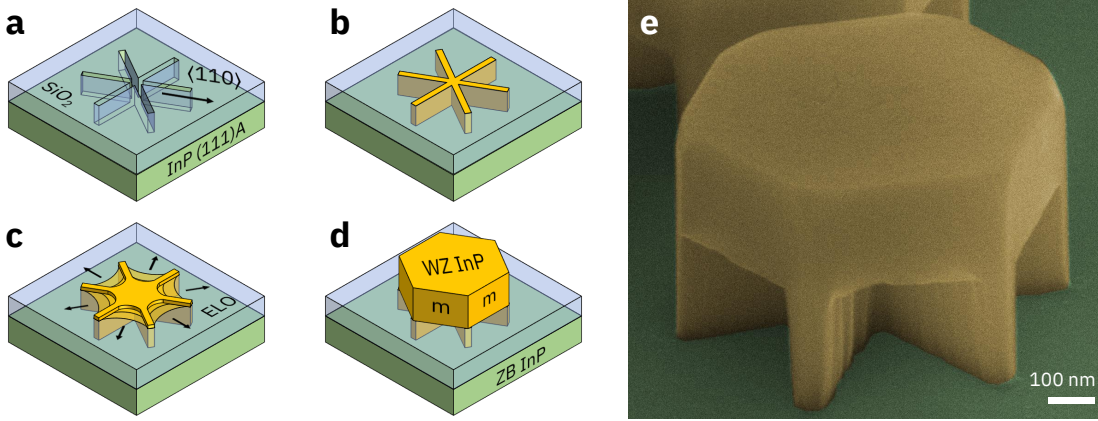


**Figure 6.2** | Concept for WZ InP microdisk epitaxy. (a)  $\langle 110 \rangle$ -oriented lines are patterned on a standard InP (111)A substrate covered with 300 nm  $\text{SiO}_2$  by e-beam lithography and dry etching. (b) Growth is initiated in a fin-mode which allows for crystal phase switching to pure WZ. (c) Zipper-induced ELO maintains the metastable phase and provides for the formation of (d) hexagonally shaped microdisks with flat crystalline m-plane sidewalls. (e) False-colored  $60^\circ$  tilted SEM image of a typical structure with 900 nm diameter after removing the  $\text{SiO}_2$  layer, revealing the pedestal fin structure.

The growth technique offers interesting options for designing a specific photonic structure, but also combinations of structures that can be grown in a single step. This includes hexagons of different sizes which can resemble either (nano-)wires or (micro-)disks. Crystal heights are mainly determined by deposition time, but also by diffusion mechanisms, which results in higher growth rates for hexagons with smaller diameter as illustrated in Figure 6.3(a). Moreover, the resulting features are accurately defined by lithography and the respective resolution limit, including gap sizes as demonstrated in Figure 6.3(b). Periodic arrays consisting of multiple structures, like hexagons, can be formed. Additionally, a wide range of different geometries and polygons can be grown together with no additional fabrication steps after epitaxy. This principle is exemplified in Figure 6.3(c) and (d). Angled lines expand to rhomboids [108] that are enclosed by low energy facets and form structures that could serve as waveguides. Similarly, an elongated hexagon can be obtained by extending one of the seed lines. In principle, any convex shape can be envisioned which can be formed by m- and a-type facets, including for example triangles and rectangles. The well controlled and deliberate expansion of the exemplified structures beyond the width of the underlying fin together with the thick oxide mask layer are key for optical isolation and photonic functionality.

To obtain high quality optical devices from InP nanostructures, excellent crystalline quality needs to be achieved. Hence, we investigate the crystal structure and phase purity of the grown structures. Figure 6.4(a) depicts a cross-sectional scanning transmission electron microscope (STEM) image of a typical microdisk with 1.5  $\mu\text{m}$  diameter imaged along a  $\langle 110 \rangle$  zone-axis. Substrate and microdisk are divided by an oxide layer (dark), which is interrupted by three vertical bright stripes. These correspond to the line openings (compare Figure 6.2(a)), as

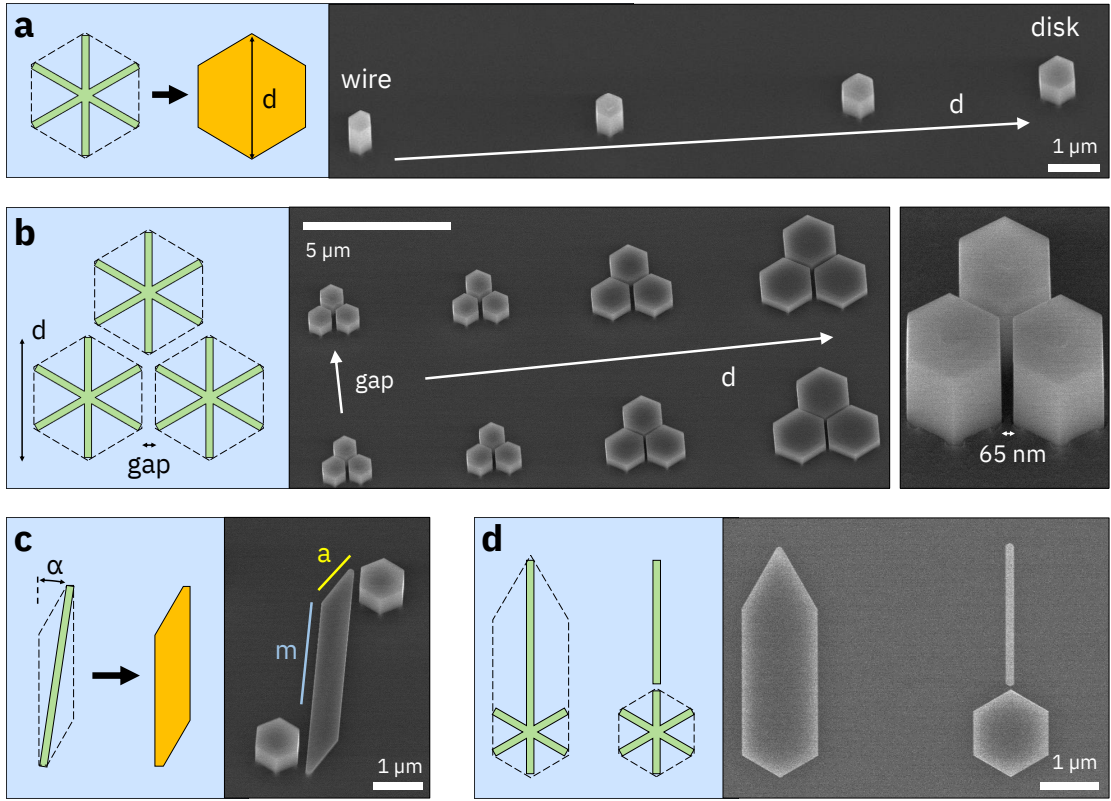


**Figure 6.3** | Growth of structures with different feature sizes and geometries applicable to photonic devices. (a) Changing the diameter of patterned stars allows to grow a range of feature sizes from wires to disks. (b) Multiple disks can be placed closely together to obtain arrays with tunable gap sizes. (c) Angular misaligned lines extend to an enclosing rhomboid formed from *m*- and *a*-planes. (d) The difference of a line opening connected and in proximity to a hexagon on the resulting crystal shape.

they are observed in a lamella which is slightly off-centered with respect to the hexagon-axis (inset of Figure 6.4(a)). In order to investigate the crystal phase and defects we perform HR-STEM characterization in Figure 6.4(b)-(g). We observe a transition from ZB to WZ phase after the crystal has extended approximately 5 nm into the oxide template. This is attributed to the initial growth stage at lower temperature, combined with the surface roughness of the substrate. At closer inspection the abruptness of this phase transition is revealed. The high-angle annular dark field (HAADF) image in Figure 6.4(c) suggests that only a single bilayer (stacking fault) divides a pure ZB (ABCABC...) from a pure WZ (ABAB...) stacking sequence. Following this transition, fault-free WZ phase is observed (exemplified in two additional HR-STEM images) up to the flat top facet in the central area. Close to the side-facets, a ring-like structure terminates the top-surface, which is approximately 30 nm high. In stark contrast to the phase purity of the microdisk below, this ring shows ZB phase with high amount of stacking faults as indicated in Figure 6.4(g). We assign this to the continued growth at reduced temperatures during the first seconds of the cool-down (see **Experimental Section**).

In order to assess optical properties, the devices are characterized using a  $\mu$ -photoluminescence

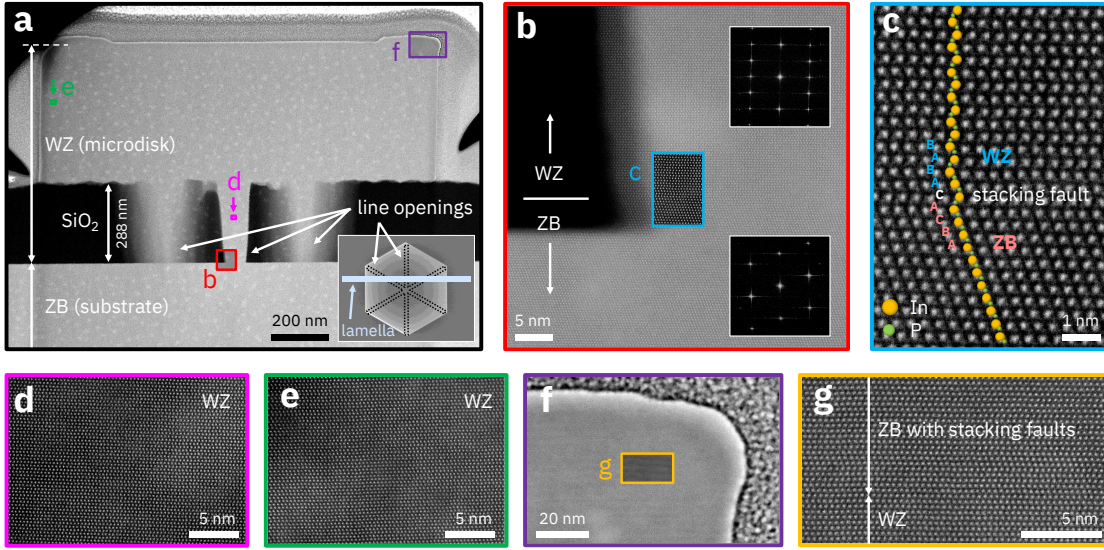


**Figure 6.4** | HAADF-STEM characterization of a representative microdisk. (a) FIB cross section of a microdisk with a diameter of 1.5  $\mu\text{m}$  and a height of 475 nm. The inset shows a top view image of the approximate position of the lamella with respect to the hexagon. Red, pink, green and purple marked areas indicate regions of interest, which are investigated in more detail. (b) High-resolution image at the central opening reveals a transition from ZB to WZ phase 5 nm from the substrate surface. Fast Fourier transform (FFT) images substantiate this observation. The area framed in blue is magnified in (c), which depicts the stacking change from ZB to WZ phase. A single stacking fault is obtained between otherwise phase-pure regions. (d)-(e) High-resolution images show pure WZ phase at various positions of the microdisk. (f-g) Magnification of the top right corner, showing faulted ZB material for the last 30 nm of the growth.

(PL) setup with a ps-pulsed supercontinuum laser at 750 nm wavelength. A 100 $\times$  objective is used to illuminate the devices from the top and collect their optical response. Figure 6.5(a) depicts the photoluminescence response of a 2  $\mu\text{m}$  WZ microdisk for increasing excitation fluences (20 – 295  $\mu\text{J}/\text{cm}^2$ ). At low illumination, the spontaneous emission of the microdisk is visible with a peak position of 880 nm corresponding to the bandgap energy of WZ InP and hence, confirming the crystal phase [303]. Upon increasing laser power, a resonant mode starts forming at 875 nm. This can be observed in Figure 6.5(b), where the integrated linear light in light out (LL) curve of the measured cavity mode is plotted. A clear kink marks the onset of lasing. By performing a linear fit on the right-hand side of the graph, the threshold of the resonant cavity mode can be determined to 365  $\mu\text{J}/\text{cm}^2$ . In logarithmic representation, a clear S-shape is revealed which is characteristic for a laser. Alongside with the strong increase of the emission in the resonant cavity mode, we observe a linewidth narrowing, another indication for lasing (see inset in Figure 6.5(b)). The increase of the linewidth at high pump powers is due to a blueshift of the resonant wavelength arising from refractive index changes and is widely observed in similar systems [343, 337]. Additional insights can be obtained by analyzing far field images of the optical response taken with a standard camera. As shown in Figure 6.5(c) the spontaneous emission is visible at low excitation fluences. With increasing pump energy, the emission of the devices gets stronger and fringes start forming. At high excitation fluences,

a clear far-field radiation pattern with interference fringes is visible because of the extended first-order coherence of the laser emission. Room-temperature lasing operation in as-grown microdisks confirms the sufficient optical isolation provided by the 300 nm thick oxide layer introduced during fabrication, which was chosen for this first proof-of-concept.

To further quantify the material quality and the lasing performance, we perform time-correlated single photon counting (TCSPC) measurements. The sample is again illuminated with a 750 nm ps-pulsed supercontinuum laser using a 100 $\times$  objective. Figure 6.5(d) depicts the results of the TCSPC measurements. At room temperature and low excitation fluence, the ZB substrate and WZ microdisk exhibit carrier lifetimes of 1.57 ns and 239 ps, respectively. This is in agreement with results obtained in a previous work [303], and is attributed to the higher oscillator strength of the optical transition at the  $\Gamma$ -point in WZ phase [173, 314]. Under strong excitation power, the measured carrier lifetime of the WZ microdisk reduces strongly resulting in a value below the resolution limit of the measurement setup ( $<50$  ps). This strong reduction of carrier lifetime is attributed to the stimulated emission in the resonant mode observed under high excitation powers, which further confirms lasing operation of the hexagonal microdisk with laser pulse durations below  $<50$  ps. This constitutes, to the best of our knowledge, the first demonstration of a WZ InP microdisk laser. In combination with the possibility to controllably grow a range of different geometries side-by-side, our platform could have many promising future photonic applications.

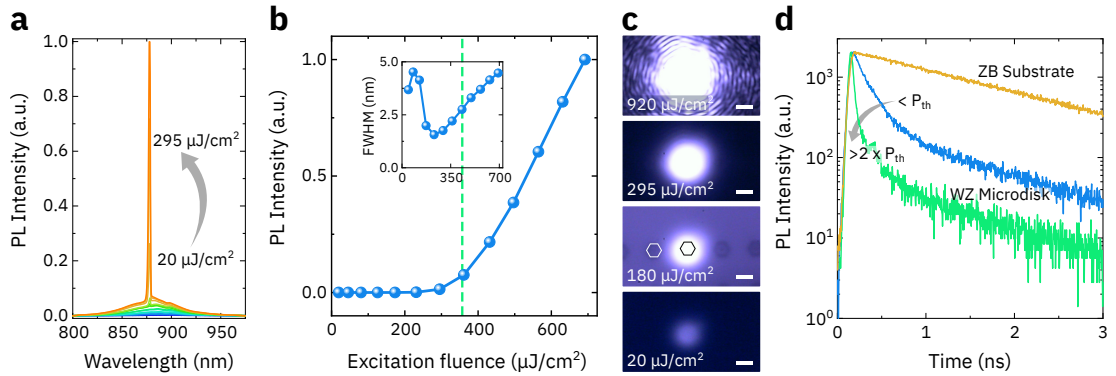


**Figure 6.5 | Optical characterization.** (a) PL spectrum of a 2  $\mu\text{m}$  WZ microdisk for increasing optical excitation at the onset of lasing. (b) Linear LL curve of the device measured in (a). The inset shows the FWHM of the resonant mode versus excitation fluence. The dashed line depicts the laser threshold. (c) Far field images of the device in (a) at different excitation fluences. The image at 180  $\mu\text{J}/\text{cm}^2$  is taken under white light illumination. The hexagonal shapes indicate the fabricated devices. The scale bar in all far field images corresponds to 2  $\mu\text{m}$ . (d) TCSPC measurements of the ZB substrate, and a microdisk below and above threshold ( $>2 \times P_{th}$ ).

In conclusion, we developed a methodology based on selective area epitaxy specifically tailored for the fabrication of photonic devices. High resolution lithographic patterning and thick oxide masks enable precise positioning and optical isolation, while zipper-ELO leads to large devices with defect-free and smooth crystal surfaces. Besides hexagonal microdisks we show a range of additional shapes to exemplify the capabilities of our platform. The unique

fabrication approach allowed for the demonstration of optically driven lasing from hexagonal WZ InP cavities with a threshold of  $365 \mu\text{J}/\text{cm}^2$ . Finally, the concepts introduced are generic and could therefore also find applications in other commercially important material systems such as InAlGaP and III-nitrides.

### Experimental Section

**Substrate fabrication.** An InP(111)A wafer was covered with nominally 300 nm plasma-enhanced chemical vapor deposited (PECVD)  $\text{SiO}_2$  (288 nm measured during STEM). This thickness provides a compromise between sufficient optical isolation of the optical mode in the III-V material and fabrication simplicity. Line openings with widths of approximately 50-100 nm and varying lengths were patterned along the three equivalent  $\langle 110 \rangle$ -directions by e-beam lithography (EBL) and reactive ion etching (RIE) in a  $\text{CHF}_3/\text{O}_2$  plasma. Prior to growth the substrate was cleaned in acetone, isopropanol and  $\text{O}_2$  plasma.

**MOVPE growth.** InP growth was carried out in a cold-wall showerhead MOCVD reactor using  $\text{H}_2$  carrier gas, tertiarybutylphosphine (TBP) and trimethylindium (TMIn) at a total pressure of 8000 Pa. Partial pressures for TBP and TMIn were 8.2 Pa and 82 mPa, respectively, resulting in a nominal V/III ratio of 100. Before growth, the reactor was heated to  $630^\circ\text{C}$  in a TBP atmosphere. Subsequently, deposition was initiated by introducing TMIn into the chamber. The substrate temperature was ramped up to  $640^\circ\text{C}$  within the first 60 s, the final growth temperature. This procedure was developed in order to prevent substrate desorption prior to the nucleation process. Deposition time was between 5 min and 30 min. Rapid cooling was started for the last 50 s of the growth, after which TMIn supply was terminated and cooling proceeded in TBP atmosphere.

**Optical characterization.** Optical characterization is performed using a  $\mu$ -photoluminescence (PL) setup with a ps-pulsed supercontinuum laser at 750 nm (78 MHz repetition rate). The sample is illuminated from the top using a  $100\times$  objective (NA 0.6) which also collects the optical response of the sample. All measurements are performed at 300 K and under ambient conditions. The collected optical response is analyzed using a monochromator and an InGaAs CCD camera. Time-correlated single photon counting (TCSPC) measurements are performed in the same setup, using the 750 nm ps-pulsed supercontinuum laser and the  $100\times$  objective. A Si single photon detector is used to measure the optical response. Since the signal of the sample is very strong, a high-density filter was used to reduce the power of optical light incident on the detector. Using a TCSPC measurement module (PicoHarp 300), the lifetime of the sample can be determined. The resolution of the setup is 50 ps due to the temporal pulse shape of the supercontinuum laser.

### **Acknowledgements**

The authors gratefully acknowledge Preksha Tiwari, Marilyne Sousa, Anna Fontcuberta i Morral and Heike Riel for fruitful technical discussions, as well as, the BRNC staff for technical support. The work presented here has received funding from the European Union H2020 program SiLAS (Grant Agreement No. 735008) and the ERC Starting Grant project PLASMIC (Grant Agreement No. 678567).

## **6.2 Main Achievements**

In summary the following results have been obtained in this chapter:

- A platform for the synthesis of optically isolated crystals was developed, which allows for the fabrication of resonant cavities and photonic structures.
- InP microdisks and related geometries were grown with high precision and control.
- By careful exploration of the design space we demonstrated the possibility for the direct growth of virtually any shape that is enclosed in a combination of m- and a-plane facets, including triangles, rhombi, fins, stars, or wires.
- Structures can be grown in a single step with defined dimensions and gap sizes.
- For the first time, room-temperature lasing from WZ InP microdisks was demonstrated.
- A resonant mode forms at 875 nm for microdisks with a diameter of 2  $\mu\text{m}$ , at a threshold of 365  $\mu\text{J}/\text{cm}^2$ .
- Upon lasing, we observe a reduction of the carrier life from 239 ps to below 50 ps, limited by the resolution of the measurement setup.



## 7 Conclusion and Outlook

*“Around here, however, we don’t look backwards for very long. We keep moving forward, opening up new doors and doing new things, because we’re curious ... and curiosity keeps leading us down new paths.”*

– Walt Disney

In this thesis we developed and explored new strategies for *crystal phase engineering* in planar layers. Most of the results are demonstrated on the example of InP as it is a material with high ionicity and both the stable ZB and the metastable WZ phase exhibit a direct, but distinctive band gap, which allows for efficient optical analysis. Our results contribute to the understanding of metastable film growth and may pave the way towards large-scale crystal phase engineered devices.

In **Chapter 4** we introduced conformal epitaxy. This technique is highly interesting as it enables selecting confined growth planes during epitaxy, and thus to study their importance on the formation of metastable phases. We demonstrated that only a specific growth orientation permits the introduction of stacking faults in InP – an intermediate step towards the formation of the hexagonal phase. In analogy to fin epitaxy, we maintained a comparably small growth facet that allowed us to tune the crystal structure to nearly pure WZ. At the same time, the capping oxide enabled us to obtain planar layers on standard (001)-oriented substrates, the first demonstration of its kind. Even more, we showed that by growing along other directions during the same deposition run, we could concurrently synthesize ZB and WZ layers in high quality. This is another clear advantage over NW growth, where until now similar results are obtained only by coincidence rather than deliberately predefined through the seed orientation [319]. Not only was this the first time that WZ InP was synthesized in dimensions where bulk properties dominate, we simultaneously obtained ZB InP grown at exactly the same conditions, with equal morphology and surface quality. Hence, we developed an ideal platform to investigate the properties of WZ InP and compare them with the well-studied cubic phase. In this way we found indications for a higher oscillator strength of the optical transition at the  $\Gamma$ -point in WZ InP, which is very interesting for many optical applications. We proposed a model to describe our findings and demonstrated the scalability of our approach by growing WZ InP at sizes up to  $50\text{ }\mu\text{m}^2$ . Additionally, first important results were established

for GaAs films. The lower phase-control motivated us to develop a two-step approach that combines the advantages of VLS and CE. In this way, pure WZ GaAs layers were synthesized and a clear route towards metastable films of a large range of materials was established.

**Chapter 5** described zipper-induced epitaxial lateral overgrowth as another technique for metastable film synthesis. Starting from fin epitaxy, a phase change from ZB to WZ InP could be achieved along vertical direction. In order to trigger an epitaxial lateral overgrowth and thus film formation, simply changing growth parameters is not a viable option as the m-planes on the fin-sidewalls tend to be very stable and exhibit extraordinarily low growth rate, regardless the reactor conditions. On the other hand, besides its necessity for obtaining layers, growth along the lateral direction is also favorable for transferring the crystal phase of the fin structures. We thus explored a new technique that makes use of creating unstable concave edges between individual fins in order to deliberately induce so-called zipper points. The intermediate facets that are enforced in this way show high growth rate and are thus suitable for efficient lateral overgrowth. Additionally, due to the high selectivity with respect to the m-plane facets, this technique allows for precise control of the layer dimensions. We made use of these advantages to explore the size limitations of WZ film synthesis in publication 2. At given growth conditions, we established a transition point from WZ to ZB of around  $100\text{ }\mu\text{m}^2$ . This result was consistent using different growth strategies, which points towards a fundamental size limitation. Hence, we developed a nucleation-based model that extends existing theory to explain our results qualitatively. Even though our model predicts that no infinitely large WZ layer can be grown from a common growth origin, we explore a route to generate a virtually continuous substrate by tiling individual crystals in a closely arranged array. It is envisaged that these structures can be merged together in a second epitaxy step to form a layer with only minor defects at the merging points.

Zipper-ELO is a powerful technique to form layers with large dimensions that can be used for planar device fabrication. As we showed in **Chapter 6**, this method also has another advantage. The underlying oxide layer can be made thick enough to obtain optical isolation from the substrate. In combination with defined positioning, size control and as-grown smooth crystalline facets, this technique provides an ideal platform to directly synthesize optical structures with high quality. This was showcased in publication 3, where we demonstrated room-temperature lasing from a hexagonal WZ InP microdisk directly grown in a single step. Even more, this platform allows to obtain virtually any shape that is enclosed in a combination of m- and a-plane facets, including triangles, rhombi, fins, stars, or wires. Precise lithographic positioning enables narrow and defined gap sizes that can be used for example for optical coupling between various structures. This opens up manifold future applications including photonic crystals and random laser arrays.

In Fig. 7.1 we summarize our results and put them in context of the state of the art. A comprehensive understanding of metastable film growth was acquired during this research project. Two new techniques were presented, which are based on the ability to form a metastable phase in a catalyst-free epitaxy. We demonstrated that if such a growth window exists, we can extend

these materials to planar layers. So far, InP and related ternaries are the only known III-Vs for which this is possible. Advances in the catalyst-free epitaxy of metastable semiconductors are expected to increase also the range of materials that can be grown in planar films using one of our approaches. Until then, we suggest a two-step technique that combines the advantages of VLS and CE. Given the versatility of VLS, we believe that a large range of materials can be synthesized in this way.

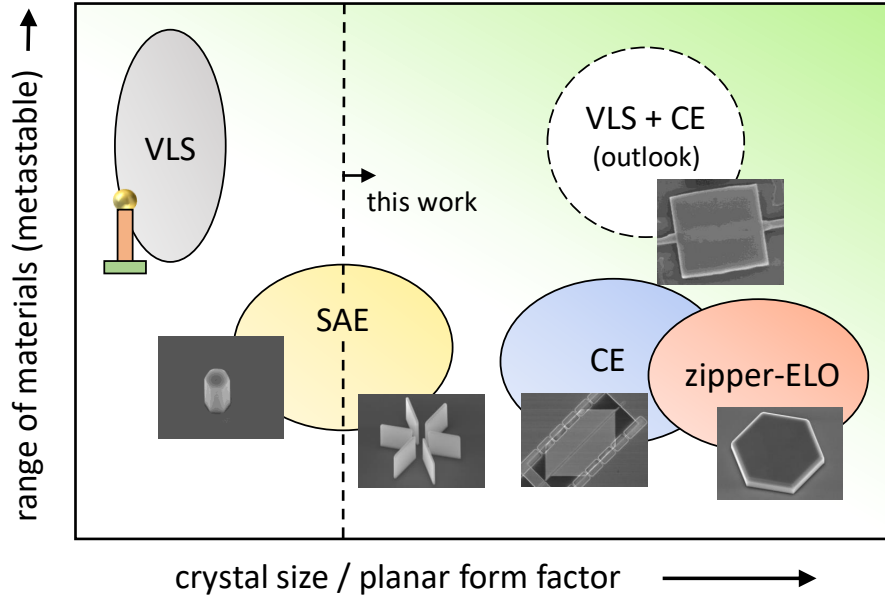


**Figure 7.1** | Qualitative map showing the techniques and results presented in this thesis compared to the state of the art for growth of metastable materials. Order of magnitude larger crystals sizes have been synthesized, extending the capabilities of selective area epitaxy techniques. For the first time, metastable WZ III-Vs have been grown with planar form factor. A promising 2-step approach (VLS + CE) is presented for future growth of metastable films of a larger range of materials.

## 7.1 Future Directions

This work presents viable routes for synthesizing planar layers of metastable material, thus bringing the interesting properties of this new kind of matter closer to application. As a material of choice, InP was primarily used throughout this thesis to demonstrate the principle and to establish a proof of concept. To increase the range of application, focus for future work needs to be put on the exploration of additional material systems. So far, this has proven difficult as other III-Vs or SiGe have less or no ionicity, a fundamental property that is known to promote WZ formation. It is possible that there are no suitable growth condition that directly generate WZ phase in many of these materials without using a catalyst. Hence, we propose additional ideas to synthesize planar films of such materials based on our findings:

- Conformal epitaxy provides layers that can be used as a virtual substrate. Template removal and a follow up planar epitaxy could be used to grow thin films of other materials

on top of WZ InP. However, the large lattice mismatch between InP and other materials has to be considered to avoid degradation resulting in less phase purity [109].

- Another two-step approach could overcome this limitation, though at the cost of increased complexity. VLS growth enables the synthesis of a large range of materials in metastable phase (compare Tab. 1.2). Integration of such a NW inside a template, such that a following epitaxy is restricted to specific growth planes, enables the formation of

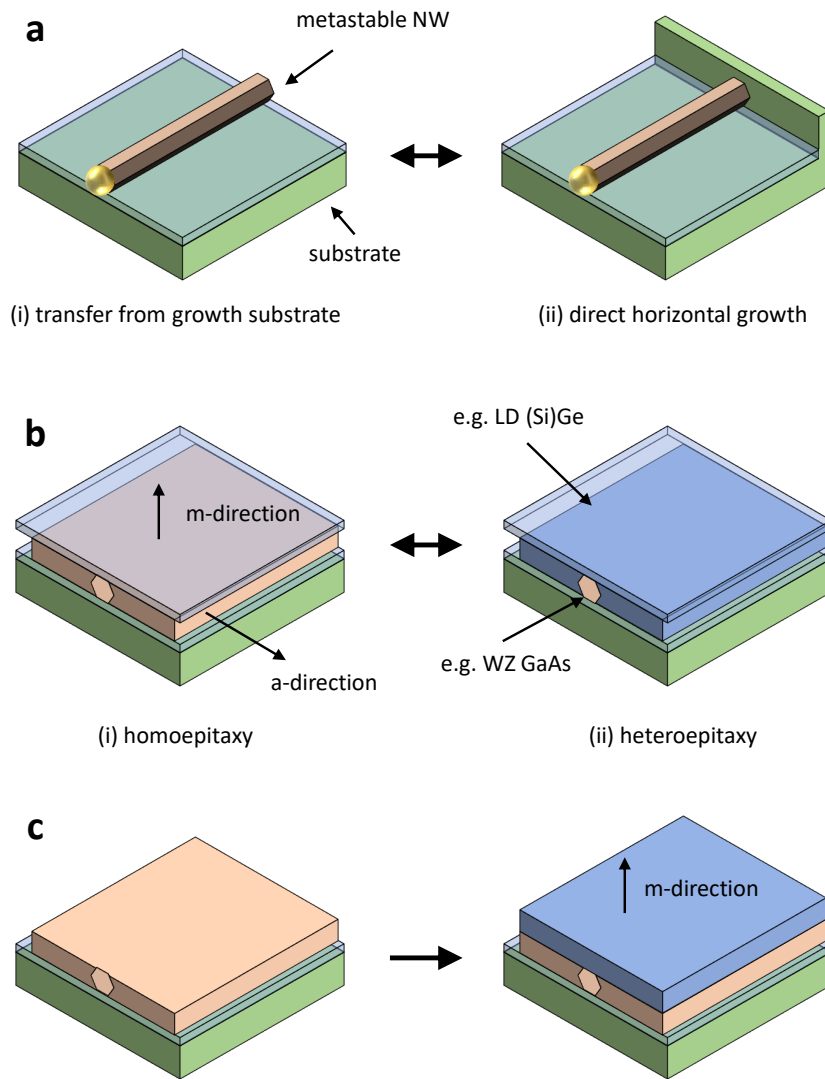


**Figure 7.2** | Ideas for synthesizing a larger range of metastable materials. (a) A metastable VLS NW is either (i) transferred to an isolated substrate or (ii) directly grown horizontally. (b) A template is formed around the NW for CE to confine the growth plane to the a-direction, which effectively hinders phase-change. Using (i) homoepitaxy or (ii) heteroepitaxy, various metastable materials can be grown in layers. (c) Removing the oxide template followed by planar epitaxy can also be used to synthesize thin films of materials that are not available in metastable phase as NWs.

layers by transferring the metastable crystal phase of the seed crystal, as demonstrated for GaAs in **Chapter 4**. As depicted in Fig. 7.2(a), instead of transferring NWs from another substrate, a route for direct horizontal growth can be envisioned, and will be explored in future work.

- Up to now, some materials can also not be grown directly using VLS. This includes the very interesting group IV semiconductors in LD phase. Motivated by heteroepitaxial shell growth in vertical NWs, we propose an idea to obtain planar layers by using a dissimilar core-NW material as indicated in Fig. 7.2(b)ii. In addition to the planar form factor, the confined growth plane should allow for prolonged expansion without compromising material quality, as compared to shell growth.
- Yet another idea we started to explore is sketched in Fig. 7.2(c). Removal of the top-oxide, followed by a planar growth should be suitable for the synthesis of thin layers of lattice matched materials. The m-plane surface is believed to be beneficial for this purpose, as it will transfer the crystal phase and remain stable during epitaxy.

A US patent application relevant to these approaches has recently been filed and we continue to pursue them particularly for the synthesis of metastable GaAs and (Si)Ge layers in collaboration with the E.P.A.M. Bakkers group at TU Eindhoven.

Other possible directions include the utilization of different deposition techniques. Hydride vapor phase epitaxy seems particularly suited for this task owed to its high selectivity and deposition rate as desired for conformal epitaxy. We are exploring this route in an active collaboration with the Y. Andre group at Institut Pascal in Clermont-Ferrand.

Given our promising results on the direct synthesis of optical devices with metastable WZ phase, further research should focus on device fabrication, doping and contact formation of these new materials. We have worked towards this goal in the framework of the H2020 SiLAS project using LD SiGe. Further studies on doping and contacting approaches are well underway. As a first demonstration we envision LEDs, either made from LD (Si)Ge or WZ In(Al)P, which both could be of enormous interest for the semiconductor industry.



## References

- [1] S. Milisauskas, *European prehistory: A survey*. Springer Science & Business Media, 2011.
- [2] M. Miodownik, “Why the Story of Materials is really the Story of Civilization”, *The Guardian*, 2014.
- [3] W. Brinkman, D. Haggan, and W. Troutman, “A history of the invention of the transistor and where it will lead us”, *IEEE Journal of Solid-State Circuits*, 32, 12, 1858–1865, 1997.
- [4] J. S. Kilby, “The Integrated Circuit’s Early History”, *Proceedings of the IEEE*, 88, 1, 109–111, 2000.
- [5] A. Borcuch, M. Piłat-Borcuch, and U. Świerczyńska-Kaczor, “The Influence of the Internet on globalization process”, *Journal of Economics and Business Research*, 18, 1, 118–129, 2012.
- [6] I. M. Ross, “The foundation of the silicon age”, *Bell Labs technical journal*, 2, 4, 3–14, 1997.
- [7] J. M. Woodall, “III-V compounds and alloys: An update”, *Science*, 208, 4446, 908–915, 1980.
- [8] C. Wang, J.-C. Chien, H. Fang, K. Takei, J. Nah, E. Plis, S. Krishna, A. M. Niknejad, and A. Javey, “Self-Aligned, Extremely High Frequency III–V Metal-Oxide-Semiconductor Field-Effect Transistors on Rigid and Flexible Substrates”, *Nano Letters*, 12, 8, 4140–4145, 2012.
- [9] G. Formicone, J. Burger, and J. Custer, “150 V-Bias RF GaN for 1 kW UHF Radar Amplifiers”, in *IEEE Compound Semiconductor Integrated Circuit Symposium (CSICS)*, IEEE, 2016, 1–4.
- [10] J. E. Goell and Y.-Z. Liu, *Light-emitting diode fabrication process*, 1976.
- [11] Y. Horikoshi and Y. Furukawa, “Temperature Sensitive Threshold Current of InGaAsP–InP Double Heterostructure Lasers”, *Japanese Journal of Applied Physics*, 18, 4, 809, 1979.

## References

---

- [12] T. Okoshi, “Recent advances in coherent optical fiber communication systems”, *Journal of lightwave technology*, 5, 1, 44–52, 1987.
- [13] B. van Dongen, H.-P. Renk, P. Selgert, and H. Visser, “Fibre-optics : 21st century communication backbone”, 11, 2016.
- [14] J. Han, M. H. Crawford, R. J. Shul, J. J. Figiel, M. Banas, L. Zhang, Y. K. Song, H. Zhou, and A. V. Nurmikko, “AlGaIn/GaN quantum well ultraviolet light emitting diodes”, *Applied physics letters*, 73, 12, 1688–1690, 1998.
- [15] S. Nakamura, S. Pearton, and G. Fasol, “The Blue Laser Diode: The Complete Story”, *Measurement Science and Technology*, 12, 755, 2001.
- [16] P. M. Pattison, M. Hansen, and J. Y. Tsao, “LED lighting efficacy: Status and directions”, *Comptes Rendus Physique*, 19, 3, 134–145, 2018.
- [17] A. Bett, F. Dimroth, G. Stollwerck, and O. Sulima, “III-V compounds for solar cell applications”, *Applied Physics A: Materials Science & Processing*, 69, 2, 119–129, 1999.
- [18] P. Krogstrup, H. I. Jørgensen, M. Heiss, O. Demichel, J. V. Holm, M. Aagesen, J. Nygard, and A. F. i Morral, “Single-nanowire solar cells beyond the Shockley–Queisser limit”, *Nature Photonics*, 7, 4, 306–310, 2013.
- [19] Y. Cui, J. Wang, S. R. Plissard, A. Cavalli, T. T. T. Vu, R. P. J. Van Veldhoven, L. Gao, M. Trainor, M. A. Verheijen, J. E. M. Haverkort, and E. P. A. M. Bakkers, “Efficiency enhancement of InP nanowire solar cells by surface cleaning”, *Nano Letters*, 13, 9, 4113–4117, 2013.
- [20] J. Wallentin, N. Anttu, D. Asoli, M. Huffman, I. Aberg, M. H. Magnusson, G. Siefer, P. Fuss-Kailuweit, F. Dimroth, B. Witzigmann, H. Q. Xu, L. Samuelson, K. Deppert, and M. T. Borgstrom, “InP Nanowire Array Solar Cells Achieving 13.8% Efficiency by Exceeding the Ray Optics Limit”, *Science*, 339, 6123, 1057–1060, 2013.
- [21] M. Yoshimura, E. Nakai, K. Tomioka, and T. Fukui, “Indium Phosphide Core–Shell Nanowire Array Solar Cells with Lattice-Mismatched Window Layer”, *Applied Physics Express*, 6, 5, 052301, 2013.
- [22] S. M. Frolov, S. R. Plissard, S. Nadj-Perge, L. P. Kouwenhoven, and E. P. A. M. Bakkers, “Quantum computing based on semiconductor nanowires”, *MRS bulletin*, 38, 10, 809–815, 2013.
- [23] D. Aasen, M. Hell, R. V. Mishmash, A. Higginbotham, J. Danon, M. Leijnse, T. S. Jespersen, J. A. Folk, C. M. Marcus, K. Flensberg, and J. Alicea, “Milestones Toward Majorana-Based Quantum Computing”, *Physical Review X*, 6, 3, 031016, 2016.
- [24] M. Friedl, K. Cervený, P. Weigele, G. Tütüncüoglu, S. Martí-Sánchez, C. Huang, T. Patlatiuk, H. Potts, Z. Sun, M. O. Hill, L. Güniat, W. Kim, M. Zamani, V. G. Dubrovskii, J. Arbiol, L. J. Lauhon, D. M. Zumbühl, and A. Fontcuberta i Morral, “Template-Assisted Scalable Nanowire Networks”, *Nano Letters*, 18, 4, 2666–2671, 2018.

- 
- [25] L. Q. Chen, L. D. Chen, S. V. Kalinin, G. Klimeck, S. K. Kumar, J. Neugebauer, and I. Terasaki, "Design and discovery of materials guided by theory and computation", *npj Computational Materials*, 1, 2015.
- [26] A. R. Verma and P. Krishna, "Polymorphism and polytypism in crystals", *John Wiley & Sons*, 1965.
- [27] G. R. Desiraju, J. J. Vittal, and A. Ramanan, *Crystal engineering: a textbook*. World Scientific, 2011.
- [28] H. O. Pierson, *Handbook of carbon, graphite, diamonds and fullerenes: processing, properties and applications*. William Andrew, 2012.
- [29] C.-Y. Yeh, Z. W. Lu, S. Froyen, and A. Zunger, "Zinc-blende - wurtzite polytypism in semiconductors", *Physical Review B*, 46, 16, 1992.
- [30] A. De and C. E. Pryor, "Electronic Structure and Optical Properties of Si, Ge and Diamond in the Lonsdaleite Phase", *Journal of Physics: Condensed Matter*, 26, 4, 045801, 2014.
- [31] K. W. Ng, W. S. Ko, F. Lu, and C. J. Chang-Hasnain, "Metastable Growth of Pure Wurtzite InGaAs Microstructures", *Nano Letters*, 14, 8, 4757–4762, 2014.
- [32] C. Frondel and U. B. Marvin, "Lonsdaleite, a hexagonal polymorph of diamond", *Nature*, 214, 5088, 587, 1967.
- [33] A. Misra, P. K. Tyagi, B. S. Yadav, P. Rai, D. S. Misra, V. Pancholi, and I. D. Samajdar, "Hexagonal diamond synthesis on h-GaN strained films", *Applied Physics Letters*, 89, 7, 071911, 2006.
- [34] A. G. Kвашnin and P. B. Sorokin, "Lonsdaleite Films with Nanometer Thickness", *The Journal of Physical Chemistry Letters*, 5, 3, 541–548, 2014.
- [35] Z. Pan, H. Sun, Y. Zhang, and C. Chen, "Harder than Diamond: Superior Indentation Strength of Wurtzite BN and Lonsdaleite", *Physical Review Letters*, 102, 5, 055503, 2009.
- [36] L. Qingkun, S. Yi, L. Zhiyuan, and Z. Yu, "Lonsdaleite – A material stronger and stiffer than diamond", *Scripta Materialia*, 65, 3, 229–232, 2011.
- [37] S. Q. Wang and H. Q. Ye, "First-principles study on the lonsdaleite phases of C, Si and Ge", *Journal of Physics: Condensed Matter*, 15, 12, L197–L202, 2003.
- [38] T. Miyoshi, Y. Kurihara, and M. Ura, *Gallium arsenide infrared light emitting diode*, 1977.
- [39] A. A. Bergh and P. J. Dean, "Light-emitting diodes", *Proceedings of the IEEE*, 60, 2, 156–223, 1972.
- [40] D. R. Wight, "Green luminescence efficiency in gallium phosphide", *Journal of Physics D: Applied Physics*, 10, 4, 431, 1977.
- [41] S. P. Najda, A. H. Kean, M. D. Dawson, and G. Duggan, "Optical measurements of electronic bandstructure in AlGaInP alloys grown by gas source molecular beam epitaxy", *Journal of applied physics*, 77, 7, 3412–3415, 1995.

## References

---

- [42] A. De and C. E. Pryor, “Predicted Band Structures of III-V Semiconductors in the Wurtzite Phase”, *Physical Review B*, 81, 15, 155210, 2010.
- [43] M. Auf der Maur, A. Pecchia, G. Penazzi, W. Rodrigues, and A. Di Carlo, “Efficiency Drop in Green InGaN/GaN Light Emitting Diodes: The Role of Random Alloy Fluctuations”, *Physical Review Letters*, 116, 2, 027401, 2016.
- [44] T. Langer, A. Kruse, F. A. Ketzner, A. Schwiegel, L. Hoffmann, H. Jönen, H. Bremers, U. Rossow, and A. Hangleiter, “Origin of the “green gap”: Increasing nonradiative recombination in indium-rich GaInN/GaN quantum well structures”, *physica status solidi (c)*, 8, 7-8, 2170–2172, 2011.
- [45] Y. Jiang, Y. Li, Y. Li, Z. Deng, T. Lu, Z. Ma, P. Zuo, L. Dai, L. Wang, H. Jia, W. Wang, J. Zhou, W. Liu, and H. Chen, “Realization of high-luminous-efficiency InGaN light-emitting diodes in the “green gap” range”, *Scientific Reports*, 5, 1–7, 2015.
- [46] Q. Fan, C. Chai, Q. Wei, K. Wong, Y. Liu, and Y. Yang, “Theoretical investigations of group IV alloys in the Lonsdaleite phase”, *Journal of Materials Science*, 53, 4, 2785–2801, 2018.
- [47] R. B. Araujo, J. S. de Almeida, and A. Ferreira da Silva, “Electronic properties of III-nitride semiconductors: A first-principles investigation using the Tran-Blaha modified Becke-Johnson potential”, *Journal of Applied Physics*, 114, 18, 183702, 2013.
- [48] I. Vurgaftman, J. R. Meyer, and L. R. Ram-Mohan, “Band parameters for III–V compound semiconductors and their alloys”, *Journal of Applied Physics*, 89, 11, 5815–5875, 2001.
- [49] I. Vurgaftman and J. R. Meyer, “Band parameters for nitrogen-containing semiconductors”, *Journal of Applied Physics*, 94, 6, 3675–3696, 2003.
- [50] A. E. Romanov, T. J. Baker, S. Nakamura, and J. S. Speck, “Strain-induced polarization in wurtzite III-nitride semipolar layers”, *Journal of Applied Physics*, 100, 2, 023522, 2006.
- [51] N. Grandjean, B. Damilano, S. Dalmaso, M. Leroux, M. Laügt, and J. Massies, “Built-in electric-field effects in wurtzite AlGaN/GaN quantum wells”, *Journal of Applied Physics*, 86, 7, 3714–3720, 1999.
- [52] M. Leroux, N. Grandjean, M. Laügt, J. Massies, B. Gil, P. Lefebvre, and P. Bigenwald, “Quantum confined Stark effect due to built-in internal polarization fields in (Al,Ga)N/GaN quantum wells”, *Physical Review B*, 58, 20, R13371–R13374, 1998.
- [53] R. Leitsmann and F. Bechstedt, “Influence of the quantum confined Stark effect on photoluminescence spectra of PbTe nanodots embedded in a CdTe matrix”, *Physical Review B*, 80, 16, 165402, 2009.
- [54] M. Auf der Maur, A. Pecchia, G. Penazzi, W. Rodrigues, and A. Di Carlo, “Efficiency Drop in Green InGaN/GaN Light Emitting Diodes: The Role of Random Alloy Fluctuations”, *Physical Review Letters*, 116, 2, 027401, 2016.

- 
- [55] L. Y. Lee, “Cubic zincblende gallium nitride for green-wavelength light-emitting diodes”, *Materials Science and Technology*, 33, 14, 1570–1583, 2017.
- [56] J. H. Kim and P. H. Holloway, “Wurtzite to zinc-blende phase transition in gallium nitride thin films”, *Applied Physics Letters*, 84, 5, 711–713, 2004.
- [57] D. A. B. Miller, “Device requirements for optical interconnects to silicon chips”, *Proceedings of the IEEE*, 97, 7, 1166–1185, 2009.
- [58] H. Kawanami, “Heteroepitaxial technologies of III-V on Si”, *Solar Energy Materials and Solar Cells*, 66, 1-4, 479–486, 2001.
- [59] N. Daix, E. Uccelli, L. Czornomaz, D. Caimi, C. Rossel, M. Sousa, H. Siegwart, C. Marchiori, J. M. Hartmann, K. T. Shiu, C. W. Cheng, M. Krishnan, M. Lofaro, M. Kobayashi, D. Sadana, and J. Fompeyrine, “Towards large size substrates for III-V co-integration made by direct wafer bonding on Si”, *APL Materials*, 2, 8, 2014.
- [60] C. Rödl, J. Furthmüller, J. R. Suckert, V. Armuzza, F. Bechstedt, and S. Botti, “Accurate electronic and optical properties of hexagonal germanium for optoelectronic applications”, *Physical Review Materials*, 3, 3, 034602, 2019.
- [61] C. Raffy, J. Furthmüller, and F. Bechstedt, “Properties of hexagonal polytypes of group-IV elements from first-principles calculations”, *Physical Review B - Condensed Matter and Materials Physics*, 66, 7, 1–10, 2002.
- [62] P. S. Chen, S. T. Fan, H. S. Lan, and C. W. Liu, “Band calculation of lonsdaleite Ge”, *Journal of Physics D: Applied Physics*, 50, 1, 2017.
- [63] R. S. Wagner and W. C. Ellis, “Vapor-liquid-solid mechanism of single crystal growth”, *Applied Physics Letters*, 4, 5, 89–90, 1964.
- [64] K. Takahashi and T. Morizumi, “Growth of InAs whiskers in wurtzite structure”, *Japanese Journal of Applied Physics*, 5, 8, 657, 1966.
- [65] H. I. T. Hauge, S. Conesa-Boj, M. A. Verheijen, S. Koelling, and E. P. A. M. Bakkers, “Single-Crystalline Hexagonal Silicon–Germanium”, *Nano Letters*, 17, 1, 85–90, 2017.
- [66] E. M. T. Fadaly, A. Dijkstra, J. R. Suckert, D. Ziss, M. A. J. V. Tilburg, C. Mao, Y. Ren, V. T. V. Lange, K. Korzun, S. Kölling, M. A. Verheijen, D. Busse, C. Rödl, J. Furthmüller, F. Bechstedt, J. Stangl, J. J. Finley, S. Botti, J. E. M. Haverkort, and E. P. A. M. Bakkers, “Direct-bandgap emission from hexagonal Ge and SiGe alloys”, *Nature*, 580, 205–209, 2020.
- [67] P. Krogstrup, H. I. Jørgensen, E. Johnson, M. H. Madsen, C. B. Sørensen, A. F. I. Morral, M. Aagesen, J. Nygård, and F. Glas, “Advances in the theory of III-V nanowire growth dynamics”, *Journal of Physics D: Applied Physics*, 46, 31, 1–63, 2013.
- [68] X. Yu, H. Wang, J. Lu, J. Zhao, J. Misuraca, P. Xiong, and S. Von Molnár, “Evidence for structural phase transitions induced by the triple phase line shift in self-catalyzed GaAs nanowires”, *Nano Letters*, 12, 10, 5436–5442, 2012.

## References

---

- [69] V. G. Dubrovskii and N. V. Sibirev, “Growth thermodynamics of nanowires and its application to polytypism of zinc blende III-V nanowires”, *Physical Review B*, 77, 1–8, 2008.
- [70] F. Glas, J.-C. Harmand, and G. Patriarche, “Why Does Wurtzite Form in Nanowires of III-V Zinc Blende Semiconductors?”, *Physical Review Letters*, 99, 14, 146101, 2007.
- [71] J. Johansson, L. S. Karlsson, K. A. Dick, J. Bolinsson, B. A. Wacaser, K. Deppert, and L. Samuelson, “Effects of supersaturation on the crystal structure of gold seeded III- V nanowires”, *Crystal Growth and Design*, 9, 2, 766–773, 2009.
- [72] T. Yamashita, K. Sano, T. Akiyama, K. Nakamura, and T. Ito, “Theoretical investigations on the formation of wurtzite segments in group III-V semiconductor nanowires”, *Applied Surface Science*, 254, 23, 7668–7671, 2008.
- [73] L. Güniat, P. Caroff, and A. Fontcuberta i Morral, “Vapor Phase Growth of Semiconductor Nanowires: Key Developments and Open Questions”, *Chemical Reviews*, 119, 15, 8958–8971, 2019.
- [74] D. Jacobsson, F. Panciera, J. Tersoff, M. C. Reuter, S. Lehmann, S. Hofmann, K. A. Dick, and F. M. Ross, “Interface dynamics and crystal phase switching in GaAs nanowires”, *Nature*, 531, 7594, 317–322, 2016.
- [75] S. Lehmann, D. Jacobsson, and K. A. Dick, “Crystal phase control in GaAs nanowires: Opposing trends in the Ga- and As-limited growth regimes”, *Nanotechnology*, 26, 30, 301001, 2015.
- [76] S. Assali, L. Gagliano, D. S. Oliveira, M. A. Verheijen, S. R. Plissard, L. F. Feiner, and E. P. A. M. Bakkers, “Exploring Crystal Phase Switching in GaP Nanowires”, *Nano Letters*, 15, 12, 8062–8069, 2015.
- [77] P. Caroff, J. Bolinsson, and J. Johansson, “Crystal Phases in III-V Nanowires: From Random Toward Engineered Polytypism”, *IEEE Journal of Selected Topics in Quantum Electronics*, 17, 4, 829–846, 2011.
- [78] K. A. Dick, P. Caroff, J. Bolinsson, M. E. Messing, J. Johansson, K. Deppert, L. R. Wallenberg, and L. Samuelson, “Control of III–V nanowire crystal structure by growth parameter tuning”, *Semiconductor Science and Technology*, 25, 2, 024009, 2010.
- [79] S. Lehmann, J. Wallentin, D. Jacobsson, K. Deppert, and K. A. Dick, “A general approach for sharp crystal phase switching in InAs, GaAs, InP, and GaP nanowires using only group v flow”, *Nano Letters*, 13, 9, 4099–4105, 2013.
- [80] R. E. Algra, M. A. Verheijen, M. T. Borgström, L. F. Feiner, G. Immink, W. J. P. Van Enckevort, E. Vlieg, and E. P. A. M. Bakkers, “Twinning superlattices in indium phosphide nanowires”, *Nature*, 456, 7220, 369–372, 2008.
- [81] T. Grap, T. Rieger, C. Blömers, T. Schäpers, D. Grützmacher, and M. I. Lepsa, “Self-catalyzed VLS grown InAs nanowires with twinning superlattices”, *Nanotechnology*, 24, 33, 2013.

- 
- [82] P. Caroff, K. A. Dick, J. Johansson, M. E. Messing, K. Deppert, and L. Samuelson, "Controlled polytypic and twin-plane superlattices in III-V nanowires", *Nature Nanotechnology*, 4, 1, 50–55, 2009.
- [83] T. Burgess, S. Breuer, P. Caroff, J. Wong-Leung, Q. Gao, H. Hoe Tan, and C. Jagadish, "Twinning superlattice formation in GaAs nanowires", *ACS Nano*, 7, 9, 8105–8114, 2013.
- [84] N. Isik Goktas, A. Sokolovskii, V. G. Dubrovskii, and R. R. LaPierre, "Formation Mechanism of Twinning Superlattices in Doped GaAs Nanowires", *Nano Letters*, 20, 5, 3344–3351, 2020.
- [85] M. Mizuta, S. Fujieda, Y. Matsumoto, and T. Kawamura, "Low temperature growth of GaN and AlN on GaAs utilizing metalorganics and hydrazine", *Japanese journal of applied physics*, 25, 12, L945–L948, 1986.
- [86] C. J. Stark, T. Detchprohm, S. C. Lee, Y. B. Jiang, S. R. Brueck, and C. Wetzel, "Green cubic GaInN/GaN light-emitting diode on microstructured silicon (100)", *Applied Physics Letters*, 103, 23, 232107, 2013.
- [87] S. Kang, B. K. Kang, S. W. Kim, and D. H. Yoon, "Growth and characteristics of zinc-blende and wurtzite GaN junctioned branch nanostructures", *Crystal Growth and Design*, 10, 6, 2581–2584, 2010.
- [88] S. H. Yun, Y. H. Ra, Y. M. Lee, K. Y. Song, J. H. Cha, H. C. Lim, D. W. Kim, N. J. Suthan Kissinger, and C. R. Lee, "Growth of hexagonal and cubic InN nanowires using MOCVD with different growth temperatures", *Journal of Crystal Growth*, 312, 15, 2201–2205, 2010.
- [89] F. Furtmayr, M. Vilemeyer, M. Stutzmann, A. Laufer, B. K. Meyer, and M. Eickhoff, "Optical properties of Si- and Mg-doped gallium nitride nanowires grown by plasma-assisted molecular beam epitaxy", *Journal of Applied Physics*, 104, 7, 2008.
- [90] C. Nie, R. Zhang, Z. L. Xie, X. Q. Xiu, B. Liu, D. Y. Fu, Q. J. Liu, P. Han, S. L. Gu, Y. Shi, and Y. D. Zheng, "Synthesis of [100] wurtzite InN nanowires and [011] zinc-blende InN nanorods", *Chinese Physics Letters*, 25, 5, 1780–1783, 2008.
- [91] S. Novikov, C. Staddon, C. Foxon, F. Luckert, P. Edwards, R. Martin, and A. Kent, "Molecular beam epitaxy as a method for the growth of free-standing bulk zinc-blende GaN and AlGaIn crystals", *Journal of Crystal Growth*, 323, 1, 80–83, 2011.
- [92] A. Barski, U. Rössner, J. L. Rouviere, and M. Arlery, "Epitaxial growth of cubic GaN and AlN on Si (001)", *Materials Research Society Internet Journal of Nitride Semiconductor Research*, 1, 1996.
- [93] E. Monroy, M. Hermann, E. Sarigiannidou, T. Andreev, P. Holliger, S. Monnoye, H. Mank, B. Daudin, and M. Eickhoff, "Polytype transition of N-face GaN:Mg from wurtzite to zinc-blende", *Journal of Applied Physics*, 96, 7, 3709–3715, 2004.

## References

---

- [94] S. V. Novikov, N. Zainal, A. V. Akimov, C. R. Staddon, A. J. Kent, and C. T. Foxon, “Molecular beam epitaxy as a method for the growth of freestanding zinc-blende (cubic) GaN layers and substrates”, *Journal of Vacuum Science & Technology B, Nanotechnology and Microelectronics: Materials, Processing, Measurement, and Phenomena*, 28, 3, C3B1–C3B6, 2010.
- [95] H. Okumura, S. Misawa, and S. Yoshida, “Epitaxial growth of cubic and hexagonal GaN on GaAs by gas-source molecular-beam epitaxy”, *Applied Physics Letters*, 59, 9, 1058–1060, 1991.
- [96] S. V. Novikov, N. Zainal, A. V. Akimov, C. R. Staddon, C. T. Foxon, A. J. Kent, G. Ferro, and P. Siffert, “Zinc-blende (Cubic) GaN and AlGaN Layers, Structures and Bulk Crystals by Molecular Beam Epitaxy”, vol. 154, 2010, 154–158.
- [97] Y. Taniyasu, K. Suzuki, D. H. Lim, A. W. Jia, M. Shimotomai, Y. Kato, M. Kobayashi, A. Yoshikawa, and K. Takahashi, “Cubic InGaN/GaN Double-Heterostructure Light Emitting Diodes Grown on GaAs (001) Substrates by MOVPE”, *Physica status solidi (A)*, 180, 1, 241–246, 2000.
- [98] S. Assali, I. Zardo, S. Plissard, D. Kriegner, M. A. Verheijen, G. Bauer, A. Meijerink, A. Belabbes, F. Bechstedt, J. E. M. Haverkort, and E. P. A. M. Bakkers, “Direct Band Gap Wurtzite Gallium Phosphide Nanowires”, *Nano Letters*, 13, 4, 1559–1563, 2013.
- [99] T. T. Vu, T. Zehender, M. A. Verheijen, S. R. Plissard, G. W. Immink, J. E. Haverkort, and E. P. A. M. Bakkers, “High optical quality single crystal phase wurtzite and zincblende InP nanowires”, *Nanotechnology*, 24, 11, 2013.
- [100] F. Ishizaka, Y. Hiraya, K. Tomioka, and T. Fukui, “Growth of wurtzite GaP in InP/GaP core-shell nanowires by selective-area MOVPE”, *Journal of Crystal Growth*, 411, 71–75, 2015.
- [101] J. Wallentin, M. E. Messing, E. Trygg, L. Samuelson, K. Deppert, and M. T. Borgström, “Growth of doped InAsP nanowires with InP shells”, *Journal of Crystal Growth*, 331, 1, 8–14, 2011.
- [102] F. Ishizaka, Y. Hiraya, K. Tomioka, J. Motohisa, and T. Fukui, “Growth and characterization of wurtzite InP/AlGaP core-multishell nanowires with AlGaP quantum well structures”, *Japanese Journal of Applied Physics*, 56, 1, 010311, 2017.
- [103] F. Ishizaka, Y. Hiraya, K. Tomioka, J. Motohisa, and T. Fukui, “Growth of All-Wurtzite InP/AlInP Core-Multishell Nanowire Array”, *Nano Letters*, 17, 3, 1350–1355, 2017.
- [104] L. Gagliano, A. Belabbes, M. Albani, S. Assali, M. A. Verheijen, L. Miglio, F. Bechstedt, J. E. Haverkort, and E. P. A. M. Bakkers, “Pseudodirect to Direct Compositional Crossover in Wurtzite GaP/InGaP Core-Shell Nanowires”, *Nano Letters*, 16, 12, 7930–7936, 2016.
- [105] Q. Gao, D. Saxena, F. Wang, L. Fu, S. Mokkapati, Y. Guo, L. Li, J. Wong-Leung, P. Caroff, H. H. Tan, and C. Jagadish, “Selective-Area Epitaxy of Pure Wurtzite InP Nanowires: High Quantum Efficiency and Room-Temperature Lasing”, *Nano Letters*, 14, 9, 5206–5211, 2014.

- 
- [106] L. Gagliano, M. Kruijsse, J. D. D. Schefold, A. Belabbes, M. A. Verheijen, S. Meuret, S. Koelling, A. Polman, F. Bechstedt, J. Haverkort, and E. P. A. M. Bakkers, “Efficient Green Emission from Wurtzite AlInP Nanowires”, *Nano Letters*, 18, 6, 3543–3549, 2018.
  - [107] A. Berg, P. Caroff, N. Shahid, M. N. Lockrey, X. Yuan, M. T. Borgström, H. H. Tan, and C. Jagadish, “Growth and optical properties of InGaP nanowires synthesized by selective-area epitaxy”, *Nano Research*, 10, 2, 672–682, 2017.
  - [108] N. Wang, X. Yuan, X. Zhang, Q. Gao, B. Zhao, L. Li, M. Lockrey, H. H. Tan, C. Jagadish, and P. Caroff, “Shape Engineering of InP Nanostructures by Selective Area Epitaxy”, *ACS Nano*, 13, 6, 7261–7269, 2019.
  - [109] Y. Hiraya, F. Ishizaka, K. Tomioka, and T. Fukui, “Crystal phase transition to green emission wurtzite AlInP by crystal structure transfer”, *Applied Physics Express*, 9, 3, 035502, 2016.
  - [110] G. Zhang, K. Tateno, H. Sanada, T. Sogawa, and H. Nakano, “AlAs/GaAs/GaP Heterostructure Nanowires Grown on Si Substrate”, in *2007 IEEE 19th International Conference on Indium Phosphide & Related Materials*, IEEE, 2007, 388–391.
  - [111] S. Lehmann, D. Jacobsson, K. Deppert, and K. A. Dick, “High crystal quality wurtzite-zinc blende heterostructures in metal-organic vapor phase epitaxy-grown GaAs nanowires”, *Nano Research*, 5, 7, 470–476, 2012.
  - [112] K. A. Dick, C. Thelander, L. Samuelson, and P. Caroff, “Crystal phase engineering in single InAs nanowires”, *Nano Letters*, 10, 9, 3494–3499, 2010.
  - [113] R. Popovitz-Biro, A. Kretinin, P. Von Huth, and H. Shtrikman, “InAs/GaAs core-shell nanowires”, *Crystal Growth and Design*, 11, 9, 3858–3865, 2011.
  - [114] P. Mohan, J. Motohisa, and T. Fukui, “Realization of conductive InAs nanotubes based on lattice-mismatched InP/InAs core-shell nanowires”, *Applied Physics Letters*, 88, 1, 013110, 2006.
  - [115] M. Moewe, L. C. Chuang, S. Crankshaw, C. Chase, and C. J. Chang-Hasnain, “Atomically sharp catalyst-free wurtzite GaAs/AlGaAs nanoneedles grown on silicon”, *Applied Physics Letters*, 93, 2, 023116, 2008.
  - [116] X. Li, K. Zhang, J. Treu, L. Stampfer, G. Koblmüller, F. Toor, and J. P. Prineas, “Contactless Optical Characterization of Carrier Dynamics in Free-Standing InAs-InAlAs Core-Shell Nanowires on Silicon”, *Nano Letters*, 2019.
  - [117] M. Heurlin, T. Stankevič, S. Mickevičius, S. Yngman, D. Lindgren, A. Mikkelsen, R. Feidenhans'l, M. T. Borgström, and L. Samuelson, “Structural Properties of Wurtzite InP–InGaAs Nanowire Core–Shell Heterostructures”, *Nano Letters*, 15, 4, 2462–2467, 2015.
  - [118] J. N. Shapiro, A. Lin, C. Ratsch, and D. L. Huffaker, “Temperature dependence of stacking faults in catalyst-free GaAs nanopillars”, *Nanotechnology*, 24, 47, 475601, 2013.

## References

---

- [119] K. Tomioka, J. Motohisa, S. Hara, and T. Fukui, “Crystallographic Structure of InAs Nanowires Studied by Transmission Electron Microscopy”, *Japanese Journal of Applied Physics*, 46, No. 45, L1102–L1104, 2007.
- [120] J. C. Shin, K. H. Kim, K. J. Yu, H. Hu, L. Yin, C.-Z. Ning, J. A. Rogers, J.-M. Zuo, and X. Li, “InGaAs Nanowires on Silicon: One-Dimensional Heterogeneous Epitaxy, Bandgap Engineering, and Photovoltaics”, *Nano Letters*, 11, 11, 4831–4838, 2011.
- [121] B. Mandl, K. A. Dick, D. Kriegner, M. Keplinger, G. Bauer, J. Stangl, and K. Deppert, “Crystal structure control in Au-free self-seeded InSb wire growth”, *Nanotechnology*, 22, 14, 145603, 2011.
- [122] M. Pozuelo, H. Zhou, S. Lin, S. A. Lipman, M. S. Goorsky, R. F. Hicks, and S. Kodambaka, “Self-catalyzed growth of InP/InSb axial nanowire heterostructures”, *Journal of Crystal Growth*, 329, 1, 6–11, 2011.
- [123] S. Gorji Ghalamestani, S. Lehmann, and K. A. Dick, “Can antimonide-based nanowires form wurtzite crystal structure?”, *Nanoscale*, 8, 5, 2778–2786, 2016.
- [124] D. Anandan, V. Nagarajan, R. K. Kakkerla, H. W. Yu, H. L. Ko, S. K. Singh, C. T. Lee, and E. Y. Chang, “Crystal phase control in self-catalyzed InSb nanowires using basic growth parameter V/III ratio”, *Journal of Crystal Growth*, 522, 30–36, 2019.
- [125] H. Kindlund, R. R. Zamani, A. R. Persson, S. Lehmann, L. R. Wallenberg, and K. A. Dick, “Kinetic Engineering of Wurtzite and Zinc-Blende AlSb Shells on InAs Nanowires”, *Nano Letters*, 18, 9, 5775–5781, 2018.
- [126] L. Namazi, L. Gren, M. Nilsson, M. Garbrecht, C. Thelander, R. R. Zamani, and K. A. Dick, “Realization of Wurtzite GaSb Using InAs Nanowire Templates”, *Advanced Functional Materials*, 28, 28, 1–13, 2018.
- [127] C. Himwas, S. Collin, H. L. Chen, G. Patriarche, F. Oehler, L. Travers, O. Saket, F. H. Julien, J. C. Harmand, and M. Tchernycheva, “Correlated optical and structural analyses of individual GaAsP/GaP core-shell nanowires”, *Nanotechnology*, 30, 30, 2019.
- [128] H. Zhou, M. Pozuelo, R. F. Hicks, and S. Kodambaka, “Self-catalyzed vapor–liquid–solid growth of InPSb nanostructures”, *Journal of Crystal Growth*, 319, 1, 25–30, 2011.
- [129] M. Tchernycheva, G. E. Cirlin, G. Patriarche, L. Travers, V. Zwiller, U. Perinetti, and J. C. Harmand, “Growth and characterization of InP nanowires with InAsP insertions”, *Nano Letters*, 7, 6, 1500–1504, 2007.
- [130] T. Xu, K. A. Dick, S. Plissard, T. H. Nguyen, Y. Makoudi, M. Berthe, J. P. Nys, X. Wallart, B. Grandidier, and P. Caroff, “Faceting, composition and crystal phase evolution in IIIV antimonide nanowire heterostructures revealed by combining microscopy techniques”, *Nanotechnology*, 23, 9, 2012.
- [131] P. K. Mohseni, C. Maunders, G. A. Botton, and R. R. LaPierre, “GaP/GaAsP/GaP core-multishell nanowire heterostructures on (111) silicon”, *Nanotechnology*, 18, 44, 445304, 2007.

- 
- [132] H. Li, J. Tang, G. Pang, D. Wang, X. Fang, R. Chen, and Z. Wei, "Optical characteristics of GaAs/GaAsSb/GaAs coaxial single quantum-well nanowires with different Sb components", *RSC Advances*, 9, 65, 38114–38118, 2019.
- [133] C. Thelander, P. Caroff, S. Plissard, and K. A. Dick, "Electrical properties of InAsSb and InSb nanowires grown by molecular beam epitaxy", *Applied Physics Letters*, 100, 23, 232105, 2012.
- [134] A. Fontcuberta i Morral, J. Arbiol, J. D. Prades, A. Cirera, and J. R. Morante, "Synthesis of Silicon Nanowires with Wurtzite Crystalline Structure by Using Standard Chemical Vapor Deposition", *Advanced Materials*, 19, 10, 1347–1351, 2007.
- [135] J.-L. Maurice, J. Tang, I. Florea, F. Fossard, P. Roca i Cabarrocas, E. V. Johnson, and M. Foldyna, "TEM characterisation of diamond-hexagonal silicon nanowires", in *European Microscopy Congress 2016: Proceedings*, Weinheim, Germany: Wiley-VCH Verlag GmbH & Co. KGaA, 2016, 488–489.
- [136] F. J. Lopez, E. R. Hemesath, and L. J. Lauhon, "Ordered Stacking Fault Arrays in Silicon Nanowires", *Nano Letters*, 9, 7, 2774–2779, 2009.
- [137] C. Cayron, M. Den Hertog, L. Latu-Romain, C. Mouchet, C. Secouard, J.-L. Rouviere, E. Rouviere, and J.-P. Simonato, "Odd electron diffraction patterns in silicon nanowires and silicon thin films explained by microtwins and nanotwins", *Journal of Applied Crystallography*, 42, 2, 242–252, 2009.
- [138] N. Jeon, S. A. Dayeh, and L. J. Lauhon, "Origin of Polytype Formation in VLS-Grown Ge Nanowires through Defect Generation and Nanowire Kinking", *Nano Letters*, 13, 8, 3947–3952, 2013.
- [139] S. Biswas, S. Barth, and J. D. Holmes, "Inducing imperfections in germanium nanowires", *Nano Research*, 10, 5, 1510–1523, 2017.
- [140] S. Biswas, J. Doherty, D. Majumdar, T. Ghoshal, K. Rahme, M. Conroy, A. Singha, M. A. Morris, and J. D. Holmes, "Diameter-Controlled Germanium Nanowires with Lamellar Twinning and Polytypes", *Chemistry of Materials*, 27, 9, 3408–3416, 2015.
- [141] H. I. T. Hauge, M. A. Verheijen, S. Conesa-Boj, T. Etzelstorfer, M. Watzinger, D. Kriegner, I. Zardo, C. Fasolato, F. Capitani, P. Postorino, S. Kölling, A. Li, S. Assali, J. Stangl, and E. P. A. M. Bakkers, "Hexagonal Silicon Realized", *Nano Letters*, 15, 9, 5855–5860, 2015.
- [142] E. C. Garnett, M. L. Brongersma, Y. Cui, and M. D. McGehee, "Nanowire Solar Cells", *Annual Review of Materials Research*, 41, 1, 269–295, 2011.
- [143] Z. Fan and J. G. Lu, "Gate-refreshable nanowire chemical sensors", *Applied Physics Letters*, 86, 12, 123510, 2005.
- [144] S. Gazibegovic, D. Car, H. Zhang, S. C. Balk, J. A. Logan, M. W. A. de Moor, M. C. Cassidy, R. Schmits, D. Xu, G. Wang, P. Krogstrup, R. L. M. Op het Veld, K. Zuo, Y. Vos, J. Shen, D. Bouman, B. Shojaei, D. Pennachio, J. S. Lee, P. J. van Veldhoven, S. Koelling, M. A. Verheijen, L. P. Kouwenhoven, C. J. Palmstrøm, and E. P. A. M. Bakkers, "Epitaxy of advanced nanowire quantum devices", *Nature*, 548, 7668, 434–438, 2017.

## References

---

- [145] S. Adachi, *Properties of semiconductor alloys: group-IV, III-V and II-VI semiconductors*. John Wiley & Sons, 2009, vol. 28.
- [146] Y. Zhang, Z. Iqbal, S. Vijayalakshmi, and H. Grebel, “Stable hexagonal-wurtzite silicon phase by laser ablation”, *Applied Physics Letters*, 75, 18, 2758–2760, 1999.
- [147] B. E. Smith, X. Zhou, P. B. Roder, E. H. Abramson, and P. J. Pauzauskie, “Recovery of hexagonal Si-IV nanowires from extreme GPa pressure”, *Journal of Applied Physics*, 119, 18, 10–14, 2016.
- [148] G. L. Harris, *Properties of silicon carbide*, 13. Iet, 1995.
- [149] F. Keffer and A. M. Portis, “Study of the Wurtzite-Type Binary Compounds. II. Macroscopic Theory of the Distortion and Polarization”, *The Journal of Chemical Physics*, 27, 3, 675–682, 1957.
- [150] H. Schulz and K. H. Thiemann, “Crystal structure refinement of AlN and GaN”, *Solid State Communications*, 23, 11, 815–819, 1977.
- [151] F. Bernardini, V. Fiorentini, and D. Vanderbilt, “Spontaneous polarization and piezoelectric constants of III-V nitrides”, *Physical Review B - Condensed Matter and Materials Physics*, 56, 16, R10024–R10027, 1997.
- [152] S. H. Park and S. L. Chuang, “Comparison of zinc-blende and wurtzite GaN semiconductors with spontaneous polarization and piezoelectric field effects”, *Journal of Applied Physics*, 87, 1, 353–364, 2000.
- [153] A. Schliwa, G. Martin, and O. Hönig, *Multi-Band Effective Mass Approximations*, M. Ehrhardt and T. Koprucki, Eds., ser. Lecture Notes in Computational Science and Engineering May 2015. Cham: Springer International Publishing, 2014, vol. 94, 1–25.
- [154] J. W. Morris Jr, *A Survey of Materials Science - I. Structure*. 2007.
- [155] J. Li, D. Wang, and R. R. LaPierre, *Advances in III-V semiconductor nanowires and nanodevices*. Bentham Science Publishers, 2011.
- [156] S. M. Sze and K. K. Ng, *Physics of semiconductor devices*. John Wiley & Sons, 2006.
- [157] K. E. Ismail and F. Stern, *Complementary metal-oxide semiconductor transistor logic using strained Si/SiGe heterostructure layers*, 1996.
- [158] M. L. Lee, E. A. Fitzgerald, M. T. Bulsara, M. T. Currie, and A. Lochtefeld, “Strained Si, SiGe, and Ge channels for high-mobility metal-oxide-semiconductor field-effect transistors”, *Journal of Applied Physics*, 97, 1, 011101, 2005.
- [159] D. P. Bour, D. W. Treat, K. J. Beernink, B. S. Krusor, R. S. Geels, and D. F. Welch, “610-nm band AlGaInP single quantum well laser diode”, *IEEE photonics technology letters*, 6, 2, 128–131, 1994.
- [160] G. Signorello, S. Karg, M. T. Björk, B. Gotsmann, and H. Riel, “Tuning the Light Emission from GaAs Nanowires over 290 meV with Uniaxial Strain”, *Nano Letters*, 13, 3, 917–924, 2013.

- 
- [161] J. Greil, S. Assali, Y. Isono, A. Belabbes, F. Bechstedt, F. O. Valega Mackenzie, A. Y. Silov, E. P. A. M. Bakkers, and J. E. M. Haverkort, “Optical Properties of Strained Wurtzite Gallium Phosphide Nanowires”, *Nano Letters*, 16, 6, 3703–3709, 2016.
  - [162] G. Signorello, “Uniaxial Stress Effects in Zincblende and Wurtzite GaAs Nanowires : an Optical Spectroscopy Study”, *Doctoral Thesis*, 2013.
  - [163] L. W. James, J. P. Van Dyke, F. Herman, and D. M. Chang, “Band structure and high-field transport properties of InP”, *Physical Review B*, 1, 10, 3998–4004, 1970.
  - [164] J. C. Phillips, “Energy-band interpolation scheme based on a pseudopotential”, *Physical Review*, 112, 3, 685–695, 1958.
  - [165] I. Gorczyca, P. Pfeffer, and W. Zawadzki, “Pseudopotential and k.p band parameters for GaAs, InP and InSb”, *Semiconductor Science and Technology*, 6, 10, 963–968, 1991.
  - [166] Y. S. Kim, M. Marsman, G. Kresse, F. Tran, and P. Blaha, “Towards efficient band structure and effective mass calculations for III-V direct band-gap semiconductors”, *Physical Review B - Condensed Matter and Materials Physics*, 82, 20, 1–11, 2010.
  - [167] P. Németh, L. A. J. Garvie, T. Aoki, N. Dubrovinskaia, L. Dubrovinsky, and P. R. Buseck, “Lonsdaleite is faulted and twinned cubic diamond and does not exist as a discrete material”, *Nature Communications*, 5, 1, 5447, 2014.
  - [168] F. Bechstedt and A. Belabbes, “Structure, energetics, and electronic states of III-V compound polytypes”, *Journal of Physics Condensed Matter*, 25, 27, 2013.
  - [169] K. Li, H. Sun, F. Ren, K. W. Ng, T.-T. D. Tran, R. Chen, and C. J. Chang-Hasnain, “Tailoring the Optical Characteristics of Microsized InP Nanoneedles Directly Grown on Silicon”, *Nano Letters*, 14, 1, 183–190, 2014.
  - [170] M. Murayama and T. Nakayama, “Chemical trend of band offsets at wurtzite/zincblende heterocrystalline semiconductor interfaces”, *Physical Review B*, 49, 7, 4710–4724, 1994.
  - [171] L. Zhang, J. W. Luo, A. Zunger, N. Akopian, V. Zwiller, and J. C. Harmand, “Wide InP Nanowires with wurtzite/zincblende superlattice segments are type-II whereas narrower nanowires become type-I: An atomistic pseudopotential calculation”, *Nano Letters*, 10, 10, 4055–4060, 2010.
  - [172] M. De Luca and A. Polimeni, “Electronic properties of wurtzite-phase InP nanowires determined by optical and magneto-optical spectroscopy”, *Applied Physics Reviews*, 4, 4, 041102, 2017.
  - [173] T. Akiyama, K. Nakamura, and T. Ito, “Structural stability and electronic structures of InP nanowires: Role of surface dangling bonds on nanowire facets”, *Phys. Rev. B*, 73, 23, 235308, 2006.
  - [174] Freeman, C. H. Park, B.-H. Cheong, K.-H. Lee, and K.-J. Chang, “Structural and electronic properties of cubic, 2H, 4H, and 6H SiC”, *Physical Review B*, 49, 7, 4485, 1994.
  - [175] A. F. Wright and J. S. Nelson, “Consistent structural properties for AlN, GaN, and InN”, *Physical Review B*, 51, 12, 7866, 1995.

## References

---

- [176] T. Kaewmaraya, L. Vincent, and M. Amato, “Accurate Estimation of Band Offsets in Group IV Polytype Junctions: A First-Principles Study”, *The Journal of Physical Chemistry C*, 121, 10, 5820–5828, 2017.
- [177] L. Gasca, “From O to L: The Future of Optical-Wavelength Bands”, *Broadband Properties*, 83–85, 2008.
- [178] P. Capper, S. Irvine, and T. Joyce, “Epitaxial crystal growth: methods and materials”, in *Springer Handbook of Electronic and Photonic Materials*, Springer, 2017, 1.
- [179] P. Capper and M. Mauk, *Liquid phase epitaxy of electronic, optical and optoelectronic materials*. John Wiley & Sons, 2007, vol. 21.
- [180] R. F. C. Farrow, S. S. P. Parkin, P. J. Dobson, J. H. Neave, and A. S. Arrott, *Thin film growth techniques for low-dimensional structures*. Springer Science & Business Media, 2013, vol. 163.
- [181] M. Borg, “Antimonide Heterostructure Nanowires - Growth, Physics and Devices”, *Doctoral Thesis*, 2012.
- [182] J. Sijia, “Selective Area Growth of III/V Compounds on Si Substrates using Metal-Organic Vapor Phase Epitaxy”, *Doctoral Thesis*, 2015.
- [183] N. Buchan, C. Larsen, and G. Stringfellow, “Mass spectrometric studies of trimethyl-indium pyrolysis”, *Journal of Crystal Growth*, 92, 3-4, 591–604, 1988.
- [184] S. H. Li, C. A. Larsen, N. I. Buchan, and G. B. Stringfellow, “Pyrolysis of tertiarybutylphosphine”, *Journal of Electronic Materials*, 18, 3, 457–464, 1989.
- [185] A. Stegmüller, P. Rosenow, and R. Tonner, “A quantum chemical study on gas phase decomposition pathways of triethylgallane (TEG, Ga(C<sub>2</sub>H<sub>5</sub>)<sub>3</sub>) and tert-butylphosphine (TBP, PH<sub>2</sub>(t-C<sub>4</sub>H<sub>9</sub>)) under MOVPE conditions”, *Physical Chemistry Chemical Physics*, 16, 32, 17018–17029, 2014.
- [186] G. Fan, R. Hoare, M. Pemble, I. Povey, A. Taylor, and J. Williams, “Gas phase monitoring of reactions under InP MOVPE growth conditions for the decomposition of tertiary-butyl phosphine and related precursors”, *Journal of Crystal Growth*, 124, 1-4, 49–55, 1992.
- [187] M. Masi, C. Cavallotti, G. Radaelli, and S. Carrà, “Kinetics of Indium Phosphide Epitaxial Growth Using Metal Organic Precursors”, *Crystal Research and Technology*, 32, 8, 1125–1136, 1997.
- [188] M. Sugiyama, K. Kusunoki, Y. Shimogaki, S. Sudo, Y. Nakano, H. Nagamoto, K. Sugawara, K. Tada, and H. Komiyama, “Kinetic studies on thermal decomposition of MOVPE sources using fourier transform infrared spectroscopy”, *Applied Surface Science*, 117-118, 97, 746–752, 1997.
- [189] L. Nattermann, O. Maßmeyer, E. Sterzer, V. Derpmann, H. Y. Chung, W. Stolz, and K. Volz, “An experimental approach for real time mass spectrometric CVD gas phase investigations”, *Scientific Reports*, 8, 1, 319, 2018.

- 
- [190] G. B. Stringfellow, *Organometallic vapor-phase epitaxy: theory and practice*. Elsevier, 1999.
- [191] D. B. Holt, "Surface polarity and symmetry in semiconducting compounds", *Journal of materials science*, 23, 3, 1131–1136, 1988.
- [192] M. de la Mata, R. R. Zamani, S. Martí-Sánchez, M. Eickhoff, Q. Xiong, A. Fontcuberta i Morral, P. Caroff, and J. Arbiol, "The Role of Polarity in Nonplanar Semiconductor Nanostructures", *Nano Letters*, 19, 6, 3396–3408, 2019.
- [193] A. Paszuk, S. Brückner, M. Steidl, W. Zhao, A. Dobrich, O. Supplie, P. Kleinschmidt, W. Prost, and T. Hannappel, "Controlling the polarity of metalorganic vapor phase epitaxy-grown GaP on Si(111) for subsequent III-V nanowire growth", *Applied Physics Letters*, 106, 23, 231601, 2015.
- [194] D. Jacobsson, F. Yang, K. Hillerich, F. Lenrick, S. Lehmann, D. Kriegner, J. Stangl, L. R. Wallenberg, K. A. Dick, and J. Johansson, "Phase Transformation in Radially Merged Wurtzite GaAs Nanowires", *Crystal Growth & Design*, 15, 10, 4795–4803, 2015.
- [195] K. D. Sattler, *Handbook of Nanophysics - Nanotubes and Nanowires*. CRC Press, 2011, 731.
- [196] P. Krogstrup, R. Popovitz-Biro, E. Johnson, M. H. Madsen, J. Nygård, and H. Shtrikman, "Structural phase control in self-catalyzed growth of GaAs nanowires on silicon (111)", *Nano Letters*, 10, 11, 4475–4482, 2010.
- [197] S. Schulz, M. Schwartz, A. Kuczkowski, and W. Assenmacher, "Self-catalyzed growth of GaSb nanowires at low reaction temperatures", *Journal of Crystal Growth*, 312, 9, 1475–1480, 2010.
- [198] W. Kim, V. G. Dubrovskii, J. Vukajlovic-Plestina, G. Tütüncüoğlu, L. Francaviglia, L. Güniat, H. Potts, M. Friedl, J.-B. Lèran, and A. Fontcuberta i Morral, "Bi-stability of contact angle and its role in achieving quantum-thin self-assisted GaAs nanowires", *Nano Letters*, acs.nanolett.7b03126, 2017.
- [199] J. Tersoff, "Stable Self-Catalyzed Growth of III-V Nanowires", *Nano Letters*, 15, 10, 6609–6613, 2015.
- [200] G. Dhanaraj, K. Byrappa, V. Prasad, and M. Dudley, *Springer handbook of crystal growth*. Springer Science & Business Media, 2010.
- [201] K. Tomioka, K. Ikejiri, T. Tanaka, J. Motohisa, S. Hara, K. Hiruma, and T. Fukui, "Selective-area growth of III-V nanowires and their applications", *Journal of Materials Research*, 26, 17, 2127–2141, 2011.
- [202] K. Tomioka, Y. Kobayashi, J. Motohisa, S. Hara, and T. Fukui, "Selective-area growth of vertically aligned GaAs and GaAs/AlGaAs core-shell nanowires on Si(111) substrate", *Nanotechnology*, 20, 14, 145302, 2009.
- [203] K. Tomioka, J. Motohisa, S. Hara, and T. Fukui, "Control of InAs nanowire growth directions on Si", *Nano Letters*, 8, 10, 3475–3480, 2008.

## References

---

- [204] K. Ikejiri, T. Sato, H. Yoshida, K. Hiruma, J. Motohisa, S. Hara, and T. Fukui, "Growth characteristics of GaAs nanowires obtained by selective area metal–organic vapour-phase epitaxy", *Nanotechnology*, 19, 26, 265604, 2008.
- [205] P. Mohan, J. Motohisa, and T. Fukui, "Controlled growth of highly uniform, axial/radial direction-defined, individually addressable InP nanowire arrays", *Nanotechnology*, 16, 12, 2903–2907, 2005.
- [206] W. Choi, S. Fan, P. Mohseni, M. L. Lee, and X. Li, "Selective area epitaxy of GaP nanowire array on Si (111) by MOCVD", *2019 Compound Semiconductor Week (CSW)*, 111, 1–2, 2019.
- [207] K. Tomioka, P. Mohan, J. Noborisaka, S. Hara, J. Motohisa, and T. Fukui, "Growth of highly uniform InAs nanowire arrays by selective-area MOVPE", *Journal of Crystal Growth*, 298, 644–647, 2007.
- [208] K. Choi, M. Arita, and Y. Arakawa, "Selective-area growth of thin GaN nanowires by MOCVD", *Journal of Crystal Growth*, 357, 58–61, 2012.
- [209] V. Consonni, E. Sarigiannidou, E. Appert, A. Bocheux, S. Guillemin, F. Donatini, I. C. Robin, J. Kioseoglou, and F. Robaut, "Selective area growth of well-ordered ZnO nanowire arrays with controllable polarity", *ACS Nano*, 8, 5, 4761–4770, 2014.
- [210] L. Yang, J. Motohisa, J. Takeda, K. Tomioka, and T. Fukui, "Selective-area growth of hexagonal nanopillars with single InGaAs/GaAs quantum wells on GaAs(111)B substrate and their temperature-dependent photoluminescence", *Nanotechnology*, 18, 10, 105302, 2007.
- [211] A. Hayashida, T. Sato, S. Hara, J. Motohisa, K. Hiruma, and T. Fukui, "Fabrication and characterization of GaAs quantum well buried in AlGaAs/GaAs heterostructure nanowires", *Journal of Crystal Growth*, 312, 24, 3592–3598, 2010.
- [212] H. Sasakura, H. Kumano, I. Suemune, J. Motohisa, Y. Kobayashi, M. Van Kouwen, K. Tomioka, T. Fukui, N. Akopian, and V. Zwiller, "Exciton coherence in clean single InP/InAsP/InP nanowire quantum dots emitting in infra-red measured by Fourier spectroscopy", *Journal of Physics: Conference Series*, 193, 20–24, 2009.
- [213] L. E. Jensen, M. T. Björk, S. Jeppesen, A. I. Persson, B. J. Ohlsson, and L. Samuelson, "Role of Surface Diffusion in Chemical Beam Epitaxy of InAs Nanowires", *Nano Letters*, 4, 10, 1961–1964, 2004.
- [214] G. Wang, M. R. Leys, N. D. Nguyen, R. Loo, G. Brammertz, O. Richard, H. Bender, J. Dekoster, M. Meuris, M. M. Heyns, and M. Caymax, "Growth of high quality InP layers in STI trenches on miscut Si (0 0 1) substrates", *Journal of Crystal Growth*, 315, 1, 32–36, 2011.
- [215] B. Kunert, W. Guo, Y. Mols, R. Langer, and K. Barla, "Integration of III/V Hetero-Structures By Selective Area Growth on Si for Nano- and Optoelectronics", *{ECS} Transactions*, 75, 8, 409–419, 2016.

- [216] G. Wang, M. R. Leys, N. D. Nguyen, R. Loo, G. Brammertz, O. Richard, H. Bender, J. Dekoster, M. Meuris, M. M. Heyns, and M. Caymax, "Selective Area Growth of InP in Shallow-Trench-Isolated Structures on Off-Axis Si(001) Substrates", *Journal of The Electrochemical Society*, 157, 11, H1023, 2010.
- [217] B. Korgel and R. F. Hicks, "A diffusion model for selective-area epitaxy by metalorganic chemical vapor deposition", *Journal of crystal growth*, 151, 1-2, 204–212, 1995.
- [218] T. Ujihara, Y. Yoshida, W. S. Lee, and Y. Takeda, "Pattern size effect on source supply process for sub-micrometer scale selective area growth by organometallic vapor phase epitaxy", *Journal of crystal growth*, 289, 1, 89–95, 2006.
- [219] Q. Gao, V. G. Dubrovskii, P. Caroff, J. Wong-Leung, L. Li, Y. Guo, L. Fu, H. H. Tan, and C. Jagadish, "Simultaneous Selective-Area and Vapor-Liquid-Solid Growth of InP Nanowire Arrays", *Nano Letters*, 16, 7, 4361–4367, 2016.
- [220] A. I. Persson, L. E. Fröberg, S. Jeppesen, M. T. Björk, and L. Samuelson, "Surface diffusion effects on growth of nanowires by chemical beam epitaxy", *Journal of Applied Physics*, 101, 3, 2007.
- [221] J. Seidl, J. G. Gluschke, X. Yuan, S. Naureen, N. Shahid, H. H. Tan, C. Jagadish, A. P. Micolich, and P. Caroff, "Regaining a Spatial Dimension: Mechanically Transferrable Two-Dimensional InAs Nanofins Grown by Selective Area Epitaxy", *Nano Letters*, 19, 7, 4666–4677, 2019.
- [222] M. Albani, L. Ghisalberti, R. Bergamaschini, M. Friedl, M. Salvalaglio, A. Voigt, F. Montalenti, G. Tütüncüoğlu, A. Fontcuberta i Morral, and L. Miglio, "Growth kinetics and morphological analysis of homoepitaxial GaAs fins by theory and experiment", *Physical Review Materials*, 2, 9, 1–10, 2018.
- [223] Z. Yang, A. Surrente, G. Tutuncuoglu, K. Galkowski, M. Cazaban-Carrazé, F. Amaduzzi, P. Leroux, D. K. Maude, A. Fontcuberta i Morral, and P. Plochocka, "Revealing Large-Scale Homogeneity and Trace Impurity Sensitivity of GaAs Nanoscale Membranes", *Nano Letters*, 17, 5, 2979–2984, 2017.
- [224] Z. Yan, Y. Hamaoka, S. Naritsuka, and T. Nishinaga, "Coalescence in microchannel epitaxy of InP", *Journal of crystal growth*, 212, 1-2, 1–10, 2000.
- [225] Z. R. Zytewicz, "Epitaxial Lateral Overgrowth of GaAs: Principle and Growth Mechanism", *Crystal Research and Technology*, 34, 5, 573–582, 1999.
- [226] S. Naritsuka and T. Nishinaga, "Epitaxial lateral overgrowth of InP by liquid phase epitaxy", *Journal of crystal growth*, 146, 1-4, 314–318, 1995.
- [227] R. Bergmann, E. Bauser, and J. H. Werner, "Defect-free epitaxial lateral overgrowth of oxidized (111) Si by liquid phase epitaxy", *Applied physics letters*, 57, 4, 351–353, 1990.
- [228] T. Nishinaga, T. Nakano, and S. Zhang, "Epitaxial Lateral Overgrowth of GaAs by LPE", *Japanese Journal of Applied Physics*, 27, Part 2, No. 6, L964–L967, 1988.

## References

---

- [229] Y. Suzuki and T. Nishinaga, "Epitaxial Lateral Overgrowth of Si by LPE with Sn Solution and Its Orientation Dependence", *Japanese Journal of Applied Physics*, 28, Part 1, No. 3, 440–445, 1989.
- [230] M. Shichijo, R. Nakane, S. Sugahara, and S. Takagi, "Fabrication of III-V on insulator structures on Si using microchannel epitaxy with a two-step growth technique", *Japanese Journal of Applied Physics*, 46, 9A, 5930–5934, 2007.
- [231] G. Bacchin and T. Nishinaga, "A new way to achieve both selective and lateral growth by molecular beam epitaxy: low angle incidence microchannel epitaxy", *Journal of crystal growth*, 208, 1-4, 1–10, 2000.
- [232] T. Nishinaga, "Microchannel epitaxy: an overview", *Journal of crystal growth*, 237, 1410–1417, 2002.
- [233] Y. S. Chang, S. Naritsuka, and T. Nishinaga, "Optimization of growth condition for wide dislocation-free GaAs on Si substrate by microchannel epitaxy", *Journal of crystal growth*, 192, 1-2, 18–22, 1998.
- [234] Z. Yan, S. Naritsuka, and T. Nishinaga, "Interface supersaturation in microchannel epitaxy of InP", *Journal of crystal growth*, 203, 1-2, 25–30, 1999.
- [235] P. Vennéguès, B. Beaumont, V. Bousquet, M. Vaille, and P. Gibart, "Reduction mechanisms for defect densities in GaN using one- or two-step epitaxial lateral overgrowth methods", *Journal of Applied Physics*, 87, 9 I, 4175–4181, 2000.
- [236] S. Naritsuka, "Microchannel epitaxy of III–V layers on Si substrates", *Future Directions in Silicon Photonics*, 101, 139–161, 2019.
- [237] W. Huang, T. Nishinaga, and S. Naritsuka, "Microchannel epitaxy of GaAs from parallel and nonparallel seeds", *Japanese Journal of Applied Physics*, 40, 9R, 5373–5376, 2001.
- [238] T. Kochiya, Y. Oyama, T. Kimura, K. Suto, and J.-i. Nishizawa, "Dislocation-free large area InP ELO layers by liquid phase epitaxy", *Journal of crystal growth*, 281, 2-4, 263–274, 2005.
- [239] N. Julian, P. Mages, C. Zhang, J. Zhang, S. Kraemer, S. Stemmer, S. Denbaars, L. Coldren, P. Petroff, and J. Bowers, "Coalescence of InP Epitaxial Lateral Overgrowth by MOVPE with V/III Ratio Variation", *Journal of Electronic Materials*, 41, 5, 845–852, 2012.
- [240] A. Ogura and Y. Fujimoto, "Novel technique for Si epitaxial lateral overgrowth: Tunnel epitaxy", *Applied Physics Letters*, 55, 21, 2205–2207, 1989.
- [241] A. Ogura and Y. Fujimoto, "Extremely thin and defect-free Si-on-insulator fabrication by tunnel epitaxy", *Applied Physics Letters*, 57, 26, 2806–2807, 1990.
- [242] A. Ogura, "50-nm-Thick Silicon-on-Insulator Fabrication by Advanced Epitaxial Lateral Overgrowth: Tunnel Epitaxy", *Journal of The Electrochemical Society*, 140, 4, 1125, 1993.
- [243] P. Schubert and G. Neudeck, "Confined lateral selective epitaxial growth of silicon for device fabrication", *IEEE Electron Device Letters*, 11, 5, 181–183, 1990.
- [244] P. J. Schubert, *Confined lateral selective epitaxial growth*, 1990.

- 
- [245] P. J. Schubert and G. W. Neudeck, "Vertical Bipolar Transistors Fabricated in Local Silicon on Insulator Films Prepared Using Confined Lateral Selective Epitaxial Growth (CLSEG)", *IEEE Transactions on Electron Devices*, 37, 11, 2336–2342, 1990.
- [246] D. Pribat, L. Karapiperis, and C. Collet, "Conformal vapor phase epitaxy", *Applied Physics Letters*, 55, 24, 2544–2546, 1989.
- [247] P. Pengpad, K. Osman, N. S. Lloyd, J. M. Bonar, P. Ashburn, H. A. Kemhadjian, J. S. Hamel, and D. M. Bagnall, "Lateral SiGe heterojunction bipolar transistor by confined selective epitaxial growth: simulation and material growth", *Microelectronic engineering*, 73, 508–513, 2004.
- [248] D. Pribat, C. Collet, P. Legagneux, and L. Karapiperis, "Conformal vapor phase growth of submicron thick (100) GaAs films", *Applied Physics Letters*, 56, 20, 2007–2009, 1990.
- [249] D. Pribat, B. Gerard, M. Dupuy, and P. Legagneux, "High quality GaAs on Si by conformal growth", *Applied Physics Letters*, 60, 17, 2144–2146, 1992.
- [250] O. Parillaud, N. Piffault, E. Gil-Lafon, R. Cadoret, B. Gerard, D. Pribat, L. C. D. Recherche, and D. D. Corbeville, "Defect-free InP films on Si substrates obtained by hydride vapor phase conformal growth", in *Proceedings of 1994 IEEE 6th International Conference on Indium Phosphide and Related Materials (IPRM)*, IEEE, 1994, 547–550.
- [251] N. Piffault, O. Parillaud, E. Gil-Hafon, J. Leymarie, A. M. Vasson, A. M. Vasson, R. Cadoret, B. Gerard, D. Pribat, L. C. D. Recherche, and D. D. Corbeville, "Assessment of the strain of InP films on Si obtained by HVPE conformal growth", in *Proceedings of 1994 IEEE 6th International Conference on Indium Phosphide and Related Materials (IPRM)*, IEEE, 1994, 155–158.
- [252] L. Czornomaz, E. Uccelli, M. Sousa, V. Deshpande, V. Djara, D. Caimi, M. D. Rossell, R. Erni, and J. Fompeyrine, "Confined Epitaxial Lateral Overgrowth (CELO): A novel concept for scalable integration of CMOS-compatible InGaAs-on-insulator MOSFETs on large-area Si substrates", *Digest of Technical Papers - Symposium on VLSI Technology*, T172–T173, 2015.
- [253] H. Schmid, M. Borg, K. Moselund, L. Gignac, C. M. Breslin, J. Bruley, D. Cutaia, and H. Riel, "Template-assisted selective epitaxy of III–V nanoscale devices for co-planar heterogeneous integration with Si", *Applied Physics Letters*, 106, 23, 233101, 2015.
- [254] Y. Han, Y. Xue, and K. M. Lau, "Selective lateral epitaxy of dislocation-free InP on silicon-on-insulator", *Applied Physics Letters*, 114, 19, 192105, 2019.
- [255] S. T. Šuran Brunelli, A. Goswami, B. Markman, H. Y. Tseng, M. Rodwell, C. Palmstrøm, and J. Klamkin, "Horizontal heterojunction integration via template-Assisted selective epitaxy", *Crystal Growth and Design*, 19, 12, 7030–7035, 2019.
- [256] S. Wirths, B. F. Mayer, H. Schmid, M. Sousa, J. Gooth, H. Riel, and K. E. Moselund, "Room-Temperature Lasing from Monolithically Integrated GaAs Microdisks on Silicon", *ACS Nano*, 12, 3, 2169–2175, 2018.

## References

---

- [257] K. E. Moselund, D. Cutaia, H. Schmid, H. Riel, S. Sant, and A. Schenk, "Complementary III–V heterostructure tunnel FETs", in *European Solid-State Device Research Conference (ESSDERC)*, IEEE, 2016, 403–407.
- [258] S. Mauthe, B. Mayer, M. Sousa, G. Villares, P. Staudinger, H. Schmid, and K. Moselund, "Monolithically integrated InGaAs microdisk lasers on silicon using template-assisted selective epitaxy", in *Nanophotonics VII*, D. L. Andrews, J.-M. Nunzi, A. Ostendorf, and A. J. Bain, Eds., SPIE, 2018, 103.
- [259] C. Convertino, C. Zota, H. Schmid, D. Caimi, M. Sousa, K. Moselund, and L. Czornomaz, "Replacement Metal Gate InGaAs-OI FinFETs by Selective Epitaxy in Oxide Cavities", in *2019 Joint International EUROSIOI Workshop and International Conference on Ultimate Integration on Silicon (EUROSIOI-ULIS)*, IEEE, 2019, 1–4.
- [260] D. Cutaia, K. E. Moselund, M. Borg, H. Schmid, L. Gignac, C. M. Breslin, S. Karg, E. Uccelli, and H. Riel, "Vertical InAs-Si Gate-All-Around Tunnel FETs Integrated on Si Using Selective Epitaxy in Nanotube Templates", *IEEE Journal of the Electron Devices Society*, 3, 3, 176–183, 2015.
- [261] M. Borg, H. Schmid, K. E. Moselund, D. Cutaia, and H. Riel, "Mechanisms of template-assisted selective epitaxy of InAs nanowires on Si", *Journal of Applied Physics*, 117, 14, 144303, 2015.
- [262] M. Borg, L. Gignac, J. Bruley, A. Malmgren, S. Sant, C. Convertino, M. D. Rossell, M. Sousa, C. Breslin, H. Riel, K. E. Moselund, and H. Schmid, "Facet-selective group-III incorporation in InGaAs template assisted selective epitaxy", *Nanotechnology*, 30, 8, 084004, 2019.
- [263] M. Knoedler, N. Bologna, H. Schmid, M. Borg, K. E. Moselund, S. Wirths, M. D. Rossell, and H. Riel, "Observation of Twin-free GaAs Nanowire Growth Using Template-Assisted Selective Epitaxy", *Crystal Growth & Design*, 17, 12, 6297–6302, 2017.
- [264] T. Akiyama, K. Sano, K. Nakamura, and T. Ito, "An Empirical Potential Approach to Wurtzite-Zinc-Blende Polytypism in Group III-V Semiconductor Nanowires", *Japanese Journal of Applied Physics*, 45, No. 9, L275–L278, 2006.
- [265] J. Johansson, J. Bolinsson, M. Ek, P. Caroff, and K. A. Dick, "Combinatorial approaches to understanding polytypism in III-V nanowires", *ACS Nano*, 6, 7, 6142–6149, 2012.
- [266] K. Ikejiri, Y. Kitauchi, K. Tomioka, J. Motohisa, and T. Fukui, "Zinc blende and wurtzite crystal phase mixing and transition in indium phosphide nanowires", *Nano Letters*, 11, 10, 4314–4318, 2011.
- [267] E. V. Anslyn and D. A. Dougherty, *Modern physical organic chemistry*. University science books, 2006.
- [268] Y. Kitauchi, Y. Kobayashi, K. Tomioka, S. Hara, K. Hiruma, T. Fukui, and J. Motohisa, "Structural Transition in Indium Phosphide Nanowires", *Nano Letters*, 10, 5, 1699–1703, 2010.

- 
- [269] B. S. A. Dayeh, D. Susac, K. L. Kavanagh, E. T. Yu, and D. Wang, “Structural and Room-Temperature Transport Properties of Zinc Blende and Wurtzite InAs Nanowires”, *Advanced Functional Materials*, 19, 2102–2108, 2009.
  - [270] G. Zhang, K. Tateno, H. Gotoh, T. Sogawa, and H. Nakano, “Structural, Compositional, and Optical Characterizations of Vertically Aligned AlAs/GaAs/GaP Heterostructure Nanowires Epitaxially Grown on Si Substrate”, *Japanese Journal of Applied Physics*, 49, 1–6, 2010.
  - [271] H. Gottschalk, G. Patzer, and H. Alexander, “Stacking fault energy and ionicity of cubic III–V compounds”, *physica status solidi (a)*, 45, 1, 207–217, 1978.
  - [272] T. Yamashita, T. Akiyama, K. Nakamura, and T. Ito, “Effects of facet orientation on relative stability between zinc blende and wurtzite structures in group III–V nanowires”, *Japanese Journal of Applied Physics*, 49, 5R, 55003, 2010.
  - [273] V. Pankoke, P. Kratzer, and S. Sakong, “Calculation of the diameter-dependent polytypism in GaAs nanowires from an atomic motif expansion of the formation energy”, *Physical Review B - Condensed Matter and Materials Physics*, 84, 7, 1–8, 2011.
  - [274] C. Thelander, P. Caroff, S. Plissard, A. W. Dey, and K. A. Dick, “Effects of crystal phase mixing on the electrical properties of InAs nanowires”, *Nano Letters*, 11, 6, 2424–2429, 2011.
  - [275] J. Wallentin, M. Ek, L. R. Wal-lenberg, L. Samuelson, K. Deppert, and M. T. Borgström, “Changes in contact angle of seed particle correlated with increased zincblende formation in doped InP nanowires”, *Nano letters*, 10, 12, 4807–4812, 2010.
  - [276] J. Wallentin, K. Mergenthaler, M. Ek, L. R. Wallenberg, L. Samuelson, K. Deppert, M.-E. Pistol, and M. T. Borgström, “Probing the wurtzite conduction band structure using state filling in highly doped InP nanowires”, *Nano letters*, 11, 6, 2286–2290, 2011.
  - [277] C. Thelander, K. A. Dick, M. T. Borgström, L. E. Fröberg, P. Caroff, H. A. Nilsson, and L. Samuelson, “The electrical and structural properties of n-type InAs nanowires grown from metal–organic precursors”, *Nanotechnology*, 21, 20, 205703, 2010.
  - [278] B. A. Wacaser, K. A. Dick, J. Johansson, M. T. Borgström, K. Deppert, and L. Samuelson, “Preferential interface nucleation: An expansion of the VLS growth mechanism for nanowires”, *Advanced Materials*, 21, 2, 153–165, 2009.
  - [279] F. Panciera, Z. Baraissov, G. Patriarche, V. G. Dubrovskii, F. Glas, L. Travers, U. Mirsaidov, and J.-C. Harmand, “Phase selection in self-catalysed GaAs nanowires”, *Nano Letters*, 2020.
  - [280] D. T. J. Hurle, “A mechanism for twin formation during Czochralski and encapsulated vertical Bridgman growth of III–V compound semiconductors”, *Journal of crystal growth*, 147, 3-4, 239–250, 1995.
  - [281] V. G. Dubrovskii and N. V. Sibirev, “Growth rate of a crystal facet of arbitrary size and growth kinetics of vertical nanowires”, *Physical Review E - Statistical Physics, Plasmas, Fluids, and Related Interdisciplinary Topics*, 70, 3, 7, 2004.

## References

---

- [282] J. Johansson, L. S. Karlsson, C. P. T. Svensson, T. Martensson, B. A. Wacaser, K. Deppert, L. Samuelson, and W. Seifert, “Structural properties of <111>B -oriented III-V nanowires”, *Nature Materials*, 5, 7, 574–580, 2006.
- [283] A. Taguchi, “First-principles investigations of surface reconstructions of an InAs (111)B surface”, *Journal of crystal growth*, 278, 1-4, 468–472, 2005.
- [284] T. Akiyama, T. Kondo, H. Tatematsu, K. Nakamura, and T. Ito, “Ab initio approach to reconstructions of the InP(111)A surface: Role of hydrogen atoms passivating surface dangling bonds”, *Physical Review B - Condensed Matter and Materials Physics*, 78, 20, 1–7, 2008.
- [285] H. Li, Y. Sun, C. Law, B. Visbeck, and F. Hicks, “Reconstructions of the InP(111)A surface”, *Physical Review B - Condensed Matter and Materials Physics*, 68, 8, 1–5, 2003.
- [286] H. J. Joyce, J. Wong-Leung, Q. Gao, H. H. Tan, and C. Jagadish, “Phase Perfection in Zinc Blende and Wurtzite III-V Nanowires Using Basic Growth Parameters”, *Nano Letters*, 10, 3, 908–915, 2010.
- [287] P. Krogstrup, S. Curiotto, E. Johnson, M. Aagesen, J. Nygård, and D. Chatain, “Impact of the liquid phase shape on the structure of III-V nanowires”, *Physical Review Letters*, 106, 12, 1–4, 2011.
- [288] V. G. Dubrovskii, “Development of growth theory for vapor–liquid–solid nanowires: contact angle, truncated facets, and crystal phase”, *Crystal Growth & Design*, 17, 5, 2544–2548, 2017.
- [289] A. M. Munshi, D. L. Dheeraj, J. Todorovic, A. T. Van Helvoort, H. Weman, and B. O. Fimland, “Crystal phase engineering in self-catalyzed GaAs and GaAs/GaAsSb nanowires grown on Si(111)”, *Journal of Crystal Growth*, 372, 163–169, 2013.
- [290] E. Gil, V. G. Dubrovskii, G. Avit, Y. André, C. Leroux, K. Lekhal, J. Grecenkov, A. Trasoudaine, D. Castelluci, G. Monier, R. M. Ramdani, C. Robert-Goumet, L. Bideux, J. C. Harmand, and F. Glas, “Record Pure Zincblende Phase in GaAs Nanowires down to 5 nm in Radius”, *Nano Letters*, 14, 7, 3938–3944, 2014.
- [291] I. Yang, X. Zhang, C. Zheng, Q. Gao, Z. Li, L. Li, M. N. Lockrey, H. Nguyen, P. Caroff, J. Etheridge, H. H. Tan, C. Jagadish, J. Wong-Leung, and L. Fu, “Radial Growth Evolution of InGaAs/InP Multi-Quantum-Well Nanowires Grown by Selective-Area Metal Organic Vapor-Phase Epitaxy”, *ACS Nano*, 12, 10, 10374–10382, 2018.
- [292] F. Schuster, J. Kapraun, G. N. Malheiros-Silveira, S. Deshpande, and C. J. Chang-Hasnain, “Site-Controlled Growth of Monolithic InGaAs/InP Quantum Well Nanopillar Lasers on Silicon”, *Nano Letters*, 17, 4, 2697–2702, 2017.
- [293] H.-J. Chu, T.-W. Yeh, L. Stewart, and P. D. Dapkus, “Wurtzite InP nanowire arrays grown by selective area MOCVD”, *physica status solidi (c)*, 7, 10, 2494–2497, 2010.
- [294] P. D. Nellist, “Scanning transmission electron microscopy”, *Springer Handbooks*, 49–99, 2019.

- 
- [295] P. W. Hawkes and J. C. H. Spence, *Springer Handbook of Microscopy*. Springer Nature, 2019.
- [296] J. Wen, J. Mabon, C. Lei, S. Burdin, E. Sammann, I. Petrov, A. B. Shah, V. Chobpattana, J. Zhang, K. Ran, J.-M. Zuo, S. Mishina, and T. Aoki, “The formation and utility of sub-angstrom to nanometer-sized electron probes in the aberration-corrected transmission electron microscope at the University of Illinois”, *Microscopy and Microanalysis*, 16, 2, 183–193, 2010.
- [297] C. M. Gruber, “Top-down Fabricated and Mechanically Actuated Field-enhancing Optical Antennas for Investigating Plasmon-Plasmon Interactions and Molecular Raman Scattering”, Ph.D. dissertation, ETH Zurich, 2018.
- [298] M. Yoshimi, M. Terauchi, A. Murakoshi, M. Takahashi, K. Matsuzawa, N. Shigyo, and Y. Ushiku, “Technology trends of silicon-on-insulator-its advantages and problems to be solved”, in *Proceedings of 1994 IEEE International Electron Devices Meeting*, IEEE, 1994, 429–432.
- [299] M. Bruel, “Silicon on insulator material technology”, *Electronics letters*, 31, 14, 1201–1202, 1995.
- [300] M. Borg, H. Schmid, J. Gooth, M. D. Rossell, D. Cutaia, M. Knoedler, N. Bologna, S. Wirths, K. E. Moselund, and H. Riel, “High-Mobility GaSb Nanostructures Cointegrated with InAs on Si”, *ACS Nano*, 11, 3, 2554–2560, 2017.
- [301] H. Schmid, B. Mayer, J. Gooth, S. Wirths, L. Czornomaz, H. Riel, S. Mauthe, C. Conventino, and K. E. Moselund, “Monolithic integration of multiple III-V semiconductors on Si”, *2017 IEEE SOI-3D-Subthreshold Microelectronics Technology Unified Conference (S3S)*, 1–3, 2017.
- [302] S. T. Šuran Brunelli, B. Markman, A. Goswami, H.-Y. Tseng, S. Choi, C. Palmstrøm, M. Rodwell, and J. Klamkin, “Selective and confined epitaxial growth development for novel nano-scale electronic and photonic device structures”, *Journal of Applied Physics*, 126, 1, 015703, 2019.
- [303] P. Staudinger, S. Mauthe, K. E. Moselund, and H. Schmid, “Concurrent Zinc-Blende and Wurtzite Film Formation by Selection of Confined Growth Planes”, *Nano Letters*, 18, 12, 7856–7862, 2018.
- [304] P. Staudinger, N. Tappy, S. Mauthe, K. Moselund, A. Fontcuberta i Morral, and H. Schmid, “Crystal Phase Tuning in Planar Films of III-V Semiconductors”, in *2019 Compound Semiconductor Week (CSW)*, vol. 18, IEEE, 2019, 1–2.
- [305] P. Staudinger, N. Tappy, S. Mauthe, K. E. Moselund, A. Fontcuberta i Morral, and H. Schmid, “Growth of Crystal Phase Engineered Planar Films of III-V Semiconductors”, in *European Workshop on Metal-Organic Vapour Phase Epitaxy (Poster)*, 2019.

## References

---

- [306] P. Parkinson, H. J. Joyce, Q. Gao, H. H. Tan, X. Zhang, J. Zou, C. Jagadish, L. M. Herz, and M. B. Johnston, "Carrier Lifetime and Mobility Enhancement in Nearly Defect-Free Core-Shell Nanowires Measured Using Time-Resolved Terahertz Spectroscopy", *Nano Letters*, 9, 9, 3349–3353, 2009.
- [307] R. Chau, S. Datta, and A. Majumdar, "Opportunities and challenges of III-V nano-electronics for future high-speed, low-power logic applications", in *IEEE Compound Semiconductor Integrated Circuit Symposium, 2005. CSIC '05.*, IEEE, 2005, 4 pp.
- [308] H. J. Joyce, Q. Gao, H. Hoe Tan, C. Jagadish, Y. Kim, J. Zou, L. M. Smith, H. E. Jackson, J. M. Yarrison-Rice, P. Parkinson, and M. B. Johnston, "III-V semiconductor nanowires for optoelectronic device applications", *Progress in Quantum Electronics*, 35, 2-3, 23–75, 2011.
- [309] R. L. Woo, R. Xiao, Y. Kobayashi, L. Gao, N. Goel, M. K. Hudait, T. E. Mallouk, and R. F. Hicks, "Effect of twinning on the photoluminescence and photoelectrochemical properties of indium phosphide nanowires grown on silicon (111)", *Nano Lett.*, 8, 4664–4669, 2008.
- [310] S. Perera, M. A. Fickenscher, H. E. Jackson, L. M. Smith, J. M. Yarrison-Rice, H. J. Joyce, Q. Gao, H. H. Tan, C. Jagadish, X. Zhang, and J. Zou, "Nearly intrinsic exciton lifetimes in single twin-free GaAsAlGaAs core-shell nanowire heterostructures", *Applied Physics Letters*, 93, 5, 1–4, 2008.
- [311] K. Li, K. W. Ng, T.-T. D. Tran, H. Sun, F. Lu, and C. J. Chang-Hasnain, "Wurtzite-Phased InP Micropillars Grown on Silicon with Low Surface Recombination Velocity", *Nano Letters*, 15, 11, 7189–7198, 2015.
- [312] D. Spirkoska, J. Arbiol, A. Gustafsson, S. Conesa-Boj, F. Glas, I. Zardo, M. Heigoldt, M. H. Gass, A. L. Bleloch, S. Estrade, M. Kaniber, J. Rossler, F. Peiro, J. R. Morante, G. Abstreiter, L. Samuelson, and A. Fontcuberta i Morral, "Structural and optical properties of high quality zinc-blende/wurtzite GaAs nanowire heterostructures", *Physical Review B*, 80, 24, 245325, 2009.
- [313] P. Tidemand-Petersson, O. Albrektsen, and J. Salzman, "Selective-area MOVPE for InP-based optoelectronic components", *Physica Scripta*, 1994, T54, 194, 1994.
- [314] C. Wilhelm, A. Larrue, X. Dai, D. Migas, and C. Soci, "Anisotropic photonic properties of III-V nanowires in the zinc-blende and wurtzite phase", *Nanoscale*, 4, 5, 1446–1454, 2012.
- [315] P. Staudinger, K. E. Moselund, and H. Schmid, "Exploring the Size Limitations of Wurtzite III-V Film Growth", *Nano Letters*, 20, 1, 686–693, 2020.
- [316] X. Cartoixa, M. Palummo, H. I. T. Hauge, E. P. A. M. Bakkers, and R. Rurali, "Optical Emission in Hexagonal SiGe Nanowires", *Nano Letters*, 17, 8, 4753–4758, 2017.
- [317] X. Zou, K. M. Wong, X. Zhu, W. C. Chong, J. Ma, and K. M. Lau, "High-Performance Green and Yellow LEDs Grown on SiO<sub>2</sub> Nanorod Patterned GaN/Si Templates", *IEEE Electron Device Letters*, 34, 7, 903–905, 2013.

- 
- [318] S. Wirths, R. Geiger, N. von den Driesch, G. Mussler, T. Stoica, S. Mantl, Z. Ikonik, M. Luysberg, S. Chiusi, J. M. Hartmann, H. Sigg, J. Faist, D. Buca, and D. Grützmacher, “Lasing in direct-bandgap GeSn alloy grown on Si”, *Nature Photonics*, 9, 2, 88–92, 2015.
  - [319] S. Lehmann, J. Wallentin, E. K. Mårtensson, M. Ek, K. Deppert, K. A. Dick, and M. T. Borgström, “Simultaneous Growth of Pure Wurtzite and Zinc Blende Nanowires”, *Nano Letters*, 19, 4, 2723–2730, 2019.
  - [320] F. Ren, K. Wei Ng, K. Li, H. Sun, and C. J. Chang-Hasnain, “High-quality InP nanoneedles grown on silicon”, *Applied Physics Letters*, 102, 1, 98–102, 2013.
  - [321] L. C. Chuang, M. Moewe, K. W. Ng, T.-T. D. Tran, S. Crankshaw, R. Chen, W. S. Ko, and C. J. Chang-Hasnain, “GaAs nanoneedles grown on sapphire”, *Applied Physics Letters*, 98, 12, 123101, 2011.
  - [322] T. Wu, C.-W. Sher, Y. Lin, C.-F. Lee, S. Liang, Y. Lu, S.-W. Huang Chen, W. Guo, H.-C. Kuo, and Z. Chen, “Mini-LED and Micro-LED: Promising Candidates for the Next Generation Display Technology”, *Applied Sciences*, 8, 9, 1557, 2018.
  - [323] M. Hjort, S. Lehmann, J. Knutsson, R. Timm, D. Jacobsson, E. Lundgren, K. Dick, and A. Mikkelsen, “Direct Imaging of Atomic Scale Structure and Electronic Properties of GaAs Wurtzite and Zinc Blende Nanowire Surfaces”, *Nano Letters*, 13, 9, 4492–4498, 2013.
  - [324] M. Cantoro, G. Brammertz, O. Richard, H. Bender, F. Clemente, M. Leys, S. Degroote, M. Caymax, M. Heyns, and S. De Gendt, “Controlled III/V Nanowire Growth by Selective-Area Vapor-Phase Epitaxy”, *Journal of The Electrochemical Society*, 156, 11, H860, 2009.
  - [325] A. M. Sanchez, Y. Zhang, E. W. Tait, N. D. M. Hine, H. Liu, and R. Beanland, “Non-radiative Step Facets in Semiconductor Nanowires”, *Nano Letters*, 17, 4, 2454–2459, 2017.
  - [326] E. K. Mårtensson, S. Lehmann, K. A. Dick, and J. Johansson, “Simulation of GaAs Nanowire Growth and Crystal Structure”, *Nano Letters*, 19, 2, 1197–1203, 2019.
  - [327] D. A. B. Miller, “Attojoule Optoelectronics for Low-Energy Information Processing and Communications”, *J. Lightwave Technol.*, 35, 3, 346–396, 2017.
  - [328] M. Gaio, D. Saxena, J. Bertolotti, D. Pisignano, A. Camposeo, and R. Sapienza, “A nanophotonic laser on a graph”, *Nature Communications*, 10, 1, 226, 2019.
  - [329] H. Zhao, P. Miao, M. H. Teimourpour, S. Malzard, R. El-Ganainy, H. Schomerus, and L. Feng, “Topological hybrid silicon microlasers”, *Nature Communications*, 9, 1, 981, 2018.
  - [330] S. Liu, G. A. Keeler, J. L. Reno, M. B. Sinclair, and I. Brener, “III-V Semiconductor Nanoresonators - A New Strategy for Passive, Active, and Nonlinear All-Dielectric Metamaterials”, *Advanced Optical Materials*, 4, 10, 1457–1462, 2016.

## References

---

- [331] M. Akabori, J. Takeda, J. Motohisa, and T. Fukui, “InGaAs nano-pillar array formation on partially masked InP(111)B by selective area metal–organic vapour phase epitaxial growth for two-dimensional photonic crystal application”, *Nanotechnology*, 14, 10, 1071–1074, 2003.
- [332] G. Crosnier, D. Sanchez, S. Bouchoule, P. Monnier, G. Beaudoin, I. Sagnes, R. Raj, and F. Raineri, “Hybrid indium phosphide-on-silicon nanolaser diode”, *Nature Photonics*, 11, 5, 297–300, 2017.
- [333] G. Morthier, T. Spuesens, P. Mechet, G. Roelkens, and D. Van Thourhout, “InP Microdisk Lasers Integrated on Si for Optical Interconnects”, *IEEE Journal of Selected Topics in Quantum Electronics*, 21, 6, 359–368, 2015.
- [334] A. De Groote, P. Cardile, A. Z. Subramanian, A. M. Fecioru, C. Bower, D. Delbeke, R. Baets, and G. Roelkens, “Transfer-printing-based integration of single-mode waveguide-coupled III-V-on-silicon broadband light emitters”, *Optics Express*, 24, 13, 13754, 2016.
- [335] G. Roelkens, J. Van Campenhout, J. Brouckaert, D. Van Thourhout, R. Baets, P. R. Romeo, P. Regreny, A. Kazmierczak, C. Seassal, X. Letartre, G. Hollinger, J. Fedeli, L. Di Cioccio, and C. Lagahe-Blanchard, “III-V/Si photonics by die-to-wafer bonding”, *Materials Today*, 10, 7-8, 36–43, 2007.
- [336] B. Mayer, L. Janker, B. Loitsch, J. Treu, T. Kostenbader, S. Lichtmannecker, T. Reichert, S. Morkötter, M. Kaniber, G. Abstreiter, C. Gies, G. Koblmüller, and J. J. Finley, “Monolithically Integrated High- $\beta$  Nanowire Lasers on Silicon”, *Nano Letters*, 16, 1, 152–156, 2016.
- [337] Z. Wang, B. Tian, M. Pantouvaki, W. Guo, P. Absil, J. Van Campenhout, C. Merckling, and D. Van Thourhout, “Room-temperature InP distributed feedback laser array directly grown on silicon”, *Nature Photonics*, 9, 12, 837–842, 2015.
- [338] B. Kunert, W. Guo, Y. Mols, B. Tian, Z. Wang, Y. Shi, D. Van Thourhout, M. Pantouvaki, J. Van Campenhout, R. Langer, and K. Barla, “III/V nano ridge structures for optical applications on patterned 300 mm silicon substrate”, *Applied Physics Letters*, 109, 9, 091101, 2016.
- [339] S. Lourdudoss, “Heteroepitaxy and selective area heteroepitaxy for silicon photonics”, *Current Opinion in Solid State and Materials Science*, 16, 2, 91–99, 2012.
- [340] S. Mauthe, N. Vico Trivino, Y. Baumgartner, M. Sousa, D. Caimi, T. Stoferle, H. Schmid, and K. E. Moselund, “InP-on-Si Optically Pumped Microdisk Lasers via Monolithic Growth and Wafer Bonding”, *IEEE Journal of Selected Topics in Quantum Electronics*, 25, 6, 1–7, 2019.
- [341] B. F. Mayer, S. Wirths, S. Mauthe, P. Staudinger, M. Sousa, J. Winiger, H. Schmid, and K. E. Moselund, “Microcavity Lasers on Silicon by Template-Assisted Selective Epitaxy of Microsubstrates”, *IEEE Photonics Technology Letters*, PP, c, 1–1, 2019.

- [342] Y. Li, Z. Liu, X. Lu, Z. Su, Y. Wang, R. Liu, D. Wang, J. Jian, J. H. Lee, H. Wang, Q. Yu, and J. Bao, “Broadband infrared photoluminescence in silicon nanowires with high density stacking faults”, *Nanoscale*, 7, 5, 1601–1605, 2015.
- [343] B. Bennett, R. Soref, and J. Del Alamo, “Carrier-induced change in refractive index of InP, GaAs and InGaAsP”, *IEEE Journal of Quantum Electronics*, 26, 1, 113–122, 1990.



# Curriculum Vitae

## Personal Data

Name Philipp Staudinger  
Date of Birth 24.08.1990  
Place of Birth Vöcklabruck, Austria  
Citizen of Austria

## Education

2017 – 2020 **École polytechnique fédérale de Lausanne**, Switzerland  
PhD candidate, Materials Science and Engineering  
2014 – 2016 **Technische Universität Wien**, Austria  
Master of Science, Microelectronics and Photonics, **1.0** "with distinction"  
2015 **University of Waterloo**, Canada  
Exchange Semester, **4.0/4.0**  
2011 – 2014 **Johannes Kepler Universität Linz**, Austria  
Bachelor of Science, Information Electronics, "with distinction"

## Professional Experience

2017 – 2020 **IBM Research – Zurich**, Switzerland  
Predoctoral Scientist, Science & Technology Department  
2016 – 2017 **Technische Universität Wien**, Austria  
Research Assistant, Institute of Solid State Electronics

### Activities and Certificates

- 2018 – 2020 **Peer-Review**, upon invitation for various scientific journals
- 05/2019 **Session Chair**, Compound Semiconductor Week, Nara, Japan  
Growth of Nanostructures and Quantum-Effect Devices
- 10/2017 **Transmission Electron Microscopy 1**, ETH Zürich, Switzerland  
ScopeM Certificate
- 03/2016 **ATHENS Exchange Program**, Telecom ParisTech, France  
Scientific Research Method: Techniques, Models and Practices
- 11/2015 **Student Leadership Certificate**, University of Waterloo, Canada
- 2012 – 2014 **Teaching Assistant**, Johannes Kepler Universität Linz, Austria  
Electrical Engineering 1, Signals and Systems 1 and Software Engineering 1

### Awards and Recognitions

- 02/2020 **Invited Feature**, Compound Semiconductor Magazine, United Kingdom  
“Crystal Phase Tuning Creates New Functionality”
- 06/2019 **Young Scientist Award**, European Workshop on MOVPE, Vilnius, Lithuania
- 05/2019 **Best Student Paper Award**, Compound Semiconductor Week, Nara, Japan
- 09/2018 **First Patent Achievement Award**, IBM Research, Zurich, Switzerland
- 09/2017 **Preis der Fakultät**, ETIT, TU Wien, Austria
- 2012 – 2015 **Merit-Based Scholarships**, JKU Linz (2x) and TU Wien, Austria

### Selected Conference Presentations

(Journal Publications are listed in **List of Publications**)

- 11/2020 **Microprocesses and Nanotechnology Conference**, Osaka, Japan  
**Invented talk**, to be presented
- 06/2019 **European Workshop on MOVPE**, Vilnius, Lithuania  
Growth of Crystal Phase Engineered Planar Films of III-V Semiconductors, **poster**
- 05/2019 **Compound Semiconductor Week**, Nara, Japan  
Crystal Phase Tuning in Planar Films of III-V Semiconductors, **talk**
- 06/2018 **Swiss NanoConvention**, Zürich, Switzerland  
Zinc-Blende and Wurtzite Phase Formation in InP Nano-structures Grown by Template-Assisted Selective Epitaxy, **poster**
- 03/2018 **DPG Spring Meeting**, Berlin, Germany  
Zinc-Blende and Wurtzite Phase Formation in InP Nanowires Grown by Template-Assisted Selective Epitaxy, **talk**